Entanglement and Decoherence in a Trapped-Ion Quantum Register

by

David Kielpinski

B.A., University of Chicago, 1996

A thesis submitted to the

Faculty of the Graduate School of the

University of Colorado in partial fulfillment

of the requirements for the degree of

Doctor of Philosophy

Department of Physics

2001

This thesis entitled:
Entanglement and Decoherence in a Trapped-Ion Quantum Register
written by David Kielpinski
has been approved for the Department of Physics

Dr. David Wineland

Prof. Eric Cornell

Date

The final copy of this thesis has been examined by the signatories, and we find that both the content and the form meet acceptable presentation standards of scholarly work in the above mentioned discipline.

Kielpinski, David (Ph.D., Physics)

Entanglement and Decoherence in a Trapped-Ion Quantum Register

Thesis directed by Dr. David Wineland

This thesis describes the construction of a small quantum register using laser-cooled $^9Be^+$ ions in a linear RF trap. Each qubit corresponds to a single trapped ion, with the two qubit levels being two hyperfine sublevels of the ground electronic state. I outline the basics of ion trapping and cooling and describe the operation of single-qubit logic gates using Raman transitions. I then review work performed during my tenure. We have realized an entangling gate and have produced entangled states of up to four ions. This gate enables universal quantum logic on two qubits in our system. We investigated several applications of this two-qubit register. We demonstrated a violation of a Bell inequality that closes the detector loophole. This experiment was the first to perform a complete set of Bell correlation measurements on massive particles. We also demonstrated rotation angle estimation with precision better than the standard quantum limit (SQL) using a two-ion entangled state. As a special case, we performed Ramsey spectroscopy at precision better than the SQL, opening a possibility for improvement of atomic clocks. We observed a number of decoherence mechanisms in our register, the most prominent being magnetic field fluctuations and heating of the ion motion. We propose a way to eliminate the effects of heating. Finally, we implemented a decoherence-free quantum memory that was shielded from the effects of magnetic field fluctuations. Encoding one qubit's worth of information in the decoherence-free subspace of two ions increased the memory lifetime by a factor of three under ambient conditions.

Dedication

To my mother, Andrea Kielpinski Sadler, Ph.D.,

my aunt, Eva Parrucci,

my late grandmother, Florence Kielpinski

and especially, my late grandfather

Francis S. Kielpinski

whose affection and encouragement inspired this work

Acknowledgements

The credit for this thesis redounds ultimately to the many people who patiently taught me to do experiments, even when I apparently had bananas in my ears. Special thanks go to Dave Wineland and Chris Monroe, my two amiable, approachable, and knowledgeable advisors. Thanks also to Brian King, for answering even the goofiest of first-year grad student questions, Volker Meyer, for initiating me into the mysteries of German humor, Wayne Itano, for his amazing ability to communicate with both computers and me, and Cass Sackett, the nicest supergenius I know. The contributions of my labmates are too numerous to describe here: it is a pleasure to acknowledge Amit Ben-Kish, Jim Bergquist, Didi Leibfried, Chris Myatt, Mary Rowe, Quentin Turchette, and Chris Wood. And I fully expect this thesis to pale in comparison to that of Joe Britton.

Contents

Tables

Table

Figures

Figure

Chapter 1

Introduction

This thesis describes the construction of a small quantum register using laser-cooled $^9Be^+$ ions in a linear RF trap. The register is composed of elementary two-level systems, "qubits," which are analogous to single bits in a classical computer. Each qubit corresponds to a single trapped ion, with the two qubit levels being two hyperfine sublevels of the ground electronic state. The quantum state of the whole register encodes information, and an appropriate unitary evolution of the state of the register can perform a computing task.

Here we demonstrate the ability to transform an arbitrary quantum state of two qubits into any other quantum state. In the language of computing, we can perform universal quantum logic on two qubits. A universality construction similar to that of classical computer science guarantees that the operations demonstrated here suffice for universal quantum logic on a large quantum register as well. In some sense, then, only technical difficulties stand between us and a full-scale quantum computer. For some tasks, quantum algorithms are much more efficient than any known classical algorithm, in particular for factoring of large numbers [1]. To factor an N-digit number, a classical computer requires resources that are exponential in N, but a quantum computer only requires resources polynomial in N. Because most modern cryptography relies on the difficulty of factoring large numbers, a full-scale quantum computer could have a large impact on many areas of technology, Internet commerce being only one example.

We used the quantum register to study two central phenomena in quantum information: entanglement and decoherence. Writing the two states of a qubit as $|\downarrow\rangle$ and $|\uparrow\rangle$, we see that the two-qubit state $|\downarrow\uparrow\rangle - |\uparrow\downarrow\rangle$ is entangled: we cannot decompose this state into a product $|\Psi_1\rangle|\Psi_2\rangle$ of two single-qubit states. While quantum logic operations on single qubits have been commonplace for a long time under a variety of names, controlled manipulation of entanglement has only become possible in the last few years. Entanglement is thought to be closely related to the efficiency of quantum computers. A unique feature of our experiment is that we can generate and manipulate entangled states of two qubits on demand, so that we have complete control over the behavior of the register. No other quantum computing experiment has demonstrated this ability to date.

If entanglement provides the power of quantum computing, decoherence takes it away again. Interactions of our quantum register with the environment disturb the register state, causing transfer of the information in the register to the environment. From the quantum information point of view, decoherence is just this loss of information from the register. A wide variety of physical processes cause decoherence, and methods of eliminating decoherence will be essential for large-scale quantum computers.

The outline of the thesis is as follows. Chapters 2, 3, and 4 describe the basics of the experimental apparatus and the underlying theory. Chapter 2 explains the physical principles behind ion trapping, from both a classical and a quantum perspective, and the dynamics of laser-cooled ion crystals in traps. I then describe the construction of our ion traps and the apparatus needed to operate them. In Chapter 3, I develop the theory of coherent manipulation

of a single $^9Be^+$ ion by stimulated Raman transitions and explain how to cool ion crystals to the ground state of their quantized motion. Chapter 4 describes the laser apparatus used for initialization, manipulation, and detection of the register state.

The rest of the thesis reviews work done during my tenure as a graduate student. In Chapter 5, I describe the method we used to create entangled states of the register and present data on entangled states of two and four qubits. The two-qubit entangling operation, in conjunction with the single-qubit operations discussed in Chapter 3, suffices for universal quantum logic. Chapter 6 presents two applications of the two-qubit register. We demonstrated a violation of a Bell inequality with no detector loophole. This experiment was the first to perform a complete set of Bell correlation measurements on massive particles. We also demonstrated rotation angle estimation with precision better than the standard quantum limit (SQL) using a two-ion entangled state. As a special case, we performed Ramsey spectroscopy at precision better than the SQL, opening a possibility for improvement of atomic clocks. Chapter 7 describes the major decoherence mechanisms affecting the quantum register.[1] I present a detailed analysis of gate errors for the entangling gate. The errors mostly arise from heating of the ion motion, and I discuss the data on heating gathered so far. We have no definite conclusion on the source of heating, but I describe a way to eliminate its effects through sympathetic cooling of the ion crystal. In Chapter 8, I present an experiment on eliminating a particular class of decoherence processes through encoding of quantum information into a decoherence-free subspace. Rather than attacking the physical mechanisms creating decoherence, we encoded the information so as to decouple the register state from the environment. The encoded information was completely unaffected by the class of decoherence processes we targeted, and survived much longer than the unencoded information under ambient conditions. The useful properties of the encoding suggest that some similar encoding will be commonly used in large-scale quantum computing.

[1] While some of the work in Chapter 7 predates me, our understanding of decoherence has advanced quite a bit over the course of my studies. As a general rule, any information not found in Ref. [2] is new work.

Since this work was carried out at the National Institute of Standards and Technology, SI units are obsessively used throughout.

Chapter 2

Trap Apparatus

The experiments described in this thesis used radio-frequency (RF) traps to confine $^9Be^+$ ions under ultra-high vacuum (UHV). In these traps, one applies large RF voltages to an electrode structure made of conducting material in order to create a quadrupole electric field with a minimum in free space. For appropriate RF voltages and frequencies, the RF field induces a ponderomotive potential that confines $^9Be^+$ ions harmonically at the field minimum. The ions are then well isolated from environmental perturbations, enabling the precise quantum state control needed for these experiments.

2.1 Linear RF Trap

Linear RF traps were used for almost all the experiments described here. One common electrode structure for such a trap [3] is shown in Fig. 2.1. Essentially the trap is a quadrupole mass filter plugged at the ends with static potentials. To operate the trap, one applies RF voltage to the rods 1 and 3 of Fig. 2.1, while rods 2 and 4 are held at RF ground. The induced ponderomotive potential confines the ions to the RF nodal line, which lies along the $\hat{z}$ axis. The "endcap" segments of rods 2 and 4 are held at a positive DC voltage relative to the middle segments of those rods, pushing the (positive) ions toward the center of the trap. The $\hat{x}$ axis lies on the line connecting rods 1 and 3, while the $\hat{y}$ axis lies on the line connecting rods 2 and

4.

It is difficult to calculate the exact electric potential created by this electrode configuration. However, as we will see, the ions are held at minima of the electric field, so the lowest-order term in the electric field is the quadrupole term. In our experiments, the amplitude of the ions' motion is so small compared to the distance between trap electrodes that the higher-order terms in the multipole expansion are negligible [4]. Thus we can write the electric potential in the region of interest as a sum of RF and DC quadrupole potentials:

$$\phi(\vec{x},t) = \frac{1}{2}\frac{x^2-y^2}{R^2}\kappa_{\mathrm{RF}}V_0\cos\Omega_T t + \kappa_{\mathrm{DC}}U_0\frac{1}{R^2}\left[z^2 - \frac{1}{2}(\epsilon_{\mathrm{DC}}x^2 + (1-\epsilon_{\mathrm{DC}})y^2)\right] \tag{2.1}$$

where V_0, U_0 are the applied RF and DC voltages, R is the distance from the RF nodal line to the electrode surfaces, and $\kappa_{\mathrm{RF,DC}}$ and ϵ_{DC} are geometric factors. The frequency of the RF field, Ω_T, is often called the drive frequency, and is expressed here in rad/s.

2.1.1 Single-Ion Dynamics (Classical)

For the present, we model an ion as a classical charged point particle. The equations of motion for the ion are separable in the $\{\hat{x},\hat{y},\hat{z}\}$ basis. Since there is no RF field along $\hat{z}$, the axial potential is purely harmonic with frequency $\omega_z = \sqrt{e\kappa_{\mathrm{DC}}U_0/m}$. The Mathieu equation

$$\frac{d^2x}{d\zeta^2} + [a + 2q\cos 2\zeta]x = 0 \tag{2.2}$$

describes the motion along $\hat{x}$, where we use dimensionless variables

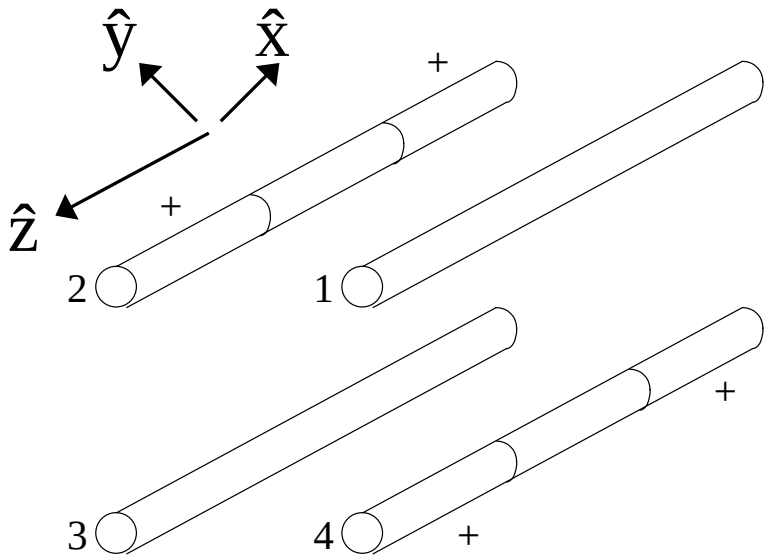

Figure 2.1: Electrode structure of a linear RF trap. A common RF voltage is applied to rods 1 and 3, while rods 2 and 4 are held at RF ground. Rods 1 and 3 are held at DC ground, while the "endcap" segments of rods 2 and 4, labeled with a "+", are held at positive DC potential with respect to the middle segments of those rods.

$$\zeta = \Omega_T t/2 \qquad \text{time} \tag{2.3}$$

$$q = \frac{2e\kappa_{\rm RF}V_0}{m\Omega_T^2 R^2} \qquad \text{RF voltage} \tag{2.4}$$

$$a = \frac{-4e\epsilon_{\rm DC}\kappa_{\rm DC}U_0}{m\Omega_T^2 R^2} \qquad \text{DC voltage} \tag{2.5}$$

Eq. 2.2 also describes the motion along $\hat{y}$ for x replaced by y, q replaced by $-q$, and $\epsilon_{\rm DC}$ replaced by $1-\epsilon_{\rm DC}$.

Since the Mathieu equation (2.2) is periodic in time, we can apply Floquet's theorem [5] to find solutions of the form

$$x(\zeta) \propto e^{\pm i\beta\zeta} f(\zeta) \tag{2.6}$$

with $f(\zeta+\pi) = f(\zeta)$. Stable solutions require $\beta = \beta(a,q)$ real. Fig. 2.2 shows the regions of stability in the $a-q$ plane [6]. In particular, the ion motion is stable for $|a| < q^2 \ll 1$, and expanding in these parameters to lowest order, we find

$$x(\zeta) \approx x_0 e^{i\beta(\zeta+\zeta_0)}\left[1+\frac{1}{2}q\sin 2\zeta\right] \tag{2.7}$$

$$\beta = \left(a+\frac{1}{2}q^2\right)^{1/2} \tag{2.8}$$

with ζ_0 a constant phase. Rewriting Eq. 2.8 in SI units gives

$$x(t) \approx x_0 e^{i(\omega t+\phi)}\left[1+\frac{e\kappa_{\rm RF}V_0}{m\Omega_T R^2}\sin\Omega_T t\right] \tag{2.9}$$

$$\omega = \frac{1}{2}\beta\Omega_T \tag{2.10}$$

with ϕ a constant phase. Eq. (2.9) describes harmonic motion of the ion at the "secular" frequency ω, modulated by the much smaller "micromotion" term at the drive frequency Ω_T.

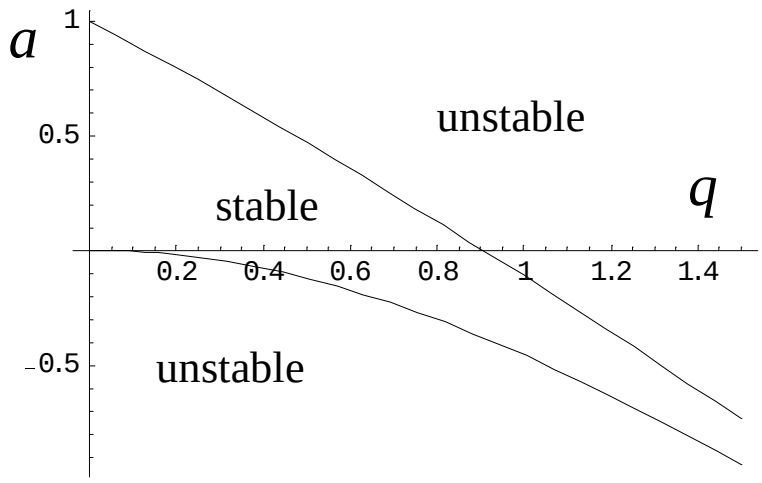

Figure 2.2: Stability diagram for RF confinement of a charged particle in a linear trap. The shaded region indicates the values of a and q for which the trapping is stable along $\hat{x}$.

Again ω and Ω_T are expressed in rad/s. If we neglect the micromotion and the effects of the DC field, the ion moves in an effective harmonic potential with secular frequency

$$\omega_{\mathrm{RF}} = \frac{e\kappa_{\mathrm{RF}}V_0}{\sqrt{2}m\Omega_T R^2} \tag{2.11}$$

Although ω_{RF} formally diverges for small Ω_T, so do a and q, so that the approximations leading to Eq. (2.11) become invalid. If we take Ω_T, V_0, and U_0 to zero in such a way that a and q remain constant, we find $V_0 \propto \Omega_T^2$, so that ω_{RF} actually goes to zero for both large and small Ω_T. To get high secular frequencies, the strategy is to apply as large an RF voltage as possible, then choose the smallest Ω_T such that the ions remain stably trapped. Though Fig. 2.2 suggests that the ion motion remains stable for $q \approx 0.8$, our experience was that reliable long-term confinement of a few ions requires $q \lesssim 0.3$.

Real ion traps are frequently subject to ambient electric fields. These fields arise, for instance, from charging of insulating material used in trap construction. Usually the amplitude of ion motion is small enough that we can neglect the spatial variation of the ambient field. Then

the ion feels a constant force F_x, which we take along $\hat{x}$, and including this force in Eq. (2.2), we find the new trajectory

$$x(\zeta) \approx (x_0 e^{i\beta(\zeta+\zeta_0)} + x_1)\left[1 + \frac{1}{2}q\sin 2\zeta\right] \tag{2.12}$$

where $x_1 = 4F_x/(m\omega^2)$. The field displaces the ion from the center of the quadrupole potential and increases the amplitude of micromotion. For Doppler-cooled ions, the amplitude of secular motion x_0 is typically less than 100 nm, so even very small ambient fields (on the order of 100 V/m) can significantly increase the micromotion amplitude.

2.1.2 Single-Ion Dynamics (Quantum)

Quantizing the ion motion along the trap axis $\hat{z}$ is straightforward. For Doppler-cooled ions, the anharmonicity of the DC potential is very small and the usual harmonic oscillator quantization holds. The energy eigenstates are equally spaced with level spacing equal to the axial trap frequency ω_z, and the ground state of the axial motion has wavepacket spread $\sqrt{\hbar/(m\omega_z)}$.

The classical dynamics along the transverse directions $\hat{x}, \hat{y}$ is rigorously described by the Mathieu equation (2.2) and so appears difficult to quantize. However, in the usual regime of small a and q, we can neglect the micromotion to a first approximation and simply treat the potential as harmonic with frequency ω. Quantizing then yields the standard harmonic oscillator spectrum for the motional energy eigenstates along $\hat{x}$ and $\hat{y}$. In a semiclassical extension of this model to include the effects of micromotion, one modulates the position operator by adding a c-number term $x_\mu \cos 2\zeta$, where x_μ is the classical micromotion amplitude.

While this semiclassical model accounts for the data presented in this thesis, it leaves important open questions about the full quantum dynamics. For instance, it is not *a priori* obvious whether there is a true ground state of the ion motion. Therefore we will briefly outline the quantum dynamics in the regime of small a and q.

In the Heisenberg picture, the position operator $\mathbf{x}$ evolves according to Eq. (2.2) [7] and we make the ansatz [8]

$$\mathbf{x}(\zeta) = \sqrt{\frac{1}{2\beta}}[s(\zeta)\mathbf{a}^\dagger + \text{h.c.}] \tag{2.13}$$

$$s(\zeta) = e^{i\beta\zeta}\left[1 + \frac{1}{2}q\sin 2\zeta\right] \tag{2.14}$$

where $\mathbf{a}$ is a time-independent operator satisfying the harmonic oscillator commutation relations $[\mathbf{a}, \mathbf{a}^\dagger] = 1$. Since $s(\zeta)$ solves the classical Mathieu equation to lowest order in a and q, ansatz (2.13) solves the quantum Mathieu equation in the same approximation.

We can rewrite the equation of motion (2.13) using the time evolution operator $\mathbf{U}$ as follows:

$$\mathbf{x}(\zeta) = \mathbf{U}^\dagger\mathbf{x}(0)\mathbf{U} \tag{2.15}$$

$$\mathbf{U} = \exp\left(\frac{1}{2}r(\zeta)\left(\mathbf{a}^2 - \mathbf{a}^{\dagger 2}\right)\right)\exp(-i\beta\mathbf{a}^\dagger\mathbf{a}\zeta) \tag{2.16}$$

where $r(\zeta) = -(q/2)\sin 2\zeta$ and we have set $\hbar = 1$. Using $i(d\mathbf{U}/d\zeta) = \mathbf{H}\mathbf{U}$, we find the effective Hamiltonian

$$\mathbf{H}(\zeta) = \beta\mathbf{a}^\dagger\mathbf{a} - \frac{1}{2}iq(\mathbf{a}^2 - \mathbf{a}^{\dagger 2})\cos 2\zeta \tag{2.17}$$

to lowest order in a, q. The first term in this Hamiltonian drives the secular oscillation at frequency β, while the second term describes squeezing of the ion wavepacket [9].

The evolution operator (2.16) has the form $\mathbf{U}(\zeta_k) = \exp(-i\beta\mathbf{a}^\dagger\mathbf{a})$ for times $\zeta_k = k\pi/2$, k an integer. If we take snapshots of the dynamics at the times ζ_k, the evolution appears to be that of a simple harmonic oscillator. At times $\zeta \neq \zeta_k$, the motional state will be squeezed by the factor $r(\zeta)$. The bandwidth of measurements on the ion motional state is usually much less than Ω_T. In this case, the fractional change in expectation value of an observable $\mathbf{O}$ due to the squeezing is

$$\delta_{\rm sqz}(\mathbf{O}) = 1 - \frac{\int_0^\pi \langle \mathbf{O}(\zeta)\rangle \, d\zeta}{\langle \mathbf{O}(0)\rangle} \tag{2.18}$$

and we find $\delta_{\rm sqz}(\mathbf{x}) = 0$, $\delta_{\rm sqz}(\mathbf{x}^2) = \mathcal{O}(q^2)$. Thus, to first order in q, we can consider the quantized ion motion to be that of a simple harmonic oscillator of frequency β.

Our quantum treatment has so far assumed that the ion sits at the RF node, so that the quantum version of Eq. (2.2) describes the evolution of the position operator $\mathbf{x}$. We can readily include the effect of a uniform force F_x, such as that arising from an ambient electric field, in our quantum description. In this case $\mathbf{x}(\zeta)$ evolves according to

$$\frac{d^2\mathbf{x}}{d\zeta^2} + [a + 2q\cos 2\zeta]\mathbf{x} = f_x \tag{2.19}$$

where f_x is the normalized force $4F_x/(m\Omega_T^2)$, and we make the ansatz

$$\mathbf{x}(\zeta) = \sqrt{\frac{1}{2\beta}}[s(\zeta)\mathbf{a}^\dagger + \text{h.c.}] + \frac{f_x}{\beta^2}\left[1 + \frac{1}{2}q\sin 2\zeta\right] \tag{2.20}$$

where the first term solves the homogeneous quantum Mathieu equation and the second term

is a c-number solution to the inhomogeneous classical Mathieu equation. Thus we can interpret the ion motion as composed of a quantum state evolving according to Eq. (2.16), but with its x-coordinate displaced by the classical micromotion of amplitude $x_1 = 4F_x/(m\omega^2)$. The semi-classical treatment of micromotion given above therefore neglects only the micromotion-induced squeezing of the ion wavepacket, which typically affects measurements only in order $\mathcal{O}(q^2)$.

2.1.3 Multiple-Ion Dynamics

When multiple ions are present in the trap, we must consider the Coulomb repulsion between ions as well as the ions' interaction with the harmonic trapping potential. If the ions are sufficiently cold, the equilibrium positions of the ions are given by minimizing the potential energy. The possible equilibrium configurations have been extensively studied experimentally [10, 11, 12] and theoretically [13, 14]. For sufficiently weak axial confinement, the equilibrium positions all lie on the trap axis $x = y = 0$, so that the ions line up in a string, as shown in Fig. 2.3. In this configuration, the ions all have the same (small) amplitude of micromotion. As we will see in Section 5, this fact is essential to operation of our entangling gate. The string configuration was used for all the experiments described in this thesis. The positions of the ions along z are given for the string by minimizing the potential [15, 16, 17]

$$V(z_1, \ldots z_N) = \frac{1}{2} m\omega_z^2 \sum_{i=1}^{N} z_i^2 + \frac{e^2}{8\pi\epsilon_0} \sum_{\substack{i,j=1 \\ i\neq j}}^{N} \frac{1}{|z_i - z_j|} \tag{2.21}$$

where $z_1, \ldots, z_N$ are the equilibrium positions for a string of N ions and ω_z the axial trapping frequency. Defining normalized positions as $u_i \equiv z_i/\ell$ with $\ell^3 \equiv e^2/(4\pi\epsilon_0 m\omega_z^2)$, we find a coupled set of equations for the u_i

$$u_i - \sum_{j=1}^{i-1} \frac{1}{(u_i - u_j)^2} + \sum_{j=i+1}^{N} \frac{1}{(u_i - u_j)^2} = 0, \;\; i = 1 \ldots N \tag{2.22}$$

Table 2.1: Scaled positions u_i for two, three, and four ions.

N	u_i
2	$-(1/2)^{2/3}$ $(1/2)^{2/3}$
3	$-(5/4)^{1/3}$ 0 $(5/4)^{1/3}$
4	-1.437 -0.454 0.454 -1.437

These equations have analytic solutions only for $N \leq 3$. Numerical solutions for $N \leq 10$ have been calculated by Steane [15] and James [16]. For two, three, and four ions, the cases of interest here, the scaled positions are given in Table 2.1. Here the scaling factor $\ell = 7.25\ \nu_z^{-2/3} \mu$m for $^9Be^+$, with ν_z the axial trap frequency in MHz (not in rad/s).

The full dynamics for multiple ions are quite complicated, and in general are chaotic [18, 19, 20] due to the nonlinearity of the Coulomb force. However, Doppler-cooled ions have a motional amplitude of less than 100 nm and typical ion spacings are several μm, so we can linearize the Coulomb force. The ions then undergo coupled harmonic oscillations about their equilibrium positions. The potential is separable in $\{\hat{x}, \hat{y}, \hat{z}\}$ once we linearize the Coulomb force. We first consider oscillations along $\hat{z}$. Writing the displacement of the ith ion as $q_i(t) = z_i(t) - \ell u_i$ yields the quadratic Lagrangian [16, 17]

$$L = \frac{m}{2} \sum_{i=1}^{N} \dot{q}_i^2 - \frac{1}{2} \sum_{i,j=1}^{N} \left. \frac{\partial^2 V}{\partial z_i \partial z_j} \right|_{\{q_i\}=0} q_i q_j \tag{2.23}$$

$$= \frac{1}{2} m \omega_z^2 \left[\sum_{i=1}^{N} \left(\frac{dq_i}{dT} \right)^2 - \sum_{i,j=1}^{N} A_{ij} q_i q_j \right] \tag{2.24}$$

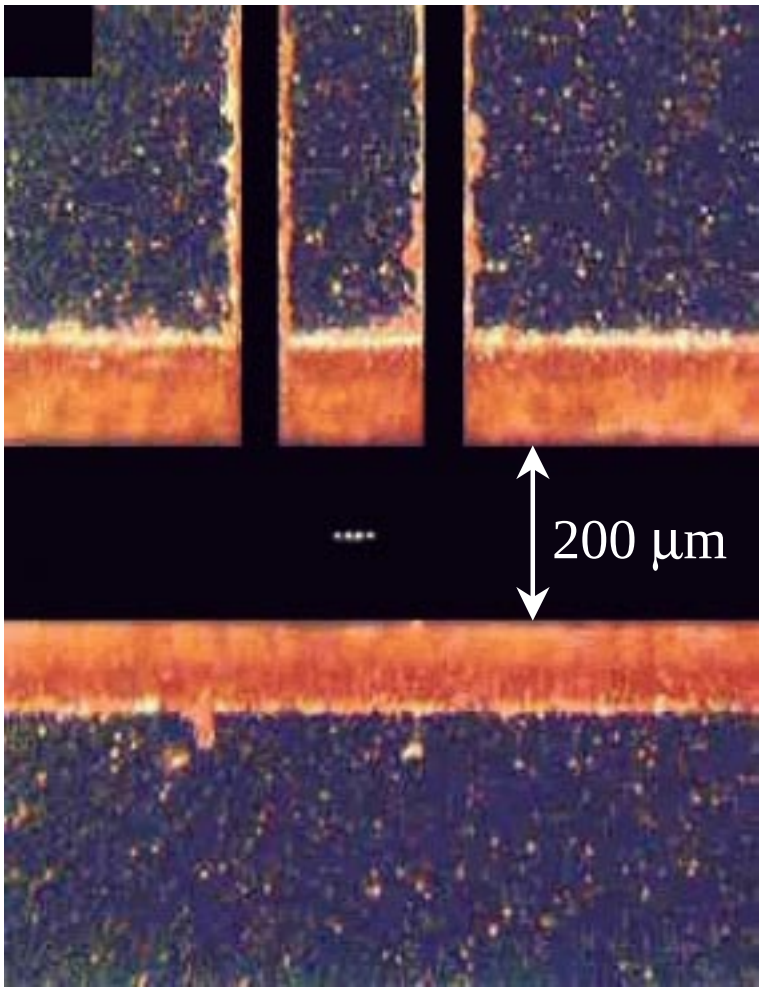

Figure 2.3: A string of four ions in the linear trap.

$$A_{ij} = \begin{cases} 1 + 2\sum\limits_{\substack{k=1 \\ k\neq i}}^{N} \dfrac{1}{|u_i - u_k|^3} & i = j \\ -2\dfrac{1}{|u_i - u_j|^3} & i \neq j \end{cases} \tag{2.25}$$

where $T = \omega_z t$ is a normalized time. To find the normal modes, we solve the eigenvalue equation

$$\sum_{j=1}^{N} A_{ij} v_j^{(k)} = \xi_k^2 v_i^{(k)} \tag{2.26}$$

for the frequencies ξ_k and (orthonormal) eigenvectors $\vec{v}^{(k)}$ of the N normal modes. In terms of the physical time t, the frequency of the kth mode is $\omega_z \xi_k$. If the kth mode is excited with an amplitude C, the ith ion moves according to

$$q_i(t) = \mathrm{Re}\left[C v_i^{(k)} e^{i(\xi_k \omega_z t + \phi_k)}\right] \tag{2.27}$$

where ϕ_k is a constant phase. For two, three, and four ions the normal mode eigenvectors and eigenvalues are given in Table 2.2. The lowest-frequency mode is always the center-of-mass (COM) mode, in which the ion string moves as a unit, with no relative motion between the ions. The Coulomb interaction then has no effect on the dynamics of the COM mode, so the COM frequency is just equal to the single-ion trap frequency ω_z. Because of the symmetry of the ion string about $z = 0$, the ions' relative amplitudes of motion in a given mode are either symmetric or antisymmetric about the center of the string, as seen in Table 2.2.

So far we have only considered the N normal modes of oscillation along the trap axis, but there are $2N$ more normal modes of the ion string involving displacement along $\hat{x}, \hat{y}$. We will treat the motion along $\hat{x}$; the analysis is similar for the motion along $\hat{y}$. The small displacements x_i are governed by the normalized Lagrangian

Table 2.2: Normal mode eigenvalues ξ_k and eigenvectors $\vec{v}^{(k)}$ for ion motion along $\hat{z}$, for two, three, and four ions.

N	ξ_k	$\vec{v}^{(k)}$				Name
2	1	$1/\sqrt{2}$	$1/\sqrt{2}$			COM
	$\sqrt{3}$	$-1/\sqrt{2}$	$1/\sqrt{2}$			Stretch
3	1	$1/\sqrt{3}$	$1/\sqrt{3}$	$1/\sqrt{3}$		COM
	$\sqrt{3}$	$-1/\sqrt{2}$	0	$1/\sqrt{2}$		Stretch
	$\sqrt{29/5}$	$1/\sqrt{6}$	$-2/\sqrt{6}$	$1/\sqrt{6}$		Egyptian
4	1	1/2	1/2	1/2	1/2	COM
	$\sqrt{3}$	−0.674	−0.213	0.213	0.674	Stretch 1
	2.41	1/2	−1/2	−1/2	1/2	Stretch 2
	3.05	−0.213	0.674	−0.674	0.213	Stretch 3

$$L = \frac{1}{2}\sum_{i=1}^{N}\left(\frac{dx_i}{dT}\right)^2 - \frac{1}{2}\sum_{i,j=1}^{N} B_{ij}x_i x_j \tag{2.28}$$

$$B_{ij} = \begin{cases} \epsilon^2 - \frac{1}{2} - \sum_{k=1,\neq i}^{N} \frac{1}{|u_i - u_k|^3} & i = j \\ \frac{1}{|u_i - u_j|^3} & i \neq j \end{cases} \tag{2.29}$$

$$\tag{2.30}$$

where $\varepsilon^2 - 1/2 \equiv (\omega_x/\omega_z)^2$ and ω_x is the secular frequency along $\hat{x}$. This peculiar definition will come in handy later (see Section 7.4.2). Note that the linearized Coulomb terms $|u_i - u_j|^{-3}$ enter into B_{ij} (Eq. 2.29) differently than for A_{ij} (Eq. 2.25) because the ion string extends along $\hat{z}$. In general, the Coulomb interaction also couples motion along $\hat{x}$ to motion along $\hat{z}$, but for the string configuration the Coulomb forces are all directed along $\hat{z}$ when the ions are at rest, decoupling the $\hat{x}$ motion from the $\hat{z}$ motion. This decoupling considerably simplifies our entangling gate (see Section 5.)

The normal mode eigenvalues $\xi^{(x)}$ and eigenvectors $\vec{v}^{(x;k)}$ can now be found by solving the counterpart of Eq. (2.26). The frequency of the kth mode in terms of the physical time t is then $\omega_x \xi_k^{(x)}$ and the motion of the ions is described by the counterpart of Eq. (2.27). Again we find a COM mode, but in this case the COM mode is not necessarily the lowest-frequency mode. For $\alpha = (\omega_z/\omega_x)^2$ larger than some N-dependent critical value α_0, the ion string breaks into a "zigzag" in which neighboring ions are displaced from the RF node in opposite directions. The critical value α_0 occurs at the smallest value of α for which $\det B_{ij} = 0$, corresponding to a motional mode along $\hat{x}$ with zero frequency, i.e. an unstable mode. The zigzag transition has been observed in detail by Enzer et al. [12], who found good agreement between experimental and theoretical values for α_0.

It is easy to quantize the normal modes, since each mode is just a simple harmonic oscillator. We consider only the axial modes for simplicity. Writing the operator for small displacements of the ith ion as $\mathbf{x}_i$ and the conjugate momentum as $\mathbf{p}_i$, we define the annihilation operator $\mathbf{a}_k$ for the kth mode in the usual way:

$$\mathbf{a}_k = \sqrt{\frac{Nm\xi_k\omega_z}{2}} \sum_{i=1}^{N} v_k^{(i)} \left(\mathbf{x}_i + \frac{i}{Nm\xi_k\omega_z} \mathbf{p}_i \right) \tag{2.31}$$

For our purposes it is sufficient to treat the micromotion classically, as described at the beginning of Section 2.1.2.

2.2 Electrode Structures for RF Traps

2.2.1 Micromachined Linear Trap

Most of the experiments described here used linear RF traps [21, 22] constructed using micromachined alumina substrates. Each trap consisted of a pair of substrate wafers bonded together. The wafers were laser-machined and coated with gold on parts of their surfaces to form electrode structures. The gold coating consisted of a 25 nm sticking layer of titanium evaporated directly onto the alumina with a layer of gold 0.25 to 0.75 μm thick evaporated onto the titanium. A schematic of an assembled trap structure is shown in Fig. 2.4. Each wafer was 1.5 cm long (along the direction of the wide slot), 1.0 cm wide, and 125 μm thick. The single wide slot on each wafer was 2 mm long and 200 μm wide, while the two thin slots were 20 μm wide and about 0.5 mm long. The edges of the wide slots were bevelled at 45°, with the narrow (200 μm) side nearer the ions. The electrode structures on the two wafers are mirror-images of each other under reflection about the wide slot. The wafers were bonded together using glass frit paste. To control the distance between the trap wafers, two alumina spacer wafers were inserted between the trap wafers, one at each end of the trap wafers.

Table 2.3: Spacing between wafers and thickness of evaporated gold layers for the linear traps.

Trap	Wafer spacing (μm)	Gold thickness (μm)
#1	250	0.25
#2	250	0.75
#3	375	0.75

Three such traps were constructed for the experiments described here. The traps varied in the spacing between wafers and the thickness of the evaporated gold layers, as detailed in Table 2.3. In each case, gold wires connected the DC electrodes on the pair of trap wafers to a nearby RF filter board constructed on thicker alumina wafers (10 mm $\times$ 7 mm $\times$ 0.2 mm). Surface-mount resistors (1 kΩ) and capacitors (800 pF) were bonded to the RF board to form low-pass RC filters (corner frequency 200 kHz). These filters provided the RF grounding for the DC electrodes. The filters also attenuated externally injected electronic noise at the ion motional frequencies. Such noise can lead to ion heating (Section 7.4). For trap #1, two identical stages of RC filtering were used, while only one stage was used for traps #2 and #3. Since the RF electrodes were electrically connected to the $\lambda/4$ RF resonator in each case (see Section 2.3), they were DC grounded.

2.2.2 Conventional Paul Trap

Some of the heating data presented in Section 7.4 was obtained using Paul traps [23, 24] of the ring-and-fork variety [25]. A schematic of such a trap is shown in Fig. 2.5. Applying an RF voltage V_{RF} across the electrode structure creates a three-dimensional RF quadrupole potential $\phi_{\mathrm{RF}} \propto V_{\mathrm{RF}}(z^2 - \alpha x^2 - (1-\alpha)y^2)/R^2$. Here R is a characteristic length scale for the

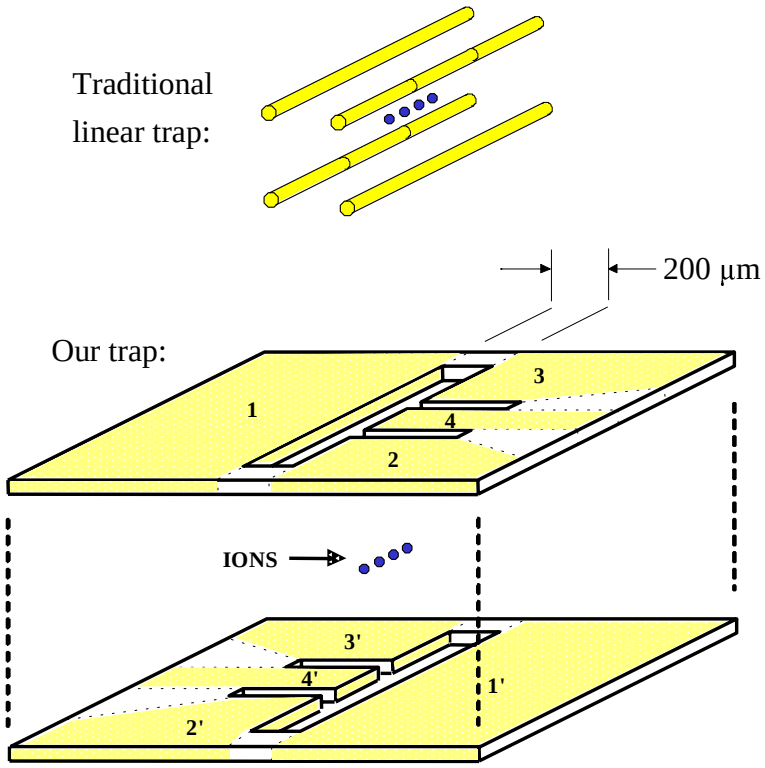

Figure 2.4: Schematic of a micromachined linear trap.

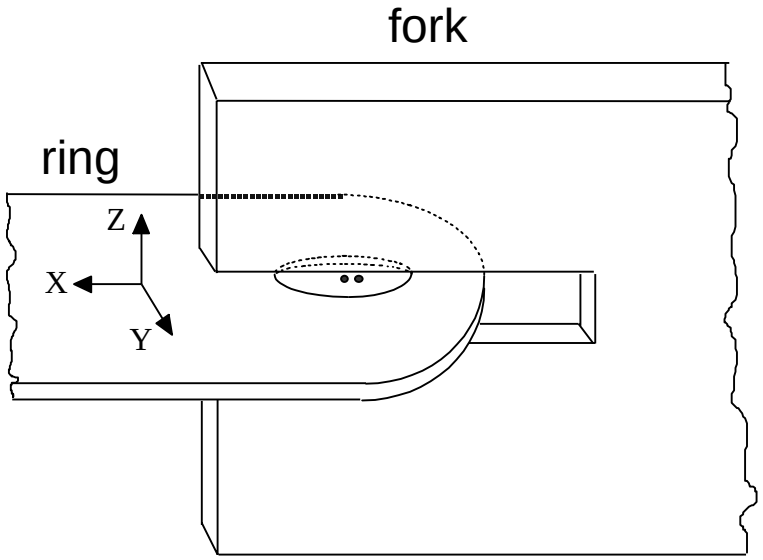

Figure 2.5: Electrode structure of a ring-and-fork Paul trap.

size and spacing of the trap electrodes and α is a dimensionless parameter depending on the ellipticity of the ring electrode ($\alpha \approx 0.4$ for a circular ring.) By convention, the $\hat{z}$ axis is taken perpendicular to the plane of the ring electrode. The RF potential traps ions by the mechanism described in Section 2.1.1. To tune the secular frequency, one applies an additional DC voltage V_{DC} across the electrodes, which adds a DC potential $\phi_{\mathrm{DC}} \propto V_{\mathrm{DC}}(z^2 - \alpha x^2 - (1-\alpha)y^2)/R^2$. The DC potential alters the secular frequency as described in Section 2.1.1. Details of the particular Paul traps used in our experiments are given in Section 7.4; typically the trap dimensions were on the order of a few hundred μm.

2.2.3 Silicon Linear Trap

During my tenure as a student, we attempted to construct a trap from micromachined silicon. Such a trap has two attractive characteristics: its electrode surfaces are extremely smooth, and the fabrication procedure should allow us to make extremely complicated electrode

structures. The electrode surfaces for the traps described above were generally quite rough on the scale of a few microns (see Fig. 2.8). The association of heating with surface effects (Sec. 7.4) suggests that the heating mechanism might depend on this roughness. With wet-etching techniques, one can obtain nearly atomically smooth surfaces, possibly eliminating the heating.

Easy fabrication techniques for complicated electrode structures will become important for our experiment in the near future. We plan to scale up the small quantum register described in this thesis by constructing a large array of interconnected ion traps, as schematically depicted in Figure 2.6. In this "quantum CCD" model, applying voltages to the DC electrodes shown in the figure allows us to shuttle ions from place to place in the array and pick out small sets of ions for quantum logic operations. Fabricating these structures by the techniques of Section 2.2.1 will eventually become impractical. However, the lithographic methods developed for silicon micromachining already routinely produce much more complicated and delicate structures.

The proposed design uses heavily boron-doped $\langle 100 \rangle$-cut Si wafers as the starting point for trap fabrication. The wafers were 100 μm thick. We used wafers with resistivity $\sim 1.5 \times 10^{-4} \Omega$ m, so the Si was essentially metallic. We planned to stack three Si layers together, rather than the two layers used in Section 2.2.1), so that the middle layer carried DC voltage only, while the outer layers carried the RF voltage. Flat pieces of Corning 7070 glass, a borosilicate glass with low RF loss, was used as an insulating spacer between the layers. We could attach the Si rigidly to the glass using the technique of anodic bonding, which is commonly used in the semiconductor industry. To make a bond, we heated the glass and Si pieces to about 450 $^\circ$ C and applied $\sim$ 1 kV between the Si and the glass for several minutes. The bond formed by this process was very strong; bonded pieces would break sooner than be pried apart. It was essential to use highly polished Si and glass pieces. A specification of 60/40 scratch/dig

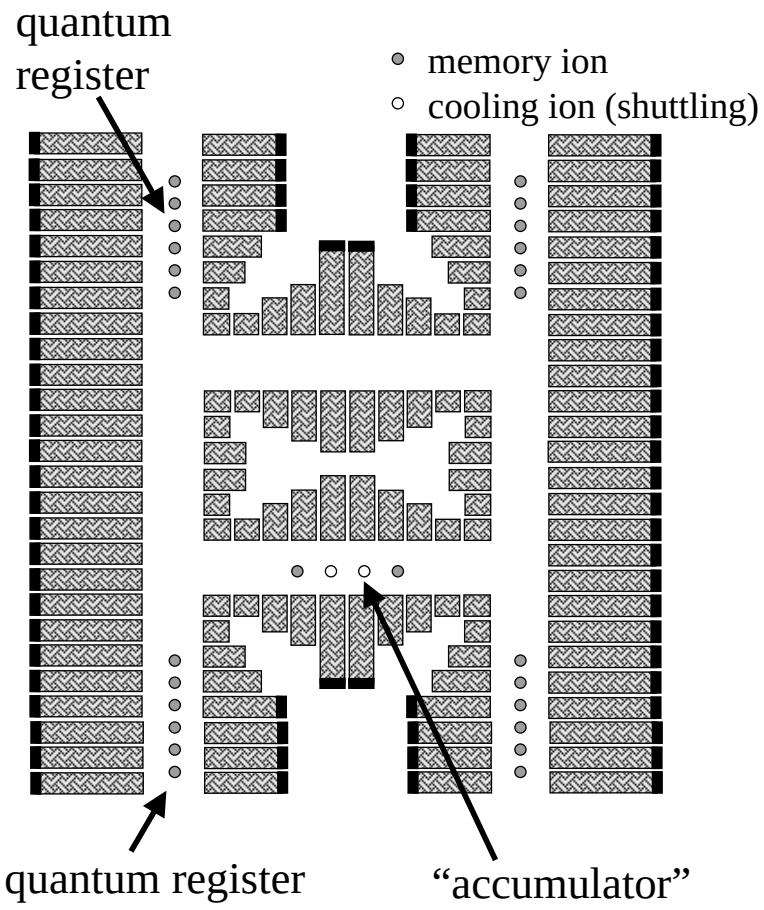

Figure 2.6: Schematic of the proposed “quantum CCD” architecture for a large-scale ion-trap quantum computer. The logic ions, which encode the quantum information, are held in a storage region. To perform a logic operation, we shuttle the relevant logic ions into an accumulator region, where they interact with lasers. Auxiliary ions sympathetically cool the logic ions (see Sec. 7.4.2).

for the glass and standard wafer polishing for the Si was sufficient. The pieces also had to be extremely clean. Standard optics-cleaning procedures with spectroscopic-grade methanol were ineffective. Instead, we cleaned the pieces by rinsing with VLSI-grade methanol, then VLSI-grade isopropanol, then deionized water ($\sim 15\text{M}\Omega$ cm resistivity).

To test the RF characteristics of our design, we applied up to 10 W of RF power to a test piece through the external resonator used for the double Paul trap (see Sec. 2.3). The test piece consisted of two Si pieces spaced by a piece of Corning 7070 glass. The glass was 175 μm thick, the thickness used in the full design. The resonance width was the same with the test piece as without it, implying that little power was dissipated in the test piece. In contrast, replacing the Corning 7070 glass with the more common Corning 7740 (Pyrex) caused severe broadening of the resonance and heating of the test piece at RF powers of ~ 1 W.

To construct the DC and RF electrode layers, we wet-etched slots 200 μm wide and 2 mm long into the wafers and diced the wafers into pieces. The DC pieces measured 1 cm square, while the RF pieces were 1 mm wide and 8 mm long. We used a KOH-based anisotropic etchant and etched the wafers from both sides. Figure 2.7 shows a schematic cross-sectional view of the slot sidewalls produced in this way. The slot dimensions above refer to the closest distance between the slot sidewalls.

After the first etch, we isotropically etched the wafers with hydrofluoric acid, removing several μm of Si, to soften any sharp edges left by the anisotropic etch. The resulting electrode surfaces were smooth on the micron scale. Figure 2.8 shows a scanning electron micrograph of a typical etched electrode surface.

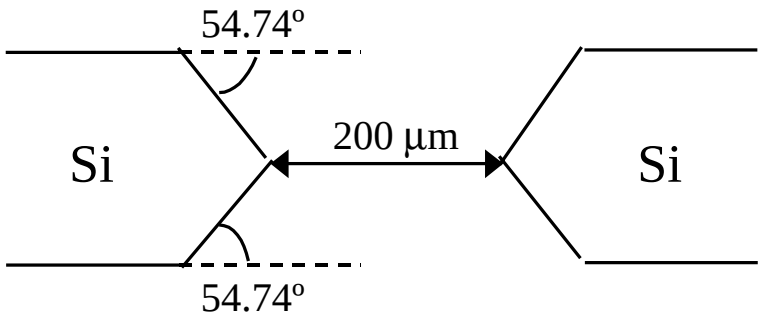

Figure 2.7: Schematic cross-sectional view of the slot sidewalls produced by the anisotropic etch. The angles shown result from the crystal lattice structure of the silicon. We measure slot dimensions as the closest distance between sidewalls.

To produce the separate DC electrodes for axial confinement of the ions, we first bonded the DC piece to two pieces of 7070 glass, making sure that the glass was at least 2 mm away from the slot edges. We then used a dicing saw to make two diagonal cuts of width ~ 40 μm across the DC piece. The cuts were at about 45° to the long axis of the slot and intersected at the geometric center of the slot. The dicing saw cut completely through the Si, but cut only slightly into the glass below. The glass was positioned so that the four pieces of Si separated by the cuts were rigidly supported on the glass. The cut sidewalls were rougher than the etched surfaces, but fields originating at the sidewalls would likely be shielded from the ions by the rest of the electrode structure, so we felt that the cut roughness would not induce heating (see Sec. 7.4). After making the saw cuts, we bonded two more pieces of glass to the other side of the DC piece, and bonded two "crossbar" pieces of 500 μm thick Si across these glass pieces for structural support. Without the crossbars, the structure was extremely delicate. Figure 2.9 shows a schematic of the completed DC electrode structure.

This project is currently not finished. We produced four DC electrode structures as outlined above, and etched a large number of RF pieces. The design called for bonding one RF

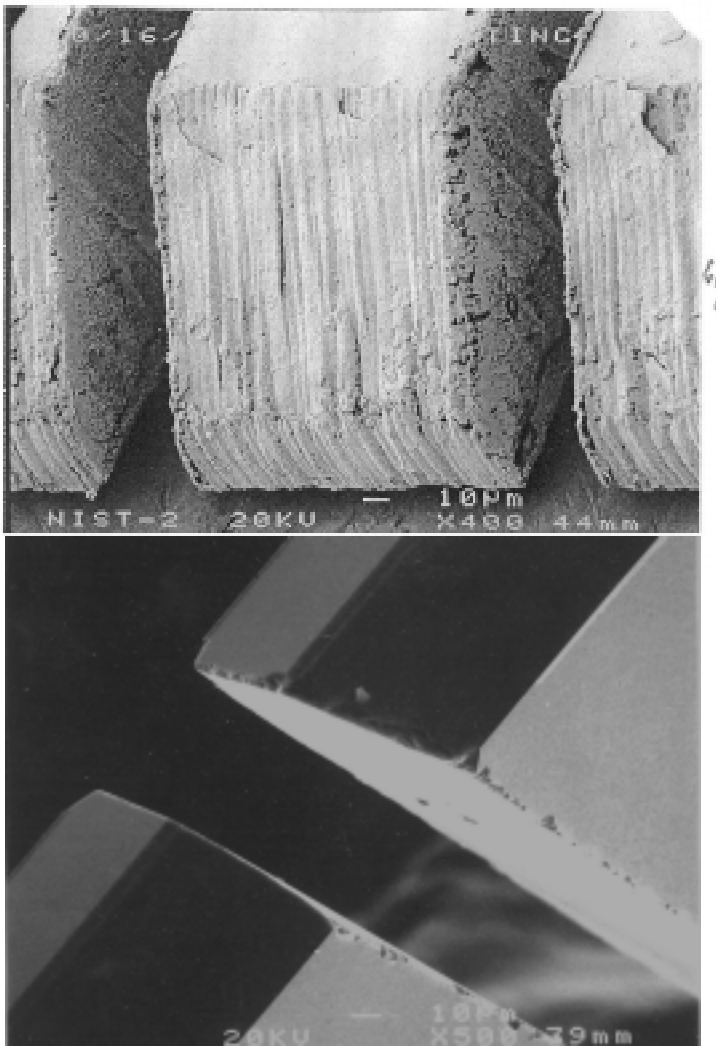

Figure 2.8: Scanning electron micrographs of a typical electrode surface of an alumina-based trap (top) and a silicon trap piece after the isotropic etch (bottom). Each image is $\sim 200\mu$m across.

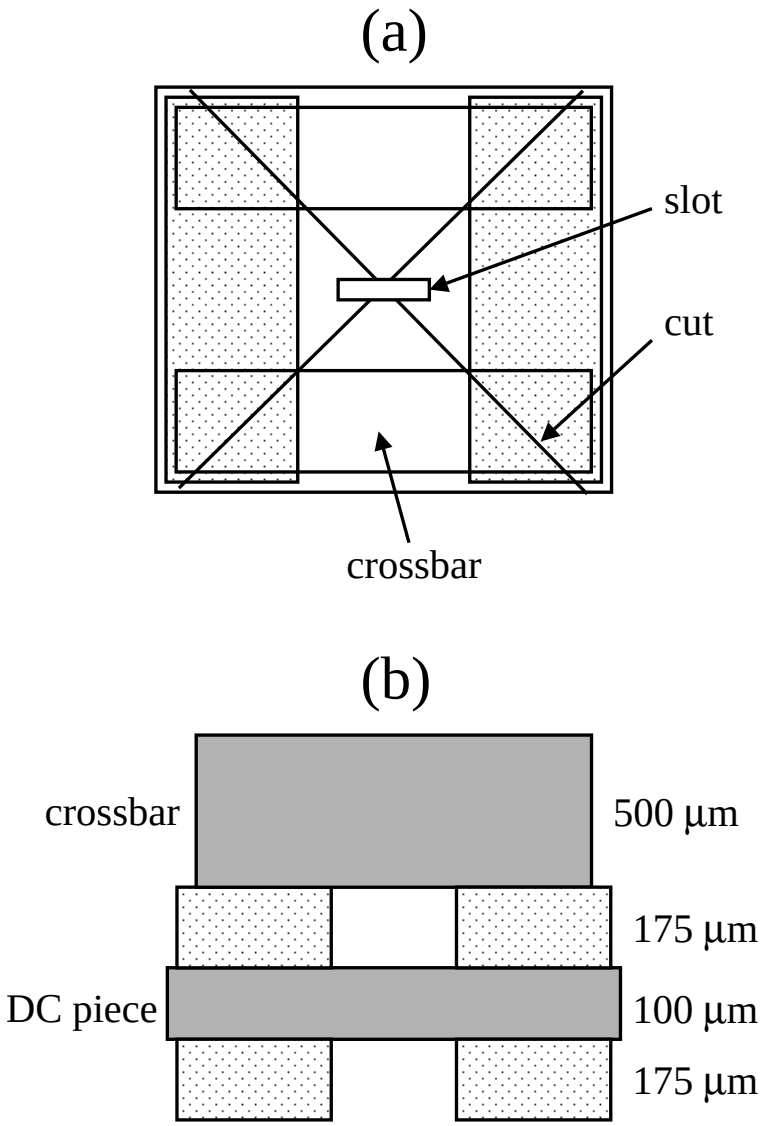

Figure 2.9: Schematic of the completed DC electrode structure. Not to scale. (a) Top view. Dots indicate glass pieces. (b) Side view. Gray shading: Si pieces. No shading: glass pieces. Dimensions are thicknesses.

piece to each side of a DC structure, with all three slits aligned. By making the RF pieces small, we hoped to avoid the capacitance associated with large structures, which lowers the drive frequency and resonator Q (see Sec. 2.3). To make electrical connections to the structure, we evaporated patches of gold onto the DC and RF pieces in the way described in Section 2.2.1. We were able to robustly gap-weld 25μm thick gold ribbon to these patches. We also intended to bond another mask layer to one side of the three-layer structure to avoid plating of Be from the ovens onto the electrodes (see Sec. 2.5). These mask layers were 1 cm square pieces of Si wafer with an etched slot 100 μm wide and 1 mm long and were to be bonded to the crossbars with glass. The center of the mask slot was to be aligned to the center of the RF and DC slots. Figure 2.10 shows a schematic cross-sectional view of the planned trap structure. Assuming the Be oven was placed 5 cm from the trap, a 1 mm aperture placed in front of the oven would suffice to keep atoms passing through the mask slot from hitting the electrode surfaces.

2.3 RF Resonators

Attaining high secular frequencies in RF traps requires the application of large RF voltages at the drive frequency, typically several hundred volts for the traps described here. Since most commercial RF generators are impedance-matched for a 50 Ω load, it is very inefficient to drive the trap electrodes directly from such a generator. Instead, we used a $\lambda/4$ coaxial RF resonator [25] as a step-up transformer to match the 50 Ω generator to the trap impedance, which is usually capacitive on the order of several pF. A schematic of such a resonator is shown in Fig. 2.11. If no trap is attached to the resonator, the fundamental resonant RF wavelength is $\lambda = 4L$ in the ideal case, where L is the length of the resonator; thus the term "$\lambda/4$ resonator". Attaching the trap lowers the resonant frequency and the Q of the resonator due to trap capacitance and leakage current.

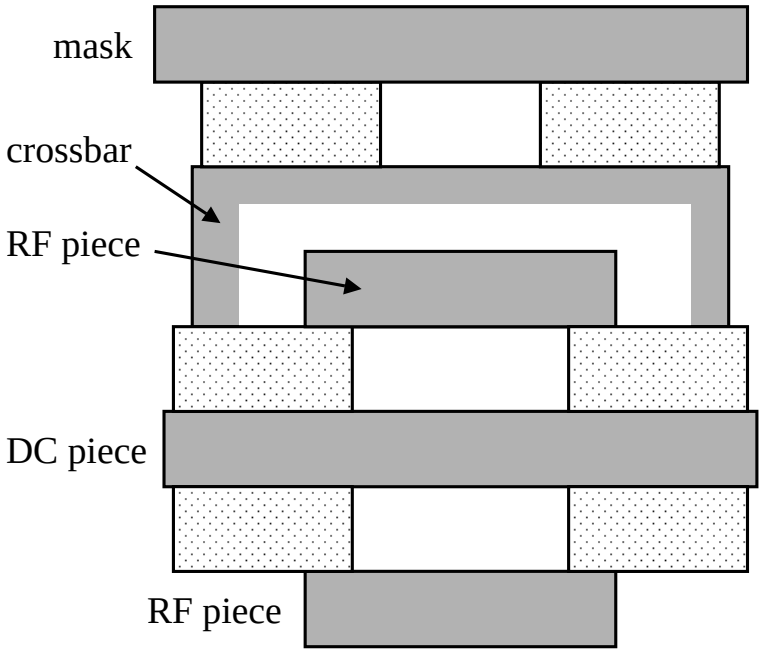

Figure 2.10: Schematic cross-section of the planned trap structure. Not to scale. Gray shading: Si pieces. Dots: glass pieces. Crossbars are partially cut away for clarity.

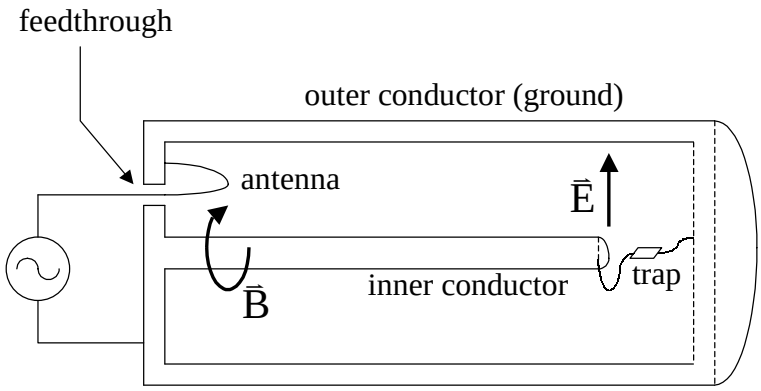

Figure 2.11: Schematic of a $\lambda/4$ coaxial resonator. The antenna couples power from the RF generator into the resonator. The high RF voltage developed at the other end of the resonator drives the trap electrodes.

To couple power into the resonator, we used a commercial RF generator to drive a loop antenna mounted at the opposite end of the resonator from the trap. At the antenna end of the resonator, the center conductor was connected to the outer conductor, so at this end the magnetic field was comparatively strong and the electric field was weak, allowing coupling through the magnetic field generated by the loop antenna. By adjusting the size and position of the loop antenna, reflected powers as low as 0.25% of the input power were obtained on resonance. Effectively, then, the RF generator looks into a 50 Ω load on resonance. At the trap end of the antenna, the electric field was strong and the magnetic field was weak, providing the large voltages we required.

The resonators for all the linear traps and all but one of the conventional Paul traps were constructed of oxygen-free high-conductivity (OFHC) copper and were mounted inside the vacuum system (see Section 2.4) to avoid breakdowns at the high-voltage end of the resonator. This arrangement also minimizes the high-voltage demands on the RF vacuum feedthrough. The feedthrough can be modeled as a capacitor in parallel with a large shunt resistance. If the

feedthrough were close to the high-voltage end, we would need to design it so that breakdowns would not occur. Further, the feedthrough capacitance could significantly lower the resonant frequency. Finally, more power would be dissipated because of the higher voltages across the feedthrough. All these effects are negligible in the current arrangement.

The vacuum-mounted resonators used with linear traps #2 and #3 had an inner conductor diameter of 0.250" (6.35 mm), an outer conductor ID of 0.750" (19.05 mm), an outer conductor OD of 1.000" (25.40 mm), and an inner conductor length of 11.7" (297.2 mm). The outer conductor was slightly longer than the inner conductor to leave room for the trap. The resonant frequency was about 250 MHz without the trap and 230 MHz with the trap. These resonators displayed loaded Q's of about 600 without the trap and about 500 with the trap.

The resonator used with linear trap #1 differed from the others in that an alumina tube was inserted between the inner and outer conductors to reduce the resonant frequency. With the alumina tube inserted, the resonant frequency was 115 MHz without the trap and 113 MHz with the trap. The loaded Q was about 200 without the trap and 150 with the trap. We had hoped that the reduction in resonant frequency would increase the secular frequency (see Eq. 2.11), but because of the lower Q we were unable to maintain the same RF voltage at the trap, so that we realized no net gain in secular frequency from this maneuver.

For the experiments with the "double" Paul trap (see Section 7.4) we mounted the resonator outside the vacuum system. A two-pin RF feedthrough connected the resonator to the trap. This tactic enabled us to construct a number of resonators with different resonant frequencies, so that we could vary the drive frequency fairly easily. All these resonators were similar to

that shown in Fig. 2.11. The resonator used for the data in Section 7.4 had a resonant frequency of 148 MHz and a Q of about 230 when attached to the feedthrough.

The RF voltages attainable at the trap were usually limited by electrical breakdown inside the vacuum chamber. For the linear traps, electrical breakdowns at the trap occurred at several MV/m, corresponding to several hundred volts of RF. The breakdown path appeared to be the shortest path joining RF and DC electrodes. Breakdown voltages for a parallel-plate geometry under comparable conditions occur at fields of about 25 MV/m [26]. We therefore do not expect to significantly increase the field strength at the trap in the near future. However, breakdowns also occurred in the body of the resonator, lowering the Q of the resonator and limiting the trap voltage to yet smaller values. The location of the breakdowns observed is consistent with the "multipactor" effect [27]. In this process, the RF voltage is such that an electron starting from the inner conductor arrives at the outer conductor (or vice versa) in half the period of the RF drive. The electron impact on the conductor creates secondary electrons, which are again accelerated by the RF, and the resulting avalanche leads to electrical breakdown. This phenomenon was only observed for the vacuum-mounted resonators and at locations near the input end of the resonators. In the external resonator, the electrons were stopped by air and the avalanche could not occur. To reduce the likelihood of breakdowns in the vacuum-mounted resonators, we initially applied a few mW of RF and slowly increased the RF power to several watts over a period of a few days. This procedure presumably reduced the secondary electron emission coefficient as the plasma discharge cleaned the resonator surfaces.

2.4 Vacuum System

The vacuum system for the linear traps and all but one of the Paul traps consisted of a quartz envelope containing the resonator and trap, an ion pump, and a titanium sublimation pump (TSP). The ion pump had a pumping speed of 22 L/s and was run continuously while the trap was in use. The titanium sublimation pump (TSP) was run about once a week for a few minutes, coating the inside of the TSP cartridge with titanium for gettering. Optical-quality quartz windows were attached to the quartz envelope (using glass frit) for optical access. The vacuum system was assembled using standard UHV conflat fittings.

After assembly, the vacuum system was roughed out with a commercial turbopump system, then baked in a home-built oven at 350° for several days into a large external ion pump. During this time the pressure was monitored with the internal ion gauge. The pressure decreased to a steady-state value of $\sim 10^{-7} - 10^{-8}$ bar. The connection to the external ion pump was then closed off, the internal ion pump was turned on, and the system was baked for another day or two, until the pressure leveled off again. Typically the pressure decreased by another order of magnitude during this time. The system was then brought back down to room temperature, which decreased the pressure to $10^{-9} - 10^{-10}$ bar. At this point the TSP was run several times, eventually yielding pressures on the order of several $\times 10^{-11}$ bar. These pressures are near the limit of sensitivity for ion gauges, so it was difficult to compare the results from the various bakes. In practice, we used the ion lifetime to judge pressure; while this hardly provides a quantitative measure of the pressure, the ion lifetime, not the pressure itself, was the quantity of interest. Typically we would run the TSP if the ion lifetime fell below several hours. Lifetimes of ten hours were not uncommon.

For the "double" Paul trap, the resonator was mounted outside the vacuum system (see Section 2.3). We replaced the quartz envelope with a commercial stainless steel vacuum chamber shaped roughly like a hemisphere, which held the trap. This chamber had one large sapphire window mounted to the flat side of the hemisphere and two small sapphire windows. These windows exhibited much more birefringence than the quartz windows, presumably because the absorption edge of sapphire is closer to the laser wavelength of 313 nm. Using quartz windows, however, would have required glass-to-metal seals several inches long.

Because of the long ion lifetimes and the lack of independent measures for gas partial pressures in the system, the effects of background gas are difficult to investigate rigorously. The estimated rate for elastic collisions of trapped ions with background gas is about one per minute at typical pressures [2]. Since the repetition rate of the experiment was usually at least several hundred Hz, elastic collisions were not expected to affect our data. The only identifiable trap "loss" mechanism was the reaction $Be^+ + H \rightarrow BeH^+$ [28], as determined from measurements of normal-mode frequencies of ion crystals before and after the reaction.

2.5 Ion Source

We produced $^9Be^+$ ions by electron bombardment of neutral Be. Probably only the Be atoms that were ionized inside the trapping region were actually trapped, since the large RF fields at the boundary of the trapping region tended to accelerate ions trying to enter the trap. However, it is difficult to verify this idea. The neutral Be source consisted of Be wire (50 μm diameter) helically wrapped around a coil of tungsten wire (several mm long, 0.1 mm diameter) with Be wire winding pitch equal to the Be wire thickness. Resistive heating of the tungsten wire with current ~ 1 A caused beryllium to evaporate from the Be wire.

Beryllium plating of the trap wafer can create electrical shorts between electrodes. To prevent this, we masked off the trap wafer with a copper baffle. The baffle had a hole 2.3 mm wide drilled in it to allow beryllium to reach the trap, and was positioned a few mm away from the trap. The baffle was electrically isolated from the other trap components and was electrically connected to the DC feedthrough. This allowed us to apply voltage to the baffle for compensation of ambient static electric fields (see Section 2.1.1).

The electrons required for ionization of the neutral Be were produced by electron guns made of pieces of tantalum foil 4 mm long, 1 mm wide, and 12 μm thick. To operate an e-gun, we biased it to a negative voltage of 50-100 volts relative to the vacuum chamber and passed several amps of heating current through the 4 mm length of the gun to induce thermionic emission. The biasing ensured that the emitted electrons left the vicinity; otherwise space-charge effects reduced the emission current. We set the bias voltage to roughly maximize the ionization cross-section for Be. Typically we adjusted the heating current so as to give 20-100 μA of emission current from the gun, of which a few nA was collected on the trap electrodes.

To load ions into the trap, we operated the Be oven and the electron gun simultaneously. We could adjust the loading rate by varying the oven current and the electron emission current. Usually we chose a loading rate of about one ion per minute, so as to easily control the total number of ions in the trap (recall that our experiments involved no more than four ions.) However, we could increase the loading rate to perhaps ten ions per minute by increasing the oven current by about 20%.

Chapter 3

Laser-Ion Interactions

We used laser light near 313 nm to manipulate the internal and motional states of the trapped $^9Be^+$ ions. Light nearly resonant with atomic transitions Doppler-cooled the ions and provided initialization of the internal state into the $|\downarrow\rangle$ qubit level. Nonresonant light induced stimulated Raman transitions which coherently couple the internal states to each other and to the motional state of the ions. These Raman transitions allowed us to cool the ion motion to the ground state with high efficiency.

3.1 Atomic Structure of $^9Be^+$

The $^9Be^+$ ion has one valence electron, making it structurally similar to the neutral alkali atoms. The energy levels of $^9Be^+$ relevant to these experiments are the 2s $^2S_{1/2}$ ground state and the 2p $^2P_{1/2}$, $^2P_{3/2}$ excited electronic states. An energy-level diagram is shown in Fig. 3.1. The fine-structure splitting between the $^2P_{1/2}$ and $^2P_{3/2}$ states is 197 GHz. The nuclear spin of $^9Be^+$ is 3/2, inducing hyperfine splitting of 1.25 GHz in the $^2S_{1/2}$ state and 237 MHz in the $^2P_{1/2}$ state [29]. The hyperfine splitting of the $^2P_{3/2}$ state is less than 1 MHz [30]. The $^2S_{1/2} \leftrightarrow {}^2P_{1/2}$ transition lies at 313.395 nm, while the $^2S_{1/2} \leftrightarrow {}^2P_{3/2}$ transition lies at 313.266 nm. Both transitions are dipole-allowed with radiative linewidths of 19.4 MHz. Transitions between hyperfine states in the $^2S_{1/2}$ manifold, however, have radiative lifetimes on the order of 10^{12} s [2], so we neglect these radiative decay processes throughout.

We usually used the 2s $^2S_{1/2}|F=2, m_F=-2\rangle$ and $|F=1, m_F=-1\rangle$ magnetic sublevels as qubit logic states. These are denoted $|\downarrow\rangle$ and $|\uparrow\rangle$ respectively, in analogy to the two states of a spin-1/2 particle. Magnetic field coils provided a quantization field of 165 μT directed along $-\hat{x}/\sqrt{2}+(\hat{y}-\hat{z})/2$, in the coordinate system of Figure 2.1. The Zeeman splitting of the magnetic sublevels is given by $\Delta E = g_F m_F \mu_B B$, where B is the magnetic field strength, $\mu_B = h \cdot 14.0$ kHz/μT is the Bohr magneton, and g_F is the Landé g-factor with $g_1 = -1/2$, $g_2 = +1/2$.

3.2 Logic State Initialization and Readout

Quantum computation requires the preparation of the computational register in a well-defined input state at the beginning of the computation and the efficient readout of the state of the register at the end of the computation. Thus, all the experiments described here began by initializing the ions to the $|\downarrow\rangle$ logic state and ended by detecting the number of ions in the $|\downarrow\rangle$ state. These tasks were accomplished by two laser beams, called "Blue Doppler" (BD) and "Red Doppler" (RD), which were nearly resonant with the $^2S_{1/2}$ $|F=2\rangle \leftrightarrow {}^2P_{3/2}$ and $^2S_{1/2}$ $|F=1\rangle \leftrightarrow {}^2P_{1/2}$ atomic transitions, respectively. The Zeeman splitting of the magnetic sublevels was about 24 MHz, comparable to the 19.4 MHz excited-state linewidth. Both beams propagated along the quantization axis $\vec{B}$ and were polarized σ^- (see Fig. 4.7 in Sec. 4.3.2 for a schematic rendering of the beam geometry.) At the beginning of each shot of an experiment, we applied the BD and RD beams at the same time for about 20 μs, then left RD on for an additional few μs. This procedure optically pumped the ions into the $|\downarrow\rangle$ state with a probability exceeding 99.9%. The extra few μs of RD ensured that the ions would not be pumped into a dark hyperfine superposition [31] in the event of imperfect BD or RD polarization. BD was always detuned from the exact $|\downarrow\rangle \leftrightarrow {}^2P_{3/2}$ resonance by 8 MHz to ensure that the ions were cooled to the Doppler cooling limit at the beginning of each shot. This detuning is optimal for

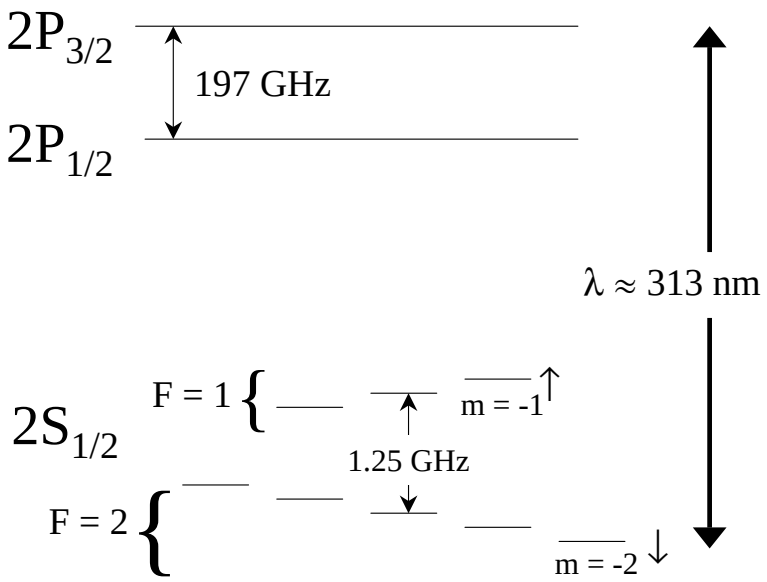

Figure 3.1: Partial energy level diagram of the $^9Be^+$ ion. The dipole-allowed S $\leftrightarrow |P\rangle$ transitions occur near 313 nm and decay with linewidth of 19.4 MHz. The ground-state hyperfine levels $|F = 2, m_F = -2\rangle$, $|F = 1, m_F = -1\rangle$ are used as qubit logic states and denoted $|\uparrow\rangle$ and $|\downarrow\rangle$ respectively. The hyperfine and magnetic structure of the P manifold is not shown.

Doppler cooling of $^9Be^+$ [32], as determined from temperature measurements on the cooled ions (see Sec. 3.3.4.)

We detected the number of ions in $|\downarrow\rangle$ by turning on BD for several hundred μs and detecting the scattered light on either a multichannel plate imager (MCP) or a photomultiplier tube (PMT). Assuming perfect σ^- polarization, an ion in $|\downarrow\rangle$ can make transitions only to the $|F = 3, m_F = -3\rangle$ hyperfine sublevel of the $^2P_{3/2}$ state. Dipole selection rules then force it to decay back to the $|F = 2, m_F = -2\rangle$ hyperfine sublevel, i.e. the $|\downarrow\rangle$ state. The number of photons scattered by a $|\downarrow\rangle$ ion on this cycling transition is limited only by the polarization of the BD beam. Since the linewidth of the $^2S_{1/2} \leftrightarrow {}^2P_{3/2}$ transition is 19.4 MHz and the hyperfine splitting is 1.25 GHz, the states $|\uparrow\rangle$ and $|\downarrow\rangle$ are spectrally well resolved. Thus we can illuminate the ion with BD for a long time, scattering many photons if the ion is in $|\downarrow\rangle$, but scattering very few if the ion is in $|\uparrow\rangle$. The detection duration is limited by off-resonant repumping of $|\uparrow\rangle$ to $|\downarrow\rangle$ by BD, which eventually causes an initially dark ion to scatter many photons. This technique for high-efficiency internal state discrimination is commonly used in studies of trapped ions [33, 34, 35].

By performing many repetitions, or shots, of an experiment and binning the results according to the number of photons detected, we can build up a histogram of the photon statistics for that experiment. Fig. 3.2 shows such a histogram for an ion prepared in $|\uparrow\rangle$, and another histogram for an ion prepared in $|\downarrow\rangle$. The two histograms are readily distinguished. We expect the $|\downarrow\rangle$ histogram to be Poissonian with $\overline{m}$ the mean number of photons detected. Non-Poissonian statistics for the $|\downarrow\rangle$ histogram indicated a problem with the experiment, for instance BD intensity fluctuations. The observed ratio of variance to mean for $|\downarrow\rangle$ histograms taken over 1000 shots varied randomly between about 0.95 and 1.05 when the experiment was running smoothly;

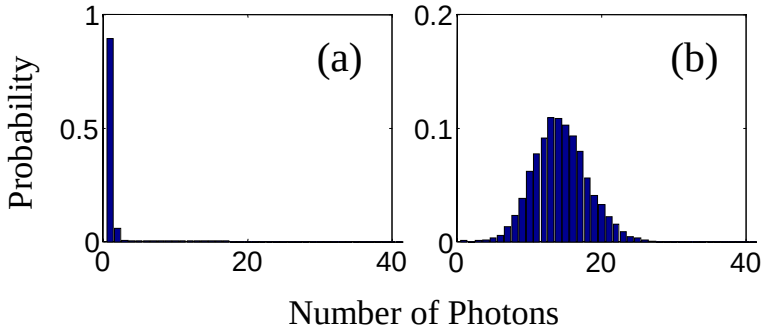

Figure 3.2: Histograms of the number of photons detected from a single ion over 1000 shots of the experiment. (a) Ion prepared in $|\uparrow\rangle$ for each shot. (b) Ion prepared in $|\downarrow\rangle$ for each shot.

the nominal value is 1. We discuss the distribution of the $|\uparrow\rangle$ histogram below.

In experiments with one ion, an experiment detected the ion in $|\downarrow\rangle$ on some shots and in $|\uparrow\rangle$ on others, for instance if we prepared the ion in a superposition state. A histogram exemplifying this situation is shown in Fig. 3.3. We fit such histograms to a weighted sum of two reference histograms, one giving the nominal count distribution for an ion in $|\downarrow\rangle$, the other for $|\uparrow\rangle$. In each shot of the experiment, the ion was projected into either the state $|\downarrow\rangle$ or the state $|\uparrow\rangle$, in accordance with the quantum measurement postulate, so fitting the histogram was similar to counting up the number of times that the ion was projected into $|\downarrow\rangle$ or $|\uparrow\rangle$ over the course of many experiments. On the other hand, if we wanted to read out the ion state on a shot-by-shot basis, we could set a discriminator at, say, 4 photons detected (for the case of Fig. 3.2). Then we considered the ion to be in state $|\downarrow\rangle$ if more than 4 photons were detected for a particular shot. The discriminator method was conceptually simpler but yielded lower signal-to-noise for the measurement of $|\downarrow\rangle$ and $|\uparrow\rangle$ probabilities than the histogram method, because it did not take into account the details of the count distributions in the overlap region between the $|\downarrow\rangle$ and $|\uparrow\rangle$ reference histograms. However, even using the discriminator method, the small overlap of the reference histograms permitted routine detection efficiencies of 98% in a single shot.

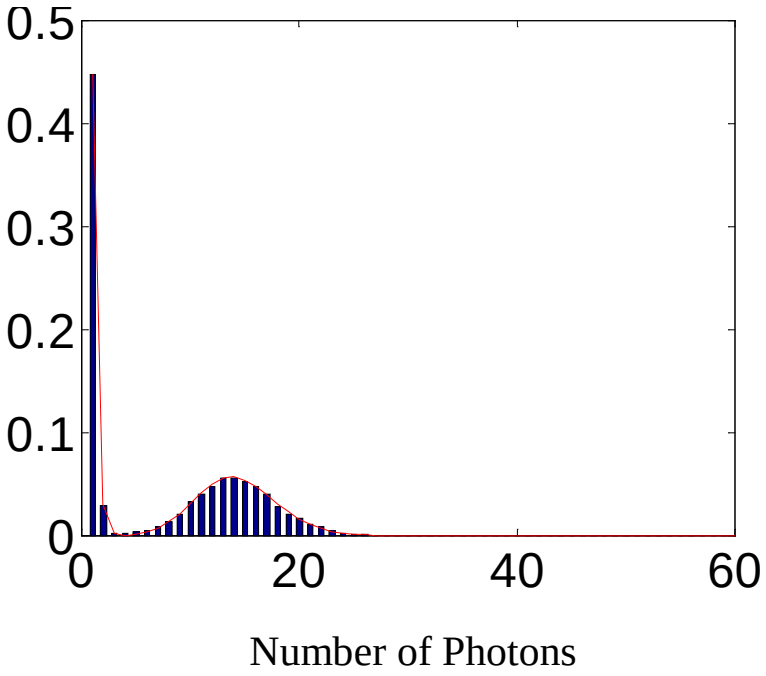

Figure 3.3: Histogram of the number of photons detected from a single ion prepared in a superposition of $|\downarrow\rangle$ and $|\uparrow\rangle$ over 1000 shots. The solid line is the best fit to the theoretical count distribution.

One limit to our readout technique was imperfect polarization of BD at the ion. To ensure good polarization, we linearly polarized the BD and RD beams and sent them through a $\lambda/4$ plate mounted on a precision rotation stage just before they pass into the vacuum system. To optimize the polarization, we monitored the ion fluorescence with BD continuously on and RD off. If the polarization was imperfect, the ion occasionally decayed from the $^2\mathrm{P}_{3/2}$ state to a state in the $^2\mathrm{S}_{1/2}\,|F=1\rangle$ manifold. The ion then stopped fluorescing until BD off-resonantly repumped it to the $^2\mathrm{S}_{1/2}\,|F=2\rangle$ manifold. We attempted to maximize the fluorescence under these conditions by adjusting the rotation angle and tilt of the $\lambda/4$ plate and by adjusting the direction of the quantizing magnetic field so that it lies exactly along the propagation direction of BD. This technique ensured that all but about a part in 10^5 of the BD intensity was σ^- polarized with respect to the ions. In principle, it is possible to completely eliminate this source of readout inefficiency.

The off-resonant repumping of $|\uparrow\rangle$ limited our readout efficiency from a more fundamental standpoint. The scattering rate of BD photons from $|\uparrow\rangle$ is determined solely by the linewidth of the $^2\mathrm{S}_{1/2} \leftrightarrow {}^2\mathrm{P}_{3/2}$ transition and the ground-state hyperfine splitting. If an ion in $|\uparrow\rangle$ scatters even one photon, the ion can decay from the $^2\mathrm{P}_{3/2}$ state into the ground $|\downarrow\rangle$ state. At that point it will begin to fluoresce brightly, so that we might mistakenly think that it was in $|\downarrow\rangle$ all along. The photon count distribution arising from this process is not trivial to calculate, since the transition from $|\uparrow\rangle$ to $|\downarrow\rangle$ occurs at a random moment during the detection interval. A detailed analysis can be found in [28]. In the absence of repumping, we should never detect photons for an ion in $|\uparrow\rangle$, but the repumping mechanism gives a probability α_p of detecting one or more photons. If β is the scattering rate of BD photons from the $|\uparrow\rangle$ state, we find [28]

$$\alpha_p \approx \frac{4\beta}{19\pi\zeta_{\mathrm{det}}\gamma}\overline{m}_0 \tag{3.1}$$

where ζ_{det} is the detection efficiency and $\Gamma = 2\pi \times 19.4$ MHz is the linewidth of the excited state.

The factor $\overline{m}_0$ is the mean number of photons detected if the ion is in the state $|\downarrow\rangle$. For $^9Be^+$ we find $\alpha_p \approx 1.35 \times 10^{-5}/\zeta_{\rm det}$. The detection efficiency for our experiment was $\zeta_{\rm det} \approx 8 \times 10^{-3}$ (see Sec. 4.5) and we typically had $\overline{m}_0 \approx 10$, so the actual value of α_p was ≈ 0.01. Of course, any stray light entering the detector would also increase the number of detected photons, but the limit set to spin detection efficiency by α_p is fundamental.

In experiments with multiple ions, we collected all the fluorescence from the ion string at once, making no attempt to spatially resolve the ions. Thus we detected only the number of ions in $|\downarrow\rangle$, rather than reading out the ions individually. Typically we collected histograms of photon count distribution as a function of an experimental parameter. In these cases we constructed reference histograms by fitting weighted sums of theoretical photon count distributions for zero, one,... ions in state $|\downarrow\rangle$ to a histogram created by averaging all the data histograms [28]. The free parameters in the theoretical distributions were the mean number of photons collected per ion in $|\downarrow\rangle$ and the mean number of photons due to background light. The effect of off-resonant repumping was included for each reference histogram, using a fixed value of α_p. Optical pumping due to imperfect BD polarization was not included in the fits. The weights in the fits to the data histograms then gave the probabilities $P_0, P_1, \ldots$ of finding zero ions in $|\downarrow\rangle$, one ion in $|\downarrow\rangle$, etc. An example histogram for four ions, including a fit to reference histograms, is shown in Fig. 3.4. The detection efficiency for this scheme decreased as the number of ions increases. For instance, the probability that an ion in $|\uparrow\rangle$ off-resonantly repumped to $|\downarrow\rangle$ was larger for a larger number of ions in $|\uparrow\rangle$. Pumping of an ion out of $|\downarrow\rangle$ due to imperfect polarization of BD was also more likely if we had many ions in $|\downarrow\rangle$. Histograms built up over 1000 shots yielded probabilities P_i with typical uncertainties of ± 0.01 for two ions and ± 0.02 for four ions. It is also possible to use the discriminator method for multiple ions, but the signal-to-noise is relatively low unless a more elaborate readout scheme is used (see Section 6.1).

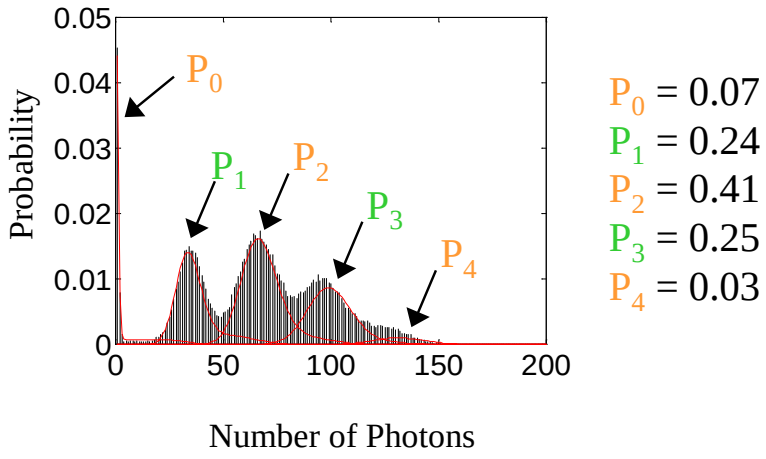

Figure 3.4: Histogram for four ions prepared in a superposition state. The solid line shows the best fit to a sum of reference histograms.

3.3 Coherent Coupling of Logic States

Quantum computation with the ion string required coherent manipulation of the ion internal and motional states. Two-photon stimulated Raman transitions provided this coherent coupling in our experiment. To drive Raman transitions between two hyperfine levels $|1\rangle$, $|2\rangle$ in the $^2S_{1/2}$ manifold, we applied two laser beams at ~ 313 nm with frequencies ω_1, ω_2 and wavevectors $\vec{k}_1$, $\vec{k}_2$. The electric fields of the beams are then

$$\vec{E}_j = \hat{\epsilon}_j E_j \cos(\vec{k}_j \cdot \vec{x} - \omega_j t + \varphi_j) \qquad j = 1, 2 \tag{3.2}$$

where E_j is the amplitude, $\hat{\epsilon}_j$ is the polarization and φ_j is the phase of the jth laser field. The Raman laser frequencies are typically detuned several tens of GHz from the nearest S $\leftrightarrow$ P resonance, so the amplitudes of the excited $|\mathrm{P}\rangle$ states remain small. Writing $\vec{\boldsymbol{\mu}}$ for the atomic dipole moment operator and setting $\hbar = 1$, we find the dipole interaction Hamiltonian

$$\mathbf{H}_{\mathrm{dip}} = -\vec{\boldsymbol{\mu}} \cdot (\vec{E}_1 + \vec{E}_2) \tag{3.3}$$

$$= \sum_{j=1,2} \boldsymbol{\Omega}_j e^{i(\vec{k}_j \cdot \vec{\mathbf{x}} + \varphi_j)} e^{-i\omega_j t} + \mathrm{h.c.} \tag{3.4}$$

where $\boldsymbol{\Omega}_j = -E_j \, \hat{\epsilon}_j \cdot \vec{\boldsymbol{\mu}}/2$. We use a convention in which E_j and all matrix elements of $\boldsymbol{\Omega}_j$ are real.

3.3.1 Three-Level Model of Raman Transitions

In general, each Raman beam will couple both the $|1\rangle$ and $|2\rangle$ states to several sublevels of the $|\mathrm{P}\rangle$ manifold. For the moment, though, we assume the simplified level diagram shown in Fig. 3.5. Here Raman beam 1 drives only the $|1\rangle \leftrightarrow$ P transition and Raman beam 2 drives only the $|2\rangle \leftrightarrow$ P transition, with ω_0 for the $|1\rangle \leftrightarrow$ P transition frequency and ω_{12} for the $|1\rangle \leftrightarrow |2\rangle$

transition frequency. Then we have $\mathbf{\Omega}_j = \Omega_j|\mathrm{P}\rangle\langle j| + \mathrm{h.c.}$ with $\Omega_j \equiv \langle j|\mathbf{\Omega}_j|\mathrm{P}\rangle$, $j = 1, 2$. The full Hamiltonian, including the energies of the atomic states, is then

$$\mathbf{H} = -\omega_0|1\rangle\langle 1| - (\omega_0 - \omega_{12})|2\rangle\langle 2| + \sum_{j=1,2} \Omega_j \left(e^{i\boldsymbol{\varphi}_j^L} e^{-i\omega_j t} + \mathrm{c.c.}\right)(|\mathrm{P}\rangle\langle j| + \mathrm{h.c.}) \tag{3.5}$$

where the operator $\boldsymbol{\varphi}_j^L \equiv \vec{k}_j \cdot \vec{\mathbf{x}} + \varphi_j$ acts on the ion motional state only.

To get rid of the fast rotation of the interaction term in the Hamiltonian (3.5), we transform to an interaction picture with respect to the free Hamiltonian $-\sum_{j=1,2} \omega_j|j\rangle\langle j|$ and make the rotating-wave approximation [36] to remove terms varying at optical frequencies. We define $\Delta_1 = \omega_1 - \omega_0$, $\Delta_2 = \omega_2 - (\omega_0 - \omega_{12})$ the laser detunings. The Hamiltonian then becomes

$$\mathbf{H}_I = \sum_{j=1,2} \Delta_j\ |j\rangle\langle j| + \sum_{j=1,2} \Omega_j\ [\mathbf{V}_j + \mathrm{h.c.}] \tag{3.6}$$

where we define the transition operators $\mathbf{V}_j = e^{i\boldsymbol{\varphi}_j^L}|\mathrm{P}\rangle\langle j|$. In the experimental situation, we have $|\Omega_j/\Delta_j| \ll 1$, so we can use the method of small rotations [37] to derive an effective Hamiltonian on the $|1\rangle$, $|2\rangle$ subspace. This method is equivalent to adiabatically eliminating $|\mathrm{P}\rangle$ [2, 28], but reveals the physics of the Raman process more clearly. We define the unitary transformation

$$\mathbf{U}_{\mathrm{small}} = \exp\left[-\sum_{j=1,2} \frac{\Omega_j}{\Delta_j}(\mathbf{V}_j - \mathrm{h.c.})\right] \tag{3.7}$$

which constitutes a small nonlinear rotation of the Hamiltonian (3.6). Then to lowest order in the $|\Omega_j/\Delta_j|$, we have the effective Hamiltonian $\mathbf{H}' = \mathbf{U}_{\mathrm{small}}\mathbf{H}_I\mathbf{U}_{\mathrm{small}}^\dagger$ given by

$$\mathbf{H}' = \sum_{j=1,2} \left(\Delta_j + \frac{2\Omega_j^2}{\Delta_j}\right)|j\rangle\langle j| - \sum_{j=1,2} \frac{2\Omega_j^2}{\Delta_j}|\mathrm{P}\rangle\langle\mathrm{P}| + \Omega_1\Omega_2\left(\frac{1}{\Delta_1} + \frac{1}{\Delta_2}\right)[\mathbf{V}_R + \mathrm{h.c.}] \tag{3.8}$$

where we define the Raman transition operator

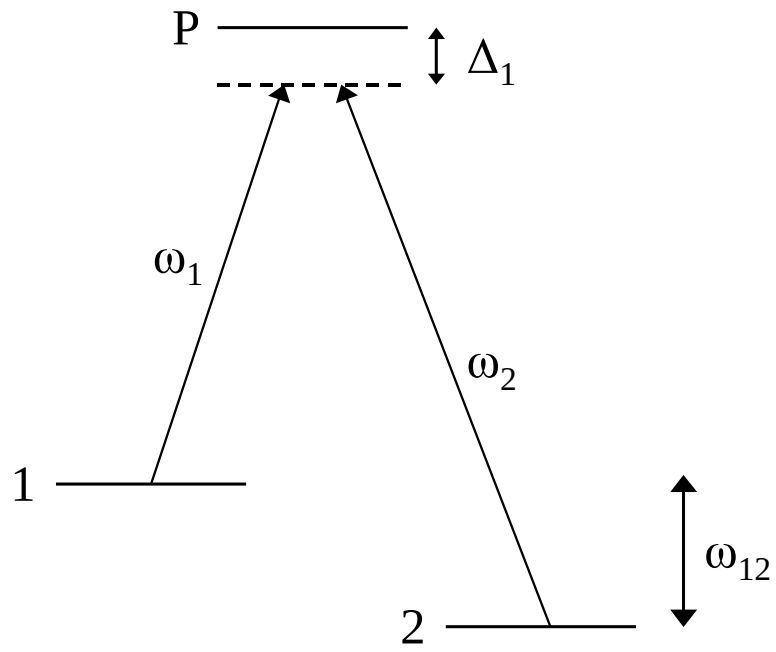

Figure 3.5: Level diagram for our simplified model of stimulated Raman transitions. Raman beam 1 couples $|1\rangle$ to P, while beam 2 couples $|2\rangle$ to P.

$$\mathbf{V}_R \equiv -e^{i\boldsymbol{\varphi}^L}|2\rangle\langle 1| \tag{3.9}$$

$$\boldsymbol{\varphi}^L \equiv \boldsymbol{\varphi}_1^L(\vec{x}) - \boldsymbol{\varphi}_2^L(\vec{x}) \tag{3.10}$$

The operator $\boldsymbol{\varphi}^L$ encodes the information about the spatial interference pattern of the Raman beams: $\boldsymbol{\varphi}^L = \exp[i(\vec{\Delta k}\cdot\vec{\mathbf{x}}+\varphi_R)]$, where $\vec{\Delta k} = \vec{k}_1 - \vec{k}_2$ and $\varphi_R = \varphi_1 - \varphi_2$. From Eqs. 3.8 and 3.10 we see that the motional dynamics depend only on $\vec{\Delta k}$. The apparently insignificant quantity φ_R is one of the most important parameters in our experiments, as we will see in Section 6.

Since the amplitude in $|\mathrm{P}\rangle$ is always small for Δ much greater than the linewidth, we neglect the term proportional to $|\mathrm{P}\rangle\langle\mathrm{P}|$ in Eq. (3.8). The Hamiltonian (3.8) then involves only the states $|1\rangle$ and $|2\rangle$; the state P has finally been eliminated. We define the single-photon detuning $\Delta \equiv (\Delta_1 + \Delta_2)/2$, the detuning from two-photon resonance $\delta \equiv \Delta_1 - \Delta_2 = (\omega_1 - \omega_2) - \omega_{12}$, and the Raman Rabi frequency $\Omega_R \equiv 2\Omega_1\Omega_2/\Delta$. The term in Ω_j^2/Δ_j describes the AC Stark shift of the $|j\rangle$ level due to the presence of the Raman light. The detuning from the Stark-shifted two-photon resonance is then $\delta' \equiv \delta + 2(\Omega_1^2 - \Omega_2^2)/\Delta$. We write angular-momentum operators for the effective spin-1/2 system $|1\rangle$, $|2\rangle$ as

$$\mathbf{S}_z \equiv (|2\rangle\langle 2| - |1\rangle\langle 1|)/2 \qquad \mathbf{S}_+ \equiv |2\rangle\langle 1| \qquad \mathbf{S}_- \equiv |1\rangle\langle 2| \tag{3.11}$$

with the commutation relations

$$[\mathbf{S}_+, \mathbf{S}_-] = 2\mathbf{S}_z \qquad [\mathbf{S}_z, \mathbf{S}_\pm] = \pm\mathbf{S}_\pm \tag{3.12}$$

The z-axis used for internal states is the quantization axis, NOT the trap axis $\hat{z}$ of Figure 2.4! We can recover the vector form of the spin operator $\vec{\mathbf{S}}$ with the definitions $\mathbf{S}_\pm \equiv \mathbf{S}_x \pm i\mathbf{S}_y$. With these modifications and definitions, the Hamiltonian (3.8) becomes

$$\mathbf{H}' = -\delta'\mathbf{S}_z + \Omega_R\left[e^{i\varphi_R}e^{i\vec{\Delta k}\cdot\mathbf{x}}\mathbf{S}_+ + \text{h.c.}\right] \tag{3.13}$$

where we have redefined the zero of energy. Transforming Eq. (3.13) to an interaction picture with respect to the free Hamiltonian $-\delta'\mathbf{S}_z$ gives the standard form of the Raman Hamiltonian [2]

$$\mathbf{H}_R = \Omega_R e^{i\varphi_R}e^{i\vec{\Delta k}\cdot\mathbf{x}}e^{-i\delta' t}\mathbf{S}_+ + \text{h.c.} \tag{3.14}$$

In the case $\vec{\Delta k} \approx 0$ (copropagating Raman beams), the Hamiltonian (3.14) reduces to

$$\mathbf{H}_{\text{co}} \approx \Omega_R e^{i\varphi_R}e^{-i\delta' t}\mathbf{S}_+ + \text{h.c.} \tag{3.15}$$

which is completely independent of the ion motion. Assuming that the Raman beams are two-photon resonant with the $|1\rangle \leftrightarrow |2\rangle$ transition ($\delta' = 0$), the Hamiltonian (3.15) describes Rabi flopping between $|1\rangle$ and $|2\rangle$ according to

$$\begin{pmatrix} C_2(t) \\ C_1(t) \end{pmatrix} = \begin{pmatrix} \cos\Omega t & -ie^{i\varphi_R}\sin\Omega t \\ -ie^{-i\varphi_R}\sin\Omega t & \cos\Omega t \end{pmatrix}\begin{pmatrix} C_2(0) \\ C_1(0) \end{pmatrix} \tag{3.16}$$

where the atomic wavefunction $\Psi = C_1(t)|1\rangle + C_2(t)|2\rangle$. We use this "copropagating carrier" evolution mainly as a diagnostic tool in the experiment, since it enables us to prepare arbitrary single-ion qubit states in a way that does not depend on the ion motional state.

3.3.2 Coupling to the Ion Motion

We performed almost all our quantum logic operations using Raman beams with an angular separation of 90° and with $\vec{\Delta k}$ parallel to the trap axis $\hat{z}$. As we will see, this geometry allows us to drive Raman transitions involving both the internal and motional states of the ions. Since ω_{12} is small compared to the $|\text{S}\rangle \leftrightarrow |\text{P}\rangle$ transition frequency, we have $k \equiv |\vec{k}_1| \approx |\vec{k}_2|$. Now

the dynamics depends on the motion of the ions along the trap axis, so the full Hamiltonian includes the energy of axial motion. For one ion we find

$$\mathbf{H} = \omega_z \mathbf{a}^\dagger \mathbf{a} + \Omega_R \left[e^{i\varphi_R} e^{i\sqrt{2}kz} e^{-i\delta' t} \mathbf{S}_+ + \text{h.c.} \right] \tag{3.17}$$

where $\mathbf{a}$ is the annihilation operator for the quantized motion along $\hat{z}$. The Hamiltonian (3.17) depends only on the motion along $\hat{z}$. This fact simplifies the dynamics enormously: for N ions we need only consider the N axial normal modes rather than the full set of $3N$ motional modes (see Sec. 2.1.3.) We can probe all $3N$ motional modes by applying counterpropagating Raman beams along an axis skew to all three trap axes.

We continue to consider only one ion. Transforming to an interaction picture with respect to the free Hamiltonian $\omega_z \mathbf{a}^\dagger \mathbf{a}$, we find

$$\begin{aligned} \mathbf{H}_z &= \Omega_R \mathbf{S}_+ e^{i\varphi_R} \exp\left[i\eta \left(\mathbf{a}^\dagger e^{i\omega_z t} + \mathbf{a} e^{-i\omega_z t} \right) - i\delta' t \right] + \text{h.c.} \\ &= \Omega_R \mathbf{S}_+ e^{i\varphi_R} \sum_{m=0}^{\infty} \frac{(i\eta)^m}{m\,!} \left(\mathbf{a}^\dagger e^{i\omega_z t} + \mathbf{a} e^{-i\omega_z t} \right)^m e^{-i\delta' t} + \text{h.c.} \end{aligned} \tag{3.18}$$

Here we have defined the Lamb-Dicke parameter $\eta \equiv \sqrt{2}kz_0$, with $z_0 = (2m_{\text{ion}}\omega_z)^{-1/2}$ the zero-point wavepacket spread along $\hat{z}$. The condition $k^2\langle \mathbf{z}^2 \rangle \ll 1$, for which the ion wavepacket is much smaller than the wavelength of the Raman beam interference pattern, is called the Lamb-Dicke limit. For each power of $\mathbf{a}$ we retain only the lowest-order term in η, giving

$$\mathbf{H}_z = \Omega_R \mathbf{S}_+ e^{i\varphi_R} e^{-i\delta' t} \sum_{m=0}^{\infty} \frac{(i\eta)^m}{m\,!} [(\mathbf{a}^\dagger)^m e^{im\omega_z t} + \mathbf{a}^m e^{-im\omega_z t}] + \text{h.c.} \tag{3.19}$$

The Hamiltonian (3.19) exhibits a series of resonances at the two-photon detunings $\delta' \approx m\omega_z$. In the Lamb-Dicke limit, the series expansion in Eq. (3.19) converges rapidly. For a particular value of m, the dynamics on resonance then obeys the approximate Hamiltonian

$$\mathbf{H}_m = \Omega_R e^{i\varphi_R} \frac{(i\eta)^{|m|}}{|m|!} \mathbf{S}_+ (\mathbf{a}^\dagger)^m + \text{h.c.} \tag{3.20}$$

where as usual $(\mathbf{a}^\dagger)^{-1} = \mathbf{a}$. This Hamiltonian is similar to the copropagating carrier Hamiltonian (3.15), except that it changes the motional state of the ion. Writing the ion internal/motional wavefunction as $\Psi = \sum_{n=0}^{\infty} C_{1,n}|1,n\rangle + \sum_{n=0}^{\infty} C_{2,n}|2,n\rangle$, we see that while the Hamiltonian (3.15) couples $|1,n\rangle$ to $|2,n\rangle$, the new Hamiltonian $\mathbf{H}_m$ couples $|1,n\rangle$ to $|1,n+m\rangle$. The ion then undergoes Rabi flopping with

$$\begin{pmatrix} C_{2,n+m}(t) \\ C_{1,n}(t) \end{pmatrix} = \begin{pmatrix} \cos\Omega_{n+m,n}t & i^{|m|-1}e^{i\varphi_R}\sin\Omega_{n+m,n}t \\ i^{|m|-1}e^{i\varphi_R}\sin\Omega_{n+m,n}t & \cos\Omega_{n+m,n}t \end{pmatrix} \begin{pmatrix} C_{2,n+m}(0) \\ C_{1,n}(0) \end{pmatrix} \tag{3.21}$$

$$\Omega_{n+m,n} \equiv \Omega_R e^{-\eta^2/2} \frac{\eta^{|m|}}{|m|!} \frac{(n_<)!}{(n_>)!}^{1/2} \tag{3.22}$$

where $n_>$ is the greater of n, $n+m$. The cases of particular interest for our experiments are $m = 0$ (the "carrier"), $m = -1$ (the "red sideband"), and $m = +1$ (the "blue sideband".) For instance, if the ion starts in the ground state $|\downarrow,0\rangle$ and we apply Raman light resonant with the blue sideband transition, it will coherently evolve through a superposition state $|\downarrow,0\rangle + |\uparrow,1\rangle$ to the state $|\uparrow,1\rangle$.[1] The intermediate superposition state exhibits entanglement between the spin and the motion (see Section 5), enabling transfer of quantum information from the spin of one ion, through a normal mode of motion involving the whole ion crystal, and back into the spin of another ion [38]. Thus we can use a motional mode of the ion crystal as a "quantum data bus," creating an effective interaction between ion spins on demand, even though the ion spins do not directly interact. The multi-bit logic operations engineered in this way are at the heart of the quantum computing results presented in this thesis.

[1] Here and hereafter, we suppress wavefunction normalization factors unless they are relevant to the point under discussion.

3.3.3 Raman Transitions with Multiple Ions

In the case of N ions, we must consider the coupling to all N axial modes to find the dynamics under the Raman drive. Instead of Eq. (3.17), we now have the Hamiltonian

$$\mathbf{H} = \sum_{k=1}^{N} \xi_k \omega_z \mathbf{a}_k^\dagger \mathbf{a}_k + \sum_{j=1}^{N} \Omega_R \left[e^{i\phi_j} e^{i\sqrt{2}kz_j} e^{-i\delta' t} \mathbf{S}_{j,+} + \text{h.c.} \right] \tag{3.23}$$

where ions are indexed by j, normal modes by k. The $\mathbf{a}_k$ are the normal mode annihilation operators defined by Eq. (2.31) and ϕ_j is the relative phase of the Raman beams φ_R at ion j. Defining $\eta_k^j \equiv v_k^{(j)} \eta / \sqrt{\xi_k}$ the Lamb-Dicke parameter of the jth ion in the kth mode and assuming the Lamb-Dicke limit, we find the analog of Eq. (3.19)

$$\mathbf{H}_z = \Omega_R e^{-i\delta' t} \sum_{j=1}^{N} \mathbf{S}_{j,+} e^{i\phi_j} \sum_{k=1}^{N} \sum_{m=0}^{\infty} \frac{(i\eta_k^j)^m}{m\,!} [(\mathbf{a}^\dagger)^m e^{im\xi_k \omega_z t} + \mathbf{a}^m e^{-im\xi_k \omega_z t}] + \text{h.c.} \tag{3.24}$$

which again exhibits resonances, this time at $\delta' \approx m\xi_k \omega_z$ for coupling to the kth normal mode.

We define the total angular momentum of the ion crystal in the usual way as

$$\vec{\mathbf{J}} = \sum_{j=1}^{N} \vec{\mathbf{S}} \tag{3.25}$$

Then the carrier Hamiltonian ($m = 0$) becomes simply

$$\mathbf{H}_0 = \Omega_R e^{-i\delta' t} \mathbf{J}_+ + \text{h.c.} \tag{3.26}$$

Here we have taken the phases $\phi_j = 0$. We can take $\phi_j \neq 0$ by making the replacement $\mathbf{S}_{j,+} \to e^{i\phi_j} \mathbf{S}_{j,+}$ in the following.

In our experiments the modes were always well-resolved from each other, so near the mth sideband of the kth mode we find the Hamiltonian

$$\mathbf{H}_{m,k} = \Omega_R \sum_{j=1}^{N} \frac{(i\eta_k^j)^{|m|}}{|m|!} \mathbf{S}_{j,+} (\mathbf{a}^\dagger)^m + \text{h.c.} \tag{3.27}$$

similar to Eq. (3.20). For the mode used for the entangling gate (see Sec. 5), we require $v_k^{(j)}$ independent of j. In this case the η_k^j are independent of j and we simply write $\eta_k = \eta/\sqrt{N\xi_k}$. The Hamiltonian then takes the simple form

$$\mathbf{H}_{m,k} = \Omega_R \frac{(i\eta_k)^{|m|}}{|m|!} \mathbf{J}_{j,+} (\mathbf{a}^\dagger)^m + \text{h.c.} \tag{3.28}$$

3.3.4 Cooling to the Ground State

At the end of each shot of an experiment, we apply BD for several hundred μs, cooling the ions to the Doppler limit (about 10 MHz of energy). Usually, though, we use resolved-sideband Raman cooling [39, 40, 41] to cool the ions still further. For clarity, we first consider Raman cooling on a single motional mode of a single ion. Suppose the ion is initially in $|\downarrow; n = 1\rangle$. Driving on the red sideband for a time $t = \pi/\Omega_{1,0}$ produces $|\uparrow; n = 0\rangle$. Then, optically pumping to the state $|\downarrow; n = 0\rangle$, we see that the motional mode has been cooled by one phonon[41]. Because the ion is in the Lamb-Dicke limit, the optical pumping is nearly recoilless and is unlikely to heat the ion [42, 43].

In practice, the ion starts in a thermal state, so the distribution of phonon number states is broad. Assuming a small probability of occupying states with more than K phonons, we can cool the whole distribution to the ground state by applying K cycles of Raman drive and optical pumping. Here we specify the pth Raman pulse duration as $t_p = \pi/\Omega_{K-(p-1),K-p}$, so that the first Raman pulse transfers all the population in $|K\rangle$ to $|K-1\rangle$, the second pulse transfers $|K-1\rangle$ to $|K-2\rangle$, etc. In this way the population is sequentially transferred to the ground state. The Visual C++ program controlling the experiment (see Sec. 4.6) computed the pulse durations using the inputs Ω_R, the mode frequency, and the number of pulses desired. The

Raman and optical pumping pulses typically lasted a few μs each. The final temperature of the mode was approximately equal to the mode heating rate (see Sec. 7.4) times the duration of a cooling cycle.

We could not use BD in repumping the ion to $|\downarrow\rangle$. While photon scattering is nearly recoilless in the Lamb-Dicke limit, the hundreds or thousands of photons scattered on the cycling transition would certainly cause the ion to equilibrate to the Doppler cooling limit [39]. Rather, we must optically pump to $|\downarrow\rangle$ while scattering only a few photons. Scattering a few RD photons ensures that the ion resides in the $^2\mathrm{S}_{1/2}\,|F=2\rangle$ manifold, but does not select the $m_F=-2$ magnetic state. To pump to $m_F=-2$, we apply RD and the blue optical pumping (BOP) beam simultaneously. BOP is polarized σ^- in the atomic basis and is tuned to the $^2\mathrm{S}_{1/2}\,|F=2\rangle \leftrightarrow {}^2\mathrm{P}_{1/2}\,|F=2\rangle$ transition. (BD is instead tuned to the $^2\mathrm{P}_{3/2}$ transition.) Dipole selection rules then keep $|\downarrow\rangle$ dark to BOP, while all other $^2\mathrm{S}_{1/2}\,|F=2\rangle$ transitions are bright to BOP. Hence the cycling transition is never excited by BOP and the ion only scatters a few photons before arriving at the dark $|\downarrow\rangle$ state. The few photons scattered from BOP and RD cause almost no heating of the ion during the optical pumping step.

To cool multiple motional modes of an ion crystal, we applied several Raman cooling cycles to each mode in succession. In this case, however, it was quite difficult to find the pulse durations corresponding to the procedure above, since we were coupling a single motional mode to several spins simultaneously. Experimental data and a theoretical treatment for the two-ion case can be found in [44]. In practice, we found that fudging the input parameters to the Visual C++ program (see Sec. 4.6) and using the resulting one-ion pulse durations produced cooling nearly as good as that given by the orthodox procedure. We could cool the stretch modes to the ground state almost perfectly because of their low heating rate (see Sec. 7.4), but usually about

one phonon remained in the COM mode. The precise cooling limit depended on the number of ions and the trap frequency.

As an alternative to the "pulsed" cooling scheme described above, we tried a "continuous" Raman cooling scheme in which we applied the red sideband drive and the optical pumping light simultaneously. If the relative intensities of Raman and optical pumping light were correctly adjusted, the average phonon number in the mode being cooled decreased exponentially with time [39, 45]. In this scheme, one does not need to compute the lengths of cooling pulses, avoiding considerable headache. The final temperature from continuous cooling was about the same as that for the pulsed cooling scheme with fudged pulse durations, but continuous cooling was about a factor of two slower.

3.3.5 Raman Transitions in $^9Be^+$

The three-level model of Raman transitions presented in Sec. 3.3.1 describes the essential features of coherent coupling through two-photon processes. However, real atoms possess a great deal more than three levels, and the effect of these other levels plays a crucial role in the engineering of robust quantum logic gates. In the experiments described here, the wavelength of the Raman light was usually set to 626.341 nm, for reasons described in Sections 7.2.2 and 7.3. Since the wavelength of the $^2S_{1/2} \leftrightarrow {}^2P_{1/2}$ transition is 626.395 nm and that of the $^2S_{1/2} \leftrightarrow {}^2P_{3/2}$ transition is 626.266 nm, both the $^2P_{1/2}$ and $^2P_{3/2}$ states participate in the Raman process. At the same time, the polarizations of the Raman beams affect the two-photon processes through the hyperfine and magnetic structure of the $^2P_{1/2}$ and $^2P_{3/2}$ levels.

To understand Raman transitions in the context of the real $^9Be^+$ ion, we return to the expression (3.3) for the dipole interaction Hamiltonian. For clarity, we consider only one ion. We index the hyperfine levels of the $^2P_{1/2}$ manifold by the label $\mathcal{F}_{1/2}$ and write $|\mathcal{F}_{1/2}\rangle \equiv {}^2P_{1/2}\,|F, m_F\rangle$. Similarly, $\mathcal{F}_{3/2}$ indexes the $^2P_{3/2}$ manifold and $\mathcal{F}_P$ runs over all indexes $\{\mathcal{F}_{1/2}, \mathcal{F}_{3/2}\}$. We decompose the laser polarization in the atomic basis $\hat{\epsilon}_a \in \{\sigma^+, \sigma^-, \pi\}$ defined by the quantization field and write

$$\Omega_j = -\frac{E_j}{2}\langle {}^2S_{1/2}\,, F = 2, m_F = -2|\sigma^- \cdot \vec{\boldsymbol{\mu}}|{}^2P_{3/2}\,, F = 3, m_F = -3\rangle \tag{3.29}$$

$$S(j, \mathcal{F}_P; \hat{\epsilon}_a) = \frac{\langle j|\hat{\epsilon}_a \cdot \vec{\boldsymbol{\mu}}|\mathcal{F}_P\rangle}{\Omega_j} \tag{3.30}$$

so that a laser of amplitude E_j and polarization $\hat{\epsilon}_a$ induces a Rabi frequency of $S(j, \mathcal{F}_P; \hat{\epsilon}_a)\Omega_j$ on the $|j\rangle \leftrightarrow \mathcal{F}_P$ transition.[2] Since only one laser polarization (in the atomic basis) can drive a given $|j\rangle \leftrightarrow \mathcal{F}_P$ transition, there is only one choice of $\hat{\epsilon}_a$ for which $S(j, \mathcal{F}_P; \hat{\epsilon}_a) \neq 0$; however, it is notationally convenient to retain the index $\hat{\epsilon}_a$. The S-factors (3.30) are tabulated in Appendix B of [28]. We choose a convention in which Ω_j and S are real, and as usual $\hbar = 1$. Fixing the zero of energy at the energy of the $^2P_{1/2}$ level, writing the fine-structure splitting $\omega_{FS} = 2\pi \times 197$ GHz, and neglecting the hyperfine splittings of the P levels, we find the full Hamiltonian in Schrödinger picture

$$\begin{aligned}\mathbf{H} = &-\omega_0|1\rangle\langle 1| - (\omega_0 - \omega_{\downarrow\uparrow})|2\rangle\langle 2| + \omega_{FS}\sum_{\mathcal{F}_{3/2}} |\mathcal{F}_{3/2}\rangle\langle\mathcal{F}_{3/2}| \\ &+ \sum_{j=1,2}\sum_{\mathcal{F}_P, \hat{\epsilon}_a} \Omega_j\, S(j, \mathcal{F}_P; \hat{\epsilon}_a)\left[(\hat{\epsilon}_a^* \cdot \hat{\epsilon}_j)e^{i\boldsymbol{\phi}_j^L} e^{-i\omega_1 t} + \text{c.c.}\right)(|\mathcal{F}_P\rangle\langle 1| + \text{h.c.}]\end{aligned} \tag{3.31}$$

for $|1\rangle$, $|2\rangle$ in the $^2S_{1/2}$ manifold. In the experiment, we always ensure that the transition frequencies between the various $^2S_{1/2}$ hyperfine states are well-resolved, so that we need only consider two $^2S_{1/2}$ sublevels in Eq. (3.31).

[2] Recall that the $^2S_{1/2} \leftrightarrow {}^2P_{1/2}$ and $^2S_{1/2} \leftrightarrow {}^2P_{3/2}$ linewidths are equal.

Now going to an interaction picture with respect to the laser frequencies and making the rotating-wave approximation to remove terms varying at optical frequencies, we find the generalization of Eq. (3.6)

$$\mathbf{H}_I = \sum_{j=1,2} \Delta_j \, |j\rangle\langle j| + \omega_{\rm FS} \sum_{\mathcal{F}_{3/2}} |\mathcal{F}_{3/2}\rangle\langle\mathcal{F}_{3/2}| + \sum_{j=1,2} \sum_{\mathcal{F}_{\rm P},\hat{\epsilon}_a} \Omega_j \; S(j,\mathcal{F}_{\rm P};\hat{\epsilon}_a) \left((\hat{\epsilon}_a^* \cdot \hat{\epsilon}_j)\mathbf{V}_{j,\mathcal{F}_{\rm P}} + \text{h.c.}\right) \tag{3.32}$$

where $\mathbf{V}_{j,\mathcal{F}_{\rm P}} = e^{i\boldsymbol{\varphi}_j^L} |\mathcal{F}_{\rm P}\rangle\langle j|$. We again apply the method of small rotations [37], defining the unitary transformation

$$\mathbf{U}_{\rm small} = \exp\left\{ - \sum_{j=1,2} \sum_{\mathcal{F}_{\rm P},\hat{\epsilon}_a} \frac{\Omega_j S(j,\mathcal{F}_{\rm P};\hat{\epsilon}_a)}{\Delta_{j,k}} \left[(\hat{\epsilon}_a^* \cdot \hat{\epsilon}_j)\mathbf{V}_{j,\mathcal{F}_{\rm P}} - \text{h.c.}\right] \right\} \tag{3.33}$$

$$\Delta_{j,k} \equiv \begin{cases} \Delta_j & k = 1/2 \\ \Delta_j - \omega_{\rm FS} & k = 3/2 \end{cases} \tag{3.34}$$

Transforming $\mathbf{H}_I \to \mathbf{H}' = \mathbf{U}_{\rm small}\mathbf{H}_I\mathbf{U}_{\rm small}^\dagger$ and again neglecting terms in $|\mathcal{F}_{\rm P}\rangle\langle\mathcal{F}_{\rm P}|$, we find the effective Hamiltonian

$$\mathbf{H}' = \sum_{j=1,2} \left(\Delta_j + 2\Omega_j^2 \sum_{k=\{1/2,3/2\}} \frac{R^{(k)}_{{\rm Stark},j}}{\Delta_k} |j\rangle\langle j| + \Omega_R R_{\rm Raman} \frac{\omega_{\rm FS}}{\omega_{\rm FS} - \Delta} \left[\mathbf{V}_R + \text{h.c.}\right] \right) \tag{3.35}$$

$$R^{(k)}_{{\rm Stark},j} \equiv \sum_{\mathcal{F}_k,\hat{\epsilon}_a} \left(S(j,\mathcal{F}_k;\hat{\epsilon}_a)\right)^2 |\hat{\epsilon}_a^* \cdot \hat{\epsilon}_j|^2 \tag{3.36}$$

$$R_{\rm Raman} \equiv \sum_{\mathcal{F}_{1/2},\hat{\epsilon}_a,\hat{\epsilon}'_a} S(1,\mathcal{F}_{1/2};\hat{\epsilon}_a) S(2,\mathcal{F}_{1/2};\hat{\epsilon}'_a)(\hat{\epsilon}_a^* \cdot \hat{\epsilon}_1)(\hat{\epsilon}_{a'}^* \cdot \hat{\epsilon}_2) \tag{3.37}$$

$$\frac{1}{\Delta_k} \equiv \frac{1}{\Delta_{1,k}} \approx \frac{1}{\Delta_{2,k}} \tag{3.38}$$

One can readily verify that $R_{\rm Raman}$ is invariant under the replacement $\mathcal{F}_{1/2} \to \mathcal{F}_{3/2}$, though the individual factors $S(j,\mathcal{F}_{\rm P};\hat{\epsilon}_a)$ are not. The detuning from the Stark-shifted two-photon resonance becomes

$$\delta_{12} = \delta + \sum_{k=\{1/2,3/2\}} \left(\frac{2\Omega_1^2 R_{\mathrm{Stark},1}^{(k)}}{\Delta_k} - \frac{2\Omega_2^2 R_{\mathrm{Stark},2}^{(k)}}{\Delta_k} \right) \tag{3.39}$$

and the Rabi frequency of $|1\rangle \leftrightarrow |2\rangle$ transitions becomes

$$\Omega_{12} = \Omega_R R_{\mathrm{Raman}} \frac{\omega_{\mathrm{FS}}}{\omega_{\mathrm{FS}} - \Delta} \tag{3.40}$$

$$= \Omega_1 \Omega_2 R_{\mathrm{Raman}} \frac{\omega_{\mathrm{FS}}}{\Delta(\omega_{\mathrm{FS}} - \Delta)} \tag{3.41}$$

After some manipulation, the Hamiltonian assumes the form

$$\mathbf{H}_{12} = \Omega_{12} e^{i\varphi_R} e^{i\vec{\Delta k}\cdot\mathbf{x}} e^{-i\delta_{12}t} \mathbf{S}_+ + \mathrm{h.c.} \tag{3.42}$$

identical to the form of the effective Hamiltonian (3.14) derived for the simpler three-level system in Sec. 3.3.1. The results following from Eq. (3.14) in Secs. 3.3.1 and 3.3.2 then hold if we make the replacements $\Omega_R \to \Omega_{12}$, $\delta' \to \delta_{12}$.

Chapter 4

Laser Apparatus and Experiment Control

4.1 Laser Sources at 626 nm

We generated the 313 nm light used in these experiments by resonantly doubling 626 nm light from stabilized dye lasers. We needed to access the $^2S_{1/2} \leftrightarrow {}^2P_{1/2}$ transition at 313.197 nm and the $^2S_{1/2} \leftrightarrow {}^2P_{3/2}$ transition at 313.133 nm, and we also needed off-resonant light at 313.170 nm to generate the Raman beams. These wavelengths are separated by hundreds of GHz, so accessing multiple wavelengths by modulation from a single laser was not possible. Therefore we used three dye laser sources operating at 626.395 nm, 626.266 nm, and 626.341 nm and resonantly doubled these laser beams separately to produce the desired UV wavelengths.

The detection laser (626.266 nm) and the Raman laser (626.341 nm) were home-built to a design by Jim Bergquist, our resident laser expert (Fig. 4.1). The laser at 626.395 nm was a Coherent model 699. All three lasers used Kiton Red dye, manufactured by Exciton. Typically 1.5 g of dye was dissolved in $\sim$ 1 L of ethylene glycol. The dye solution was drawn from a reservoir and forced through a laminar flow nozzle under an input pressure $\sim$ 2.75 bar to form a jet 100 μm thick. This jet provided the laser gain when optically excited by a pump laser. The dye jet traveled about 5 mm from the nozzle before intersecting the pump beam, and was oriented at Brewster's angle for the 626 nm light. To obtain good laser power and linewidth, it

Figure 4.1: Jim says, "I love the smell of laser dye in the morning..."

was necessary that the dye jet travel 20 cm past the gain region before striking the catch tube that returned the dye to the reservoir; otherwise acoustic noise generated at the striking point traveled back to the gain region, degrading the laser performance. The pump for the Raman laser was a Coherent Verdi V-5 doubled Nd:YAG laser operating at 532 nm with 5.5 W output power, yielding $\sim$ 1 W of 626 nm light from the Raman laser. The pump for the detection laser and the 699 was a Spectra-Physics Model 2030 argon-ion laser operating at 514 nm with typically 14–16 W output power. The argon laser light was split two ways to provide 7–8 W to each dye laser, yielding 600 mW at 626 nm from the detection laser and 300 mW from the 699. The dye laser powers quoted are for fresh dye. Over time, the dye ages and its gain decreases. Typically we replaced the dye solution when the laser power dropped to about 2/3 its maximum value. All three lasers were S-polarized (electric field perpendicular to the optical table.)

The optical design for the homemade lasers is shown in Fig. 4.2. The optical design for the 699 can be found in [46]. Each laser also had several intracavity elements: an optical diode to ensure unidirectional operation, a three-plate birefringent filter, a thin etalon, and a thick

etalon. The frequency-dependent transmission of the last three elements modulated the cavity loss at free spectral ranges (FSRs) of 1.9 THz, 200 GHz, and 10 GHz respectively. When the transmission maxima of the three elements overlapped at a particular frequency, gain competition ensured single-mode operation of the laser [47]. The birefringent filter was manually tuned with a micrometer. The thin etalon consisted of an optically flat glass plate ~ 0.5 mm thick, mounted to a galvo motor. We tuned the thin etalon by adjusting the current to the galvo. The thick etalon was similar to that found in the 699 [46] and was tuned by adjusting the voltage to a piezoelectric transducer (PZT) mounted in the thick etalon assembly. The 699 also included an intracavity Brewster plate to extend the range over which the laser could be tuned without mode-hops [46]. The thick etalon of each laser was locked to the point of maximum laser power by modulating the thick etalon voltage at 30 kHz and feeding back the demodulated laser intensity signal to the average thick etalon voltage. The feedback was provided by an integrating gain stage with bandwidth 1 kHz. This lock maximized the thick etalon transmission at the frequency of the lasing mode. The three tuning elements allowed us to tune each laser to within a few hundred MHz of any desired frequency. We could scan each laser about 1 GHz without mode-hops.

The homemade lasers were frequency-stabilized to a linewidth of $\lesssim 500$ kHz using feedback to the 30 cm mirror, which was mounted on a PZT. The bandwidth of the servo was limited by the mechanical resonance frequency of the PZT, which was 10 kHz for the detection laser and 20 kHz for the Raman laser. The error signal was derived by the Hänsch-Couillaud method [48] using a 20 cm confocal reference cavity in each case. The reference cavities were made by contacting mirrors to the ends of an Invar tube and were enclosed in insulating boxes to minimize thermal drift of the cavity length. One mirror of each cavity was mounted on a PZT for external adjustment of the cavity resonance. The servos used for locking had proportional and integral gain, as well as a second stage of integration. Usually we used only the two integration

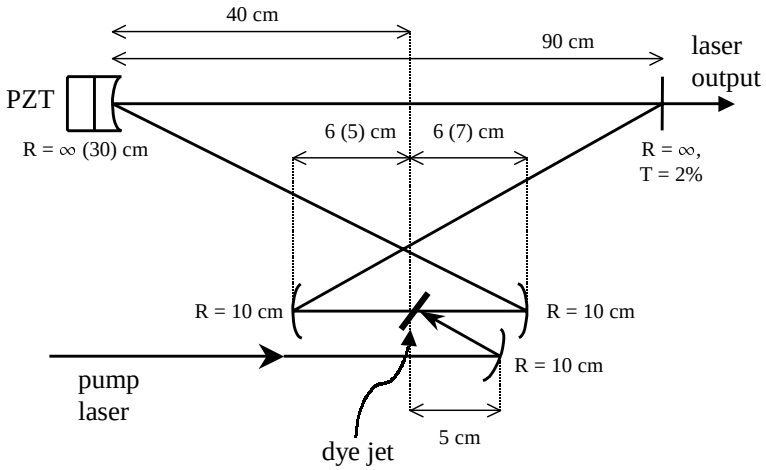

Figure 4.2: Optical design of a homemade laser. Intracavity optical elements are not shown. Values refer to the Raman (detection) laser. R = radius of curvature, T = transmission, PZT = piezoelectric transducer. Drawing is not to scale.

stages. The corner frequencies and overall gain were routinely adjusted to give the best noise reduction. The 699 was frequency-stabilized to a linewidth of about 10 MHz by sidelock to a reference cavity [46].

Our experiments were insensitive to slow drifts of the Raman laser frequency, as these drifts amounted to less than hundreds of MHz over a day, much less than the Raman laser detuning of tens of GHz. Thus it was not necessary to stabilize the Raman laser in absolute frequency. However, similar drifts of the absolute frequencies of the 699 and detection lasers would seriously affect our experiments, since we needed the doubled light from these lasers to be nearly resonant with atomic transitions of linewidth 20 MHz. We therefore used saturated-absorption iodine spectroscopy [49] to stabilize the 699 and detection lasers relative to iodine lines. We fed back the resulting error signals to the reference cavity PZTs using integrating servos with bandwidths of 10–100 Hz.

The beams used for iodine spectroscopy were derived from the main laser beams using acousto-optic modulators (AOMs), allowing us to offset the laser frequency from the frequency of the iodine line by up to $\sim$ 1 GHz. For each laser, we were able to identify an iodine line whose offset from the desired laser wavelength was within this range. We used line #954 of the "Iodine Atlas" [50] to lock the 699 and line #961 to lock the detection laser. Our lock-in detection technique produced a series of dispersive error signals, one for each component of the iodine line. We locked each laser to the bluemost hyperfine component of its iodine line. The spectrometer setup and detection electronics are described in detail in [28], although the offset frequencies given there are NOT those relevant to this thesis. The 699 was offset by a fixed frequency of -21.5 MHz from the iodine lock point (after implementation of the 617 MHz EOM - see Secs. 4.2 and 4.3.1), so that the laser wavelength was twice that of the $^2\mathrm{S}_{1/2} \leftrightarrow {}^2\mathrm{P}_{1/2}|F = 2\rangle$

transition. The detection laser was nominally offset by +804.9 MHz from its iodine lock point, but a double-pass AOM in the iodine spectrometer allowed us to vary the offset by about 10 MHz in either direction. The nominal offset was such that the BD frequency at the trap was 8 MHz red of the cycling transition frequency with the typical offset to provide Doppler cooling of the ions (see Sec.3.2.) Because of the large slope of the cycling transition scattering rate at this detuning, any increase in linewidth or drift of the detection laser led to broadening of the Poissonian distribution of detected photons for ions in $|\downarrow\rangle$, decreasing our detection efficiency. Our tolerances for the 699 linewidth and drift were much looser, since efficient optical pumping only required the ions to scatter a few photons over several μs.

We used a Burleigh model #SA-PLUS-200-B1 spectrum analyzer and a traveling-cart wavemeter [51, 52] for rough diagnostics of the laser mode structure and wavelength. An arrangement of beamsplitters and mirrors allowed us to monitor any one of the three lasers at any time. The wavemeter read out the laser wavelength to six significant digits with an update time < 1 s, allowing us to tune the lasers to within ~ 1 GHz of the desired frequencies with ease. The quoted laser wavelengths, e.g., 626.266 nm for the detection laser, are exactly the wavemeter readings. These wavelengths agree with previously measured values [53]. The wavemeter could also read out a seventh digit with update time ~ 10 s, but this feature was rarely used. The spectrum analyzer had an FSR of 2 GHz and was especially useful for observing mode hops while tuning the thick etalon. Typically such mode hops changed the frequency of the laser by the laser cavity FSR of 150 MHz, which was too small to observe on the wavemeter but could be readily resolved on the spectrum analyzer. Occasionally we wanted to measure the frequency of the Raman laser to a precision better than that provided by the wavemeter. By coupling both the Raman laser and the detection laser into the spectrum analyzer simultaneously, we could obtain the difference of laser frequencies to a precision of ~ 10 MHz modulo 2 GHz. Combining this information with the wavemeter reading gave the absolute frequency of the Raman laser to

$\sim$ 10 MHz.

4.2 Resonant Doubling to 313 nm

The apparatus described in the last section all sat on a single optical table (the "red table"). The rest of the apparatus, including the ion trap, sat on a separate table (the "UV table"), and the 626 nm light from the red table was carried to the UV table by single-mode optical fibers. We applied a controlled torque to each fiber to cancel the natural fiber birefringence with the induced stress birefringence. This scheme largely decoupled optical adjustments on the red table from those on the UV table. The light from the 699 passed through a resonant electro-optic modulator (EOM) operating at 617 MHz before coupling into the fiber. When this EOM was switched on, the first blue sideband of the 699 light provided BOP light (see Sec. 3.3.4.) For the experiment described in Section 5, we had not yet implemented the EOM and generated the BOP beam using an AOM (see Sec. 4.3.1.)

After leaving the fibers, the detection and 699 beams were coupled into a pair of resonant doubling cavities containing a β-barium borate (BBO) crystal, which generated the UV under type II critical phase-matching [54]. The fiber birefringence rotated the beam polarizations to give nearly P-polarized ($\vec{E}$ parallel to the optical table) inputs to the cavities. The cavities consisted of three mirrors shared by both beams and two mirrors mounted on PZTs, one mirror for each beam. This arrangement defined two bowtie cavities with the two resonant beams circulating through a single BBO crystal. The optical design was that described in [28], except that the PZT-mounted mirror of the 699 doubling cavity was moved slightly to make the doubling cavity FSR equal to 617 MHz. This allowed resonant doubling of both the carrier and EOM sidebands of the 699 light in the same cavity. Each cavity was actively stabilized so that the

cavity resonance frequency matched the frequency of the incoming red light. The error signal was derived by polarization spectroscopy of the cavity itself. The doubling crystal was cut so that the phase-matched red beam entered the crystal at Brewster's angle for P-polarization of the red beam. However, S-polarized red light was partially reflected from the crystal surface, so that the cavity loss was different for the two polarizations. The resulting error signal for the fundamental cavity mode was exactly that obtained by the Hänsch-Couillaud method [48], and was fed back to the mirror PZT with a servo system similar to that used for locking the lasers to the reference cavities (Sec. 4.1). The overall loop bandwidth was again set by the PZT resonant frequency of ~ 40 kHz.

The resonant buildup of the red beam greatly enhanced the efficiency of UV generation. The UV output power P_{UV} for single-pass doubling of a red beam with power P_{SP} is

$$P_{\mathrm{UV}} = \eta_{\mathrm{dbl}} P_{\mathrm{SP}}^2 \tag{4.1}$$

where $\eta_{\mathrm{dbl}} \sim 3 - 5 \times 10^{-4}\mathrm{W}^{-1}$ for BBO. The resonant cavity enhances the power P_{SP} passing through the crystal by about an order of magnitude over the input power P_{red}, so that the UV power is much larger than that obtained without the cavity. We express the overall efficiency of the doubling process as $\eta_{\mathrm{dbl}} = P_{\mathrm{UV}}/P_{\mathrm{red}}^2$. For the detection and 699 beams, we typically achieved doubling efficiencies of $0.05 - 0.10$ W^{-1}. We then obtained typically 1–2 mW of power in the BD beam (the doubled detection beam) and several hundred μW in the RD beam (the doubled 699 beam). The UV light exiting the doubler was S-polarized (electric field parallel to the optical table) due to the type II phase-matching.

The high UV powers (several mW) provided by the resonant doubling were essential for our experiments. However, residual noise of the cavity resonance relative to the laser frequency caused fluctuations of the UV power. The residual frequency noise mostly arose from spectral components of the laser frequency noise that lay above the lock bandwidth. If this residual noise

gave an effective linewidth that was a significant fraction of the doubling cavity bandwidth ($\sim$ 2.5 MHz FWHM for the detection and 699 cavities), the frequency noise of the red beam caused intensity noise of the doubled beam through Eq. (4.1). The detection laser linewidth was much smaller than the doubling cavity bandwidth, so this mechanism created little intensity noise for BD. While the 699 linewidth was sometimes larger than the doubling cavity bandwidth, we allowed sufficient optical pumping times to make up for any intensity fluctuations in RD.

The Raman light was coupled into an LAS (now Spectra-Physics) Wavetrain SC resonant cavity doubler containing a lithium borate (LBO) crystal, which was type II critically phase-matched for UV generation. The input to the cavity was again P-polarized. The cavity for this doubler consisted of two mirrors and a prism mounted on a PZT, as shown in Fig. 4.3. The cavity resonance was servoed to the red beam frequency by the Pound-Drever-Hall method [55] with feedback of the error signal to the PZT through a servo with proportional, integral, and derivative (PID) gain. The servo bandwidth was $\sim$ 6 kHz and was presumably set by the PZT resonance. We observed doubling efficiencies of $\eta_{\mathrm{dbl}} \sim 0.15/\mathrm{W}$ for this cavity. Because the length of the Wavetrain cavity was about a factor of 4 smaller than the lengths of the other doubling cavities, we believe that the bandwidth was significantly higher than that of the other cavities. The Raman laser linewidth was less than 1 MHz, so the doubling did not introduce intensity noise. The UV light from the cavity was S-polarized.

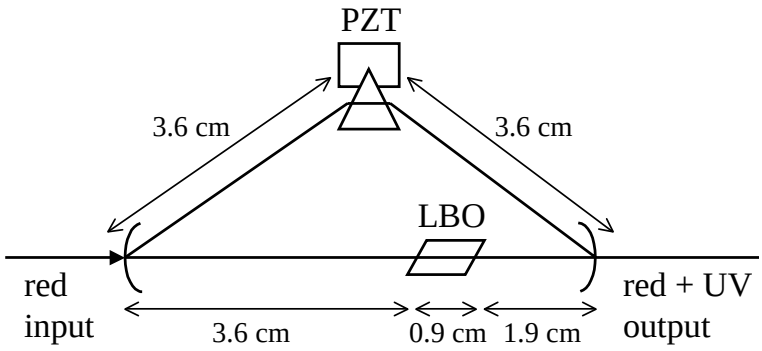

Figure 4.3: Optical design of the Wavetrain SC doubling cavity. PZT = piezoelectric transducer, LBO = lithium borate crystal.

4.3 UV Beam Control

4.3.1 BD and RD Beams

On leaving the doubling cavity, the BD beam passed through a noiseater setup using a 80 MHz AOM (Fig. 4.4) to stabilize its intensity. The signal from the photodetector was summed with an externally controlled setpoint and filtered as shown in the circuit diagram of Fig. 4.5. The diode clamps on the last amplifier stage help the circuit recover from dye laser "dropouts", momentary events in which the red laser power drops to zero. The filtered signal was input to a mixer in the RF drive setup for the AOM, so that the signal level controlled the RF power to the AOM. If the laser power exceeded the setpoint, the AOM turned on, deflecting the excess power into the AOM sideband. An aperture blocked the deflected beam but let the undeflected beam pass through. Though the noiseater can remove power from the beam, it cannot increase the beam power. If noise causes the beam power to drop below the setpoint, the servo is ineffective in removing the noise. Hence the setpoint power was typically half the power entering the noiseater. This setting was found effective in servoing out intensity fluctuations.

The overall noiseater bandwidth is limited by the transit time T_{trans} of the acoustic wave

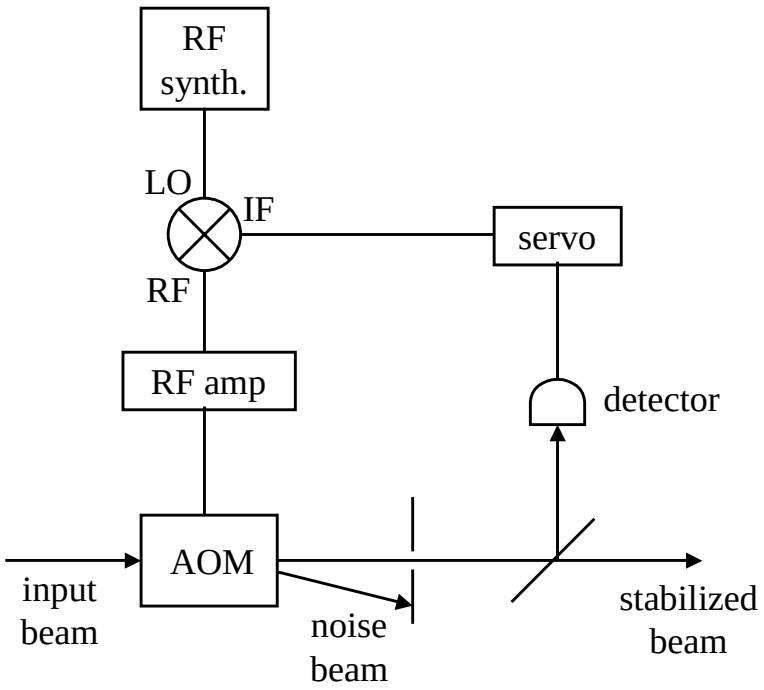

Figure 4.4: RF/optical schematic for "noiseater" intensity stabilization. PD = photodetector.

in the AOM between the AOM's RF/acoustic transducer and the position of the beam. The AOMs used in all the UV beamlines were made of quartz, which has a sound velocity of about 6000 m/s. For a beam positioned 6 mm from the transducer, the transit time is thus 1 μs. The transducer induces stress birefringence in the quartz, so the beam polarization changes unpredictably if the beam is moved much closer than 6 mm to the transducer. In practice, the servo begins to oscillate slightly at the resonant frequency $1/T_{\mathrm{trans}}$ for servo unity-gain frequencies much higher than $1/(2T_{\mathrm{trans}})$. The resulting noiseater bandwidth is then typically $\sim$ 50 kHz.

After the noiseater, BD passed through a switch arrangement consisting of a –80 MHz AOM followed by an aperture. The AOM was arranged so that its first red sideband passed through the aperture, while the unshifted beam was blocked. Hence BD passed through to the trap only when the RF driving the switch AOM was turned on. Figure 4.6 shows the entire BD beamline from the doubling cavity to the trap. We specify the selection of the redshifted beam by designating the AOM as having –80 MHz RF input; for a blueshifted beam we would write +80 MHz. A variable RF attenuator controlled the RF power to the switch AOM, allowing us to vary the BD power easily. With no attenuation, the switch efficiency was about 90%. We also used an optical neutral-density filter (ND 0.3) mounted on an electrically controlled flipper mirror for coarse control of the BD power.

In the version of the RD beamline after implementation of the 617 MHz EOM in the 699 beamline, RD passed through an 80 MHz AOM twice, once with a –80 MHz shift and once with a +80 MHz shift in the UV, to give a net zero shift. This AOM was followed by an aperture arranged so that RD arrived at the trap only if the RF driving the AOM was turned on. A variable RF attenuator in the RF drive for this AOM allowed us to control the RD and BOP power. With no attenuation, the switch efficiency was about 80%. After the switch, RD was

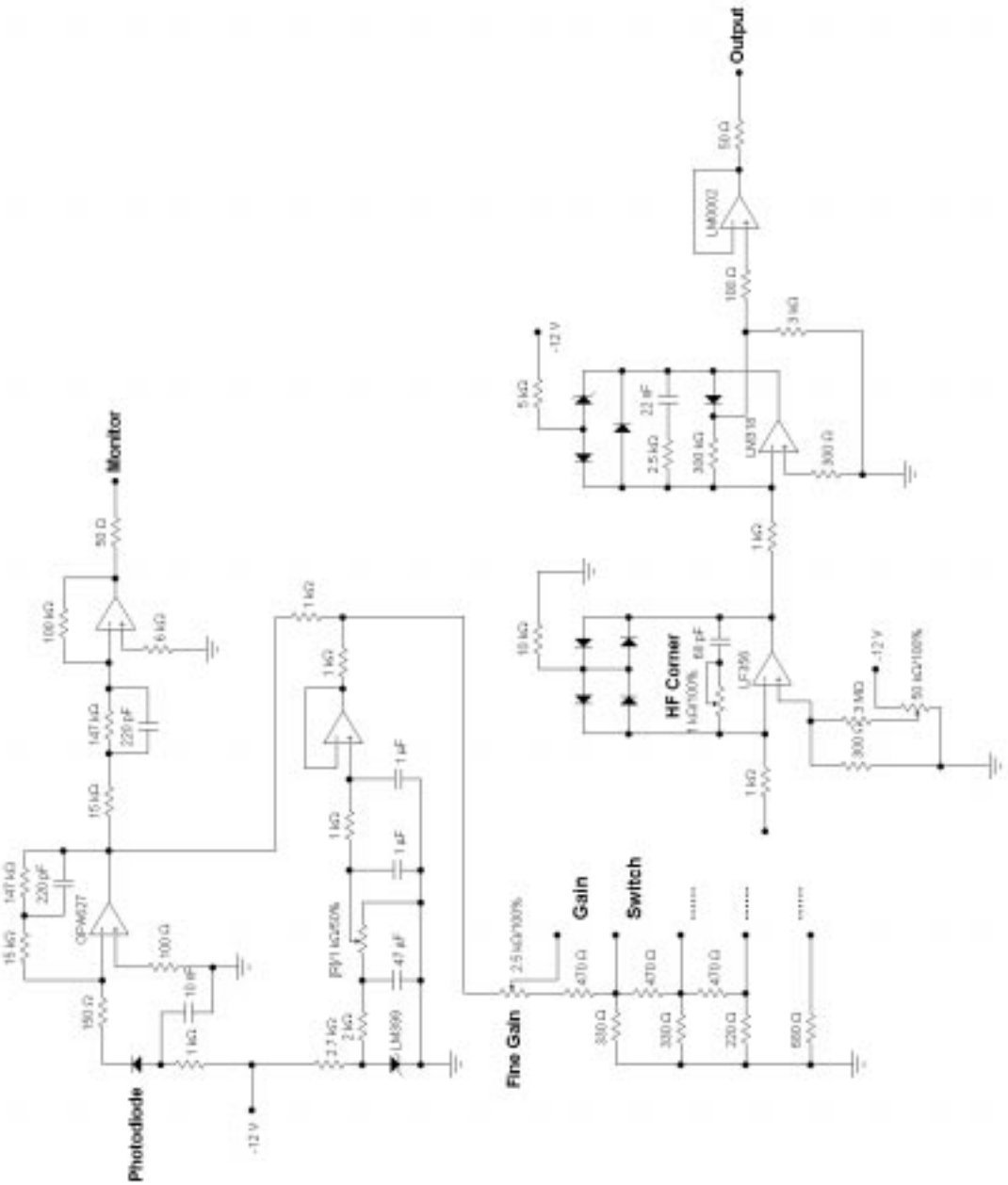

Figure 4.5: Circuit diagram for the servo used in the noiseater.

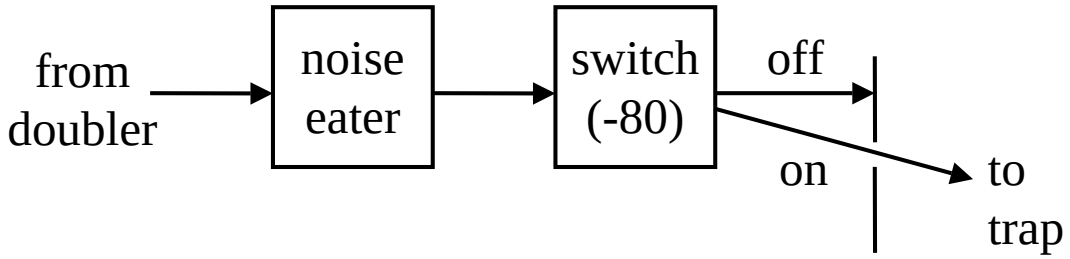

Figure 4.6: Schematic of the BD beamline from the doubling cavity to the trap. Frequency shifts of deflected beams are indicated in parentheses, in units of MHz.

combined with BD on a beamsplitter and the BD, RD beams copropagated through a polarizer and a finely adjustable quarter-wave plate to ensure σ^+ polarization in the atomic basis. The beams then passed through a final focusing lens of focal length 10 cm and into the trap. Typically the diameter of each beam was about 100 μm at the ion string. Here we roughly quantify the "beam diameter" as twice the distance between the point of maximum intensity in the transverse profile and the point at which the intensity drops by a factor of $1/e$. The focusing lens was mounted on an XYZ micrometer stage which allowed repeatable positioning of the beam at the ion to within a few μm.

In the version of the RD beamline used for the experiment of Section 5, the RD beam was split with power ratio of roughly 1/2. One of these beams propagated through a –80 MHz AOM switch like that used for BD and performed the usual function of the RD beam. Again a variable RF attenuator allowed control of the RD power. In this version, the 699 laser was offset by +18.5 MHz, rather than –21.5 MHz, from its iodine spectrometer (see Sec. 4.1.) The other beam passed through a +236 MHz AOM four times and then passed through a +236 MHz AOM switch. This beam performed the BOP function. The efficiency of BOP generation was only about 10% after the beamsplitter. The BD, RD, and BOP beams were combined with beamsplitters as described above.

4.3.2 Raman Beams

The geometries and polarizations used for Raman transitions in our experiments are shown in Fig. 4.7. Beams are labeled by frequency as B (the bluer beam) or R (the redder beam) and by the port at which they enter as 1, 2, or 3. Thus the bluer beam entering port 1 is denoted B1. Raman beams B1 and R1 entering port 1 are used together to drive copropagating carrier transitions between various hyperfine states according to Hamiltonian (Eq. 3.15). B1 and R2 together drive logic transitions between $|\downarrow\rangle$ and $|\uparrow\rangle$ according to Hamiltonian (**??**). B2 and R1 together drive logic transitions between the $|F = 2, m_F = 0\rangle$ and $|F = 1, m_F = 0\rangle$ states. Used by itself, beam B2 is also a convenient way to Stark shift the hyperfine transitions. Counterpropagating beams B3, R1 drive transitions involving all $3N$ motional modes and are used to investigate transverse vibrations of the ion crystal.

We generated the various Raman beams (B1, R1, etc.) from the doubled Raman light using AOMs. The doubled Raman light was first split into BR ("blue Raman") and RR ("red Raman") beams by a fixed-frequency AOM at 221 MHz. The RR beam was the undiffracted beam in this AOM, while the BR beam was the first blue sideband of the AOM. Figure 4.8 shows a schematic of the BR and RR beamlines from the splitter AOM to the trap. BR continued through another fixed-frequency "offset" AOM at +221 MHz driven by the same synthesizer. This AOM also served as a noiseater similar to that described for the BD beam, except that the polarity of the servo was reversed so that the intensity-stabilized beam was the shifted beam rather than the unshifted beam. RR was sent through a double-pass AOM with nominal frequency –200 MHz (–80 MHz for the experiment of Sec. 5.) We could vary the RF drive frequency of this AOM by about 15 MHz in either direction, enabling us to control the beat frequency between BR and RR beams over times of several μs without significantly steering the RR beam.

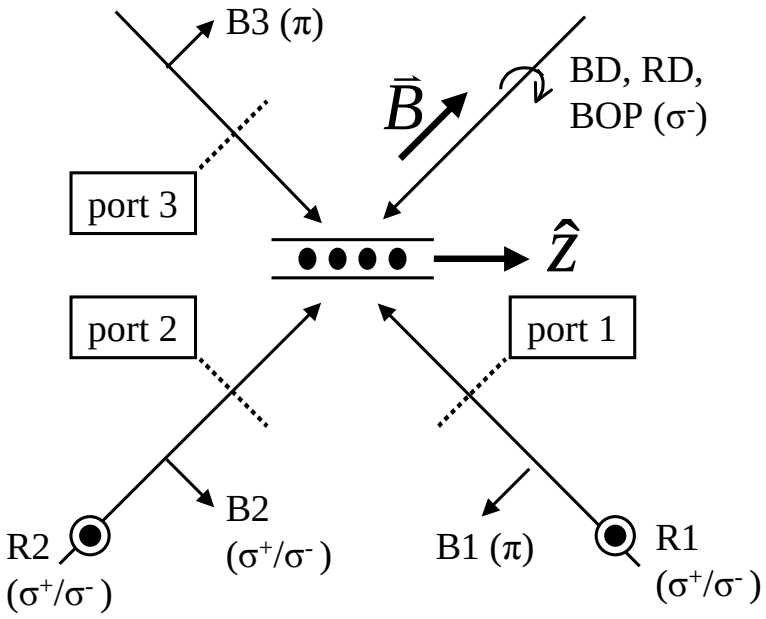

Figure 4.7: Raman beam geometry for our experiment. Beams are labeled by frequency as B (the bluer beam) or R (the redder beam) and by the port at which they enter as 1, 2, or 3. Thus the bluer beam entering port 1 is denoted B1. Polarizations are specified in the atomic basis $\{\sigma^+, \sigma^-, \pi\}$ selected by the quantization field. The trap defines the spatial coordinate system, with the trap axis along $\hat{z}$. Detection and optical pumping beams BD and RD are shown for reference.

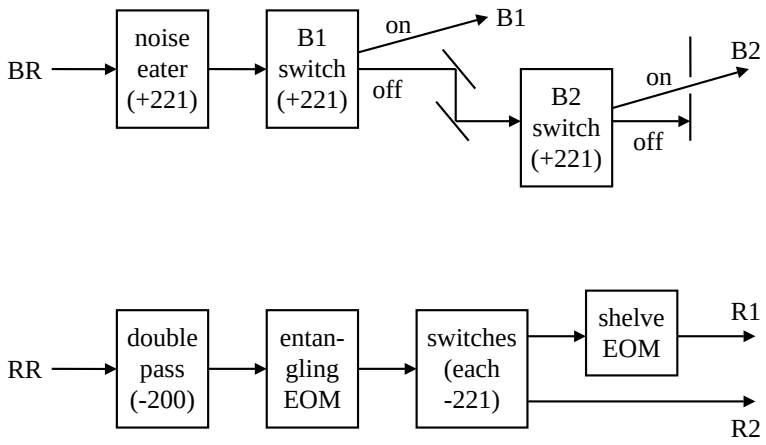

Figure 4.8: Schematic of the BR and RR beamlines from the splitter AOM to the trap. Frequency shifts of deflected beams are indicated in parentheses, in units of MHz. The center frequency is indicated for the double-pass AOM. The switch arrangement for RR is the same as for BR, but is compressed for clarity.

After the double-pass, RR was intensity-stabilized by a noiseater like that used for BD. RR then passed through a resonant EOM with frequency 17.67 MHz. Turning on this EOM provided the additional Raman frequency for the two-ion entangling gate (see Sec. 5.2.)

The BR beam was split into separate beams B1, B2 using two +221 AOM switches. The aperture after the first AOM was replaced with a mirror that separated the shifted and unshifted beams. The shifted beam was sent to the trap. The unshifted beam passed through the second switch, which was set up in the usual way. Thus the beam passed by the second switch and the shifted beam from the first switch were both 221 MHz blue of the original BR beam. We generated R1 and R2 from RR in the same way, except that the AOM switches gave a shift of –221 MHz. After the switch arrangement, R1 passed through a resonant EOM with frequency 32.67 MHz. Turning on this EOM enabled us to access the "shelving" Raman transitions (see Sec. 6.1.)

R1 and B1 were combined on a polarizing beamsplitter (PBS), B1 being first sent through a half-wave plate to rotate it to P polarization. The B1 polarization was then parallel to the quantization field, giving it π polarization in the atomic basis. The R1 polarization was perpendicular to the quantization field, but since the R1 propagation vector was also perpendicular to the quantization field, the R1 power was constrained to be divided equally between the atomic σ^+ and σ^- polarizations. The copropagating B1, R1 beams passed through a 10 cm focusing lens into the trap. The lens was mounted on an XYZ micrometer stage like that used for the BD focusing lens. The beam size at the ion was usually about 20×40 μm, with the long dimension parallel to the optical table. Residual astigmatism from the doubling cavity caused the ellipticity of the beam spot.

For the experiments in quantum logic on the $^2\mathrm{S}_{1/2}|F=2, m_F=0\rangle \leftrightarrow {}^2\mathrm{S}_{1/2}|F=1, m_F=0\rangle$ transition (Secs. 7.1 and 7.3), R2 and B2 were combined on a PBS as well, with B2 rotated to P polarization. Since R2 and B2 both propagated parallel to the quantization field, the R2 (B2) polarization was $\hat{\epsilon}_{\mathrm{R(B)}} = \sigma^+ + \exp[i\phi_{\mathrm{R(B)}}]\ \sigma^-$ in the atomic basis, with $\phi_{\mathrm{R}} = \phi_{\mathrm{B}} + \pi$ to preserve the orthogonality of the R2, B2 polarizations. After the PBS, the copropagating R2, B2 beams were sent through a finely adjustable quarter-wave plate. This waveplate enabled us to control the relative amplitudes of σ^+ and σ^- light in the R2 beam, which proved essential in implementing our entangling gate on the $|{\downarrow}\rangle \leftrightarrow |{\uparrow}\rangle$ transition (see Sec. 5.2.) For the decoherence-free subspace experiment, the PBS was removed and B2 was sent in nearly parallel to R2 using a pickoff mirror. In this case, we controlled the R2 and B2 polarizations independently by inserting a separate quarter-wave plate in each beam (see Sec. 8.2.) B2 and R2 again passed through a 10 cm focusing lens on an XYZ stage before entering the trap.

4.4 RF Generation and Control

All the RF used to drive the 80 MHz UV AOMs originated from a single HP 8640 RF generator set to exactly 80 MHz. The RF was split five ways and passed through isolation amplifiers to prevent crosstalk between channels. The channel driving the BD noiseater passed through its servo-controlled mixer, while the channels driving the switch AOMs were input to the RF switchbox. This switchbox was a collection of Mini-Circuits ZASW-series TTL-controlled RF switches that translated the TTL logic generated by the experiment control system into switching of the RF power and hence to switching of the UV beams. The RF switches had very high isolation (40–60 dB) to minimize optical power leakage through the AOMs when the RF was nominally off. Each channel was then amplified to ~ 800 mW power and sent to its AOM.

The 221 MHz signal driving the Raman splitter and BR offset AOMs was generated by an HP 8662 RF synthesizer. The signal was split into separate channels for each AOM and sent through isolation amplifiers. Each channel was then amplified to 1–2 W and sent to the AOMs. For the experiment of Section 5, we drove the 236 MHz AOMs used in the BOP beamline by amplifying the signal from an HP 8640 RF generator.

Our experiments required that we switch the frequency of the RF driving the RR double-pass AOM in a matter of microseconds. A single RF synthesizer with the desired frequency stability could not switch frequencies sufficiently quickly, so we used a TTL-controlled RF multiplexer constructed using Mini-Circuits ZYSW-series RF switches to generate the RF for the double-pass AOM. The inputs to the multiplexer were driven by the ~ 200 MHz mixing products of several HP 3335 RF synthesizers operating near 50 MHz with a single Fluke 6160 RF synthesizer operating at 150 MHz. We generated the RF in this way because suitable 200 MHz

RF synthesizers would have been prohibitively expensive. After the multiplexer, the RF was amplified to 1–2 W and sent to the double-pass AOM. All the synthesizers driving AOMs in the Raman beamlines were phase-locked together, ensuring temporal coherence of the Raman beams.

We usually determined the frequencies of the carrier and sideband transitions by sweeping out the ion fluorescence spectrum as a function of two-photon detuning. In this case we used a single GPIB-controlled HP 8660 RF synthesizer to drive the RR double-pass AOM. The GPIB interface allowed us to change the synthesizer frequency every few ms. For this application we collected data over about 100 ms at each frequency, so the dead-time involved in changing the synthesizer frequency did not affect the experiment duty cycle significantly.

For the experiment of Section 5, we drove the 80 MHz RR double-pass AOM using the HP 3335 RF synthesizers directly as inputs to the RF multiplexer. The output of the multiplexer was amplified to $\sim$ 800 mW and sent to the AOM.

The RF signals driving the two resonant EOMs were generated by HP 3335 synthesizers, amplified to $\sim$ 100 mW, and sent to the EOM resonant tank circuits. The inductor for each tank circuit was a coil of 14 gauge copper wire of several μH inductance enclosed in a thick metal box. The inductor was attached across a pair of banana plugs, the connector type supplied for this EOM (Linos Photonics PM 25). The EOM typically provided a capacitance of $\sim$ 30 pF for the tank circuit; we could adjust the tank resonance by attaching additional pF-scale capacitors across the banana plugs. The input RF power drove a loop antenna of 14 gauge copper wire, also enclosed in the box, which magnetically coupled to the tank circuit. We typically attained

a Q factor of 50 when the tank circuit was attached to the EOM. Higher Q factors were neither necessary nor desirable, as they would have limited the EOM resonant bandwidth. The resonant EOM assemblies were further enclosed in aluminum boxes to minimize RF radiation from the (snort) banana plugs. How Linos gets away with this banana plug business, I don't know.

4.5 Detection Optics

Fig 4.9 shows a schematic of the optical system used for detecting the ion fluorescence. The objective was an $f/1$ six-element compound lens with a working distance of 40 mm. After passing through the intermediate aperture (600 μm diameter) in the image plane of the objective, the image was further magnified by a UV doublet (2.5 cm focal length). The fluorescence was detected by either a Photek microchannel plate imaging tube (the "imager") or a Hamamatsu H6240-01 photomultiplier tube (PMT). We directed the fluorescence toward one or the other detection device with a mirror mounted on an electronically controlled flipper. The imager had quantum efficiency of about 5%, rather lower than the PMT quantum efficiency of about 20%. However, the imager's effective spatial resolution of several μm (measured in the ion object plane) was invaluable during loading, as we could readily distinguish the number of ions in the trap by lowering the endcap voltage somewhat. We used the PMT to collect all the data presented in this thesis. Since the PMT had no spatial discrimination, we counted the total number of photons arriving from the ion crystal rather than the number arriving from each individual ion. Thus our data allowed us to distinguish only between the cases of zero, one, two,... ions bright, which did not constitute a full readout of the state of the quantum register. The experiments reported here did not suffer unduly from this restriction.

During the detection phase, off-resonant repumping and imperfect BD polarization caused

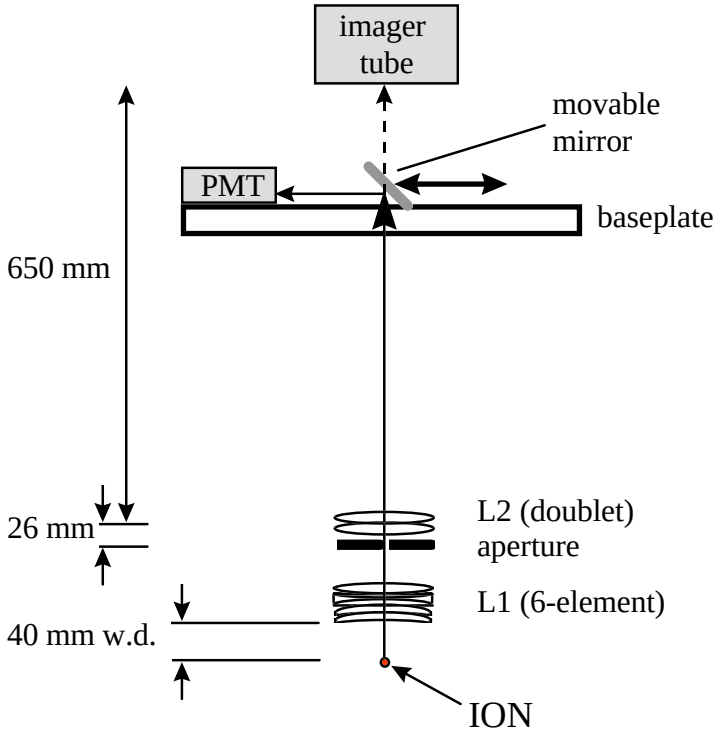

Figure 4.9: Schematic of the detection optics. L1 is the objective lens, L2 the reimaging lens.

the spin state of each ion to relax toward equilibrium between the bright $|\downarrow\rangle$ state and the rest of the $^2S_{1/2}$ manifold, which was dark. Typically an ion relaxed by 1% after scattering $\sim 10^4$ photons (see Sec. 3.2). Hence the small detection f-number and high PMT quantum efficiency were essential to our high spin discrimination efficiency.

4.6 Experiment Control and Data Acquisition

Each of our experiments was specified by a sequence of logical states of precisely defined timing and duration. These logic states controlled the switch AOMs and the EOMs (through the RF switchbox) and the frequency of the Raman beatnote (through the RF multiplexer). We specified most of the experiment parameters using a Microsoft Visual C++ program running on a standard PC, which allowed us to reprogram the control sequence in a matter of a few seconds. The Visual C++ program downloaded the control sequence by GPIB (IEEE 488) interface to a Hewlett-Packard (HP) 8175 digital pulse generator, which produced independent pulse sequences on up to 24 TTL channels with 20 ns time resolution. The Visual C++ program also instructed a Stanford Instruments DG535 pulse generator to send out TTL pulses at the repetition rate of the experiment. Each pulse triggered the HP 8175, beginning an experiment cycle.

As described in Section 3.2, each shot of the experiment ended with a detection period in which BD alone was turned on for several hundred μs. In each detection period, the TTL pulse stream produced by the PMT was sent to a National Instruments AT-MIO data acquisition card, which counted the number of TTL pulses for that shot and sent the result to a standard PC. A National Instruments LabView program running on the PC built up a histogram and graphically displayed it with about 1 s update time. In many experiments the LabView program

stepped the phase of one of the HP 3335 RF synthesizers and built up a histogram at each step. Each histogram typically consisted of 1000 shots.

We used a different data acquisition procedure for two essential functions of the experiment: finding the spectrum of ion fluorescence as a function of two-photon detuning and observing Rabi flopping on a particular Raman transition. For each function we could build up good statistics in 10–100 shots, rather than the 1000 shots used for the histogram data. Hence we could increase our data rate by stepping the independent variable on a timescale less than a millisecond, rather than stepping the variable about every 3 ms, as required by the LabView program. To build up consistent statistics, we had to update the independent variable in "real time", i.e., at a time specified to about 1 ms, the duration of a single shot. The frequent CPU interrupts associated with Microsoft Windows would have resulted in severe update errors, so we implemented the spectrum and flopping functions with separate PCs running under MS-DOS. The number of pulses from the PMT was counted over a fixed time, usually about 100 ms, and was read out to the PC.

Performing the spectrum function required that we apply a Raman pulse of a fixed duration at a fixed time in each shot of the experiment, but that we update the RR double-pass frequency in real time. The duration and timing of the Raman pulse were specified by the Visual C++ program through the HP 8175, while the spectrum PC determined the double-pass frequency. A C program running on the spectrum PC allowed us to specify the spectrum sweep parameters and graphically displayed the spectrum as it was acquired. The spectrum PC updated the double-pass frequency by GPIB commands to the HP 8660 synthesizer.

For the Rabi flopping function, we applied a Raman pulse of a variable duration at a fixed double-pass frequency and a fixed time in each shot. Here the Visual C++ program specified the double-pass frequency and the maximum length of time allowed for the pulse, while the flopping PC determined the pulse duration. A C program running on the flopping PC specified the sweep parameters and displayed the flopping curve. The flopping PC used a GPIB interface to instruct another Stanford Instruments DG535 pulse generator to put out TTL pulses of the desired duration. The TTL outputs of this "flopping" DG535 were connected to a set of logical OR gates through an array of manual switches. The other inputs to the OR gates were TTL outputs of the HP 8175. The outputs of the OR gates were input to the RF switchbox. Hence, when the manual switch for a channel was on, the RF controlled by that channel switched on when instructed by either the flopping DG535 or the HP8175. The Raman beams to be turned on during the flopping pulse were specified by these manual switches.

For many of the experiments reported here, we needed to change the trap endcap voltage multiple times within a single shot of the experiment. The voltage inputs to the trap endcap electrodes originated from the "DC switchbox", which could switch between two possible voltage states in a matter of a few microseconds. We controlled the switching either manually or via a TTL input. The voltages of the two possible switchbox states were set by manual potentiometers. The decoherence-free subspace experiment (Sec. 8) required switching between three voltage states, which we implemented by summing the outputs of two identical DC switchboxes. We ensured smooth transitions between voltage states by passing the voltage output of the switchbox arrangement through a 4-pole Bessel filter with cutoff frequency ~ 1 MHz. This filter attenuated high frequencies while preserving the phase relation between low-frequency pulse components so as not to distort the pulse shape. The TTL inputs to the DC switchboxes originated from either the DG535s or the HP8175. Directly connecting the TTL control signals to the switchbox inputs allowed 60 Hz line noise to infiltrate the voltage inputs to the endcap

electrodes, degrading the two-ion logic gate (see Sec. 5). To achieve the < 5 mV stability required for the two-ion gate, we isolated the TTL inputs to the switchboxes with optocouplers. For much the same reason, we electrically isolated the switchbox cases from the racks in which the switchboxes were mounted. Isolating the endcap voltage from 60 Hz noise proved to be a huge torment, and a future voltage multiplexing system must take serious precautions against this problem.

Chapter 5

Multiparticle Entanglement

So far we have described initialization of our quantum register (Secs. 3.2 and 3.3.4), operations on single qubits (Sec. 3.3.1), and detection of the register state (Sec. 3.2). However, one more ingredient is needed to perform universal quantum logic: a gate that entangles two particles [56, 57, 58]. This gate can be a quantum XOR [38, 59], a phase gate [2, 60, 61], or any of a class of equivalent gates. We implemented the entangling gate of Mølmer and Sørensen [62, 63] for strings of two and four ions [64], realizing the operations

$$|\downarrow\downarrow\rangle \rightarrow |\downarrow\downarrow\rangle + |\uparrow\uparrow\rangle \tag{5.1}$$

$$|\downarrow\downarrow\downarrow\downarrow\rangle \rightarrow |\downarrow\downarrow\downarrow\downarrow\rangle + |\uparrow\uparrow\uparrow\uparrow\rangle$$

One can use this gate on two ions in conjunction with single-qubit operations to construct an XOR gate [62], so this gate enables universal quantum logic. Of course, our experiment only approximates the evolution (5.1). However, measurements on the states produced in the experiment showed that those states were, in fact, entangled. We used the two-ion version of this gate as our fundamental entangling gate in the quantum logic experiments described in this thesis.

5.1 Theory of the Entangling Gate

To apply the Mølmer–Sørensen entangling gate to an ion crystal, one off-resonantly drives both the red and blue sidebands of a particular motional mode of the crystal. The detunings Δ_M from the sidebands are equal and opposite. Each ion is coupled to each sideband with the same coupling strength, written Ω_{sb}. The relevant level scheme for two ions is shown in Fig. 5.1. We obtain the coupling condition by keeping the intensity of all Raman beams constant across the ion crystal and by choosing a motional mode in which all ions have equal motional amplitudes, i.e., $|v_i^{(k)}|$ is independent of the ion index i (see Eq. 2.26.)

The essential features of the entangling gate are intuitively clear in the far-detuned limit $\Delta_M \gg \Omega_{\mathrm{sb}}$. Considering only two ions for clarity, we see that the intermediate spin state $|\downarrow\uparrow\rangle + |\uparrow\downarrow\rangle$ is only virtually populated, while the $|\downarrow\downarrow\rangle \leftrightarrow |\uparrow\uparrow\rangle$ transition is resonant. The singlet spin state $|\downarrow\uparrow\rangle - |\uparrow\downarrow\rangle$ does not take part in the dynamics. The situation is reminiscent of resonant two-photon excitation through a virtual intermediate level [65], as in, e.g., spectroscopy of the rubidium 5S $\leftrightarrow$ 5D transition. However, the "two-photon resonance" here corresponds to simultaneous excitation of two ions, rather than excitation of a high-lying level of a single atom, and the off-resonant "single-photon" couplings are actually Raman processes. Exploiting the analogy to two-photon spectroscopy, we see that the Rabi frequency for the pathway through the intermediate $|n+1\rangle$ ($|n-1\rangle$) state is proportional to $(n+1)\Omega_{\mathrm{sb}}^2/\Delta_M$ ($n\Omega_{\mathrm{sb}}^2/\Delta_M$) in the Lamb-Dicke limit. The factors of n come from the harmonic oscillator raising and lowering operators as in Eq. (3.22). The two paths interfere destructively, so the overall Rabi frequency for the $|\downarrow\downarrow\rangle \leftrightarrow |\uparrow\uparrow\rangle$ transition is proportional to $\Omega_{\mathrm{sb}}^2/\Delta_M$. In the Lamb-Dicke limit, the Rabi frequency is independent of n, so the gate is insensitive to the initial motional state of the ion crystal! In view of the heating problem in our traps (Sec. 7.4), this feature gives the Mølmer–Sørensen gate a distinct advantage over the Cirac-Zoller XOR [38], which requires that the ion

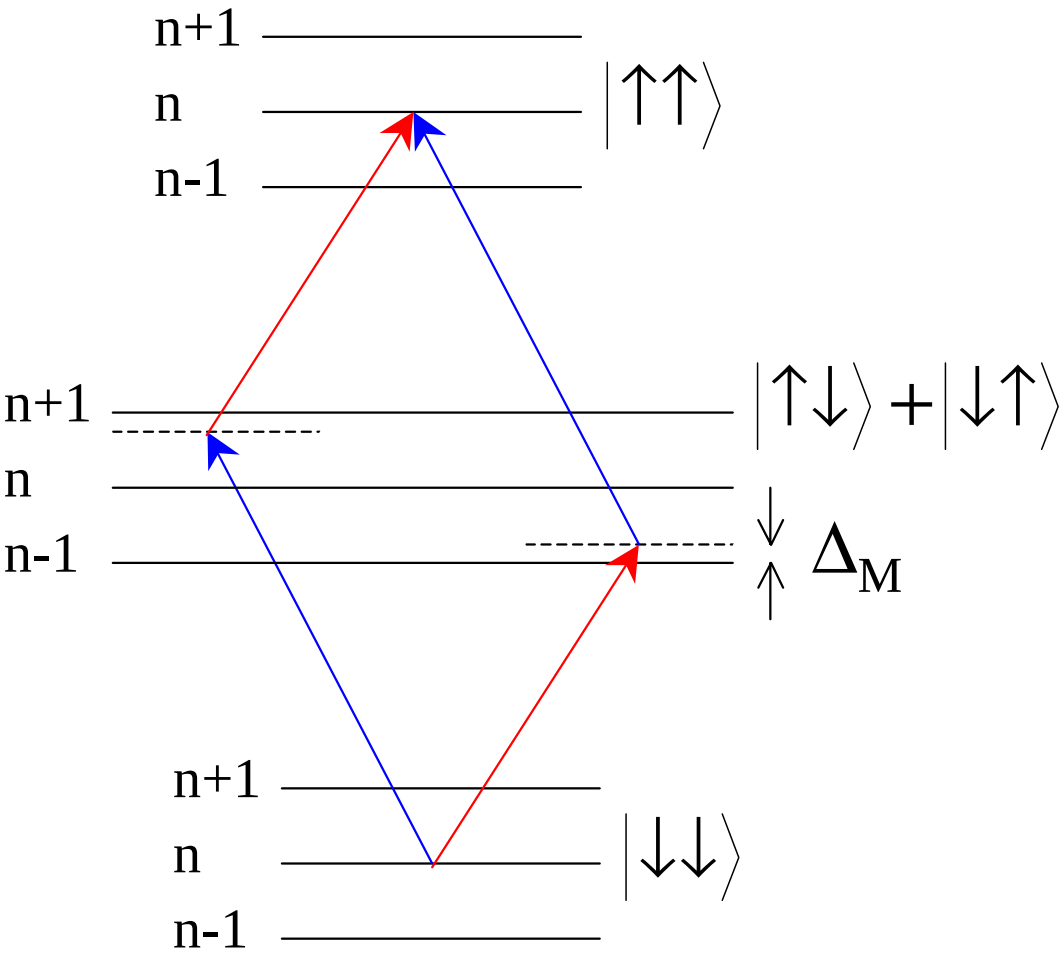

Figure 5.1: Relevant level scheme for the two-ion version of the entangling gate. The arrows represent Raman processes driven by pairs of Raman beams. The two pathways through the intermediate $|\downarrow\uparrow\rangle + |\uparrow\downarrow\rangle$ state exhibit quantum interference.

crystal start in a Fock state of the motion.

It takes a relatively long time ($\gg 1/\Omega_{\rm sb}$) to apply the entangling gate in the far-detuned limit, giving decoherence a long time to act and severely limiting the gate fidelity. However, as we will see, one can obtain the evolution (Eq. 5.1) even if Δ_M is on the order of $\Omega_{\rm sb}$, for carefully chosen values of Δ_M. In the experiment we used this "nonperturbative" gate operation to speed up the gate, allowing high-fidelity gate operation.

To analyze the nonperturbative regime, we return to the basic interaction Hamiltonian consisting of the two off-resonant Raman drives. Transforming to an interaction picture with respect to the free evolution of the ion spin and motion, and assuming the Lamb-Dicke limit, the Hamiltonian for N ions takes the form [66]

$$\mathbf{H}_M = (i\eta_k\Omega_{\rm sb}\mathbf{J}_+\mathbf{a}^\dagger e^{-i\Delta_M t} + \text{h.c.}) + (i\eta_k\Omega_{\rm sb}\mathbf{J}_+\mathbf{a}e^{-i\Delta_M t} + \text{h.c.}) \tag{5.2}$$

$$= -\eta_k\Omega_{\rm sb}\mathbf{J}_y[\mathbf{a}e^{-i\Delta_M t} + \text{h.c.}] \tag{5.3}$$

where the pair of Raman beams driving the blue (red) sideband has relative phase $\phi_{j,B}$ ($\phi_{j,R}$) at ion j and η_k is the Lamb-Dicke parameter for the logic mode (see Eq. 3.28). In Eq. (5.3) we have omitted the phases $\phi_{j,B}$, $\phi_{j,R}$, but we can insert them again later by the transformations

$$\mathbf{S}_{j,+} \to e^{i\phi_j}\mathbf{S}_{j,+} \qquad \mathbf{a} \to e^{-i\delta\phi}\mathbf{a} \tag{5.4}$$

$$\phi_j \equiv (\phi_{j,B} + \phi_{j,R})/2 \qquad \delta\phi \equiv (\phi_{j,B} - \phi_{j,R})/2 \tag{5.5}$$

Here $\delta\phi$ does not depend on j.

The full dynamics under the Hamiltonian (5.3) is given by the evolution operator $\mathbf{U}_M$ satisfying the Schrödinger equation $i\, d\mathbf{U}_M/dt = \mathbf{H}_M\mathbf{U}_M$. Given an initial state $|\psi(t=0)\rangle$, the

state at any later time is $|\psi(t)\rangle = \mathbf{U}_M(t)|\psi(0)\rangle$. Following [66], we make an ansatz for $\mathbf{U}_M$ of form

$$\mathbf{U}_M = \exp[ik(t)\mathbf{J}_y^2]\ \exp[h(t)\mathbf{J}_y\mathbf{a}^\dagger]\ \exp[-h^*(t)\mathbf{J}_y\mathbf{a}] \tag{5.6}$$

where $k(t)$, $h(t)$ are c-number functions that govern the dynamics. Substituting this ansatz into the Schrödinger equation for $\mathbf{U}_M$, we find

$$k(t) = \frac{\eta_k^2\Omega_{\rm sb}^2}{\Delta_M}\ t\ - i(e^{-i\Delta_M t} - 1)\left(\frac{\eta_k\Omega_{\rm sb}}{\Delta_M}\right)^2 \tag{5.7}$$

$$h(t) = \frac{\eta_k\Omega_{\rm sb}}{\Delta_M}(e^{i\Delta_M t} - 1) \tag{5.8}$$

The first factor in Eq. (5.6) describes the entanglement of the ions through "two-photon" transitions. The other two factors describe the virtual red- and blue-sideband transitions induced by the Raman beams. From a mathematical standpoint, we can regard the first factor as a kind of geometric phase factor generated by the noncommutativity of the blue and red sideband drives. More physically, we can say that the virtual excitation of the motional mode carries quantum information between the ions.

While the evolution (5.6) creates entanglement for any choice of Δ_M, we want to entangle the ion spins only with each other, not with the motional mode. Thus we want to eliminate the last two terms of Eq. (5.6), which we can do if $h(t) = 0$. Moreover, the gate operation (5.1) corresponds to the unitary operator $\exp[i\pi\mathbf{J}_y^2/2]$, so we require $k(t) = \pi/2$. These constraints are satisfied for

$$\Delta_M = 2\eta_k\Omega_{\rm sb}\sqrt{p} \qquad t = \frac{\pi\sqrt{p}}{\eta_k\Omega_{\rm sb}} \tag{5.9}$$

with p, j integers. Hence we can operate the gate (5.1) in a time as short as $\pi/(\eta_k\Omega_{\rm sb})$, if we choose Δ_M properly. This time is on the order of a sideband π-pulse time, so the sideband

Rabi frequency sets the clock speed for our quantum register. We require $\Omega_{\rm sb} \lesssim \omega_z$; otherwise the gate drive also drives off-resonant transitions that spoil the gate. Hence the trap frequency ultimately limits the clock speed.

We can use the entangling gate to generate the state $|{\downarrow}^{\rm N}\rangle + |{\uparrow}^{\rm N}\rangle$ with a single laser pulse, which greatly simplifies the use of entangled states for spectroscopy [67]. In contrast, N two-bit XORs are required to generate the same state [38]. Moreover, the time required to entangle N ions with our gate scales as $1/\eta_k^2 \propto N$, so our gate is no slower than the usual XOR method.

The simplest initial state for which the entangling gate produces nontrivial evolution is the two-ion state $|\psi(0)\rangle = |{\downarrow}{\downarrow}; n = 0\rangle$, where n is the number of phonons in the logic mode. Using Eq. (5.6), we find the normalized state

$$|\psi(t)\rangle = \frac{1}{2}\left(|{\downarrow}{\downarrow}; 0\rangle + |{\uparrow}{\uparrow}; 0\rangle\right) + \frac{1}{2}\, e^{ik(t)}\left(|{\downarrow}{\downarrow}; 0\rangle - |{\uparrow}{\uparrow}; 0\rangle\right) \tag{5.10}$$

$$- \frac{1}{2}\, e^{ik(t)} \sum_{n=1}^{\infty} \frac{(h(t))^{2n}}{\sqrt{(2n)!}} \left(|{\downarrow}{\downarrow}; n\rangle - |{\uparrow}{\uparrow}; n\rangle\right) \tag{5.11}$$

$$- \frac{i}{2}\, e^{ik(t)} \sum_{n=0}^{\infty} \frac{(h(t))^{2n+1}}{\sqrt{(2n+1)!}} \left(|{\downarrow}{\uparrow}; n\rangle + |{\uparrow}{\downarrow}; n\rangle\right) \tag{5.12}$$

The time-evolved state divides into a pure spin state, which undergoes no motional evolution, and a complicated spin/motion entangled state. For $h(t) = 0$ the spin/motion entanglement vanishes, leaving residual spin entanglement described by the first two terms. However, in general we may have a large correlation between spin and motion during gate operation, which can be affected by motional decoherence (see Sec. 7.4). Half the population stays in the initial motional state during the gate. Due to the virtual excitation of the logic mode, the rest of the population is spread over a Poissonian distribution of motional Fock states

$$\rho_{n,n} = \frac{e^{-b} b^n}{n!\, 2} \tag{5.13}$$

$$b(t) = |h(t)|^2 = 4 \left(\frac{\eta_k \Omega_{\mathrm{sb}}}{\Delta_M} \right)^2 \sin^2 \Delta_M t \tag{5.14}$$

For $p = 1$, $b(t) = \sin^2 \Delta_M t$. Even in the worst case of $p = 1$, the spin-motion entangled state never has motional spread greater than about one quantum. Hence we expect the gate to be robust under motional decoherence, as discussed in more detail in Sec. 7.3.

5.2 Experimental Results

We first implemented the entangling gate (5.1) on strings of two and four ions held in linear trap #1. In each case, we had to select a motional mode for logic that coupled equally to the ions. The obvious choice was the COM mode in each case, but because of the large heating rate of the COM mode, we selected higher-order modes in both cases. For the two-ion experiments we used the (axial) stretch mode with frequency $\sqrt{3}\,\omega_z$, while for four ions we used the (axial) stretch 2 mode with frequency $\approx \sqrt{29/5}\,\omega_z$ (see Table 2.2). In general, the only mode with equal coupling is the COM mode, so the equal coupling of the stretch 2 mode of four ions was a lucky coincidence for us.

The entangling gate required coupling on two Raman transitions. Rather than using two pairs of Raman beams to generate the two Raman difference frequencies, we modulated RR using a resonant EOM at frequency ω_{EOM} (see Sec. 4.3.2). The R2 carrier frequency ω_{R2} beat with the B1 frequency ω_{B1} to give a beatnote near the blue sideband, while one of the EOM-generated sidebands of R2 beat with B1 to give a beatnote near the red sideband. Thus we set the RR double-pass frequency to give $\omega_{\mathrm{ent}} \equiv \omega_{\mathrm{B1}} - \omega_{\mathrm{R2}} = \omega_{\downarrow\uparrow} + \omega_{\mathrm{logic}} - \Delta_M$ and the

EOM frequency to $\omega_{\mathrm{EOM}} = 2(\omega_{\mathrm{logic}} - \Delta_M)$, where ω_{logic} was the frequency of the logic mode. For two ions, we set $\omega_{\mathrm{COM}} = 5.0$ MHz, so $\omega_{\mathrm{logic}} = 8.7$ MHz. We used $\omega_{\mathrm{EOM}} = 17.67$ MHz to allow for the detuning of the entangling transition from the sidebands. For four ions, we had to reduce ω_{COM} to avoid the zigzag instability (Sec. 2.1.3). We chose $\omega_{\mathrm{COM}} = 3.6$ MHz, so that $\omega_{\mathrm{logic}} = 8.7$ MHz again and we could use the same EOM frequency.

To ensure equal illumination of each ion, we used beam spot sizes at least twice as large as the extent of the ion crystal. As shown in Sec. 7.3, deviations from this condition affect the gate fidelity only to second order. To observe loss of fidelity due to unequal illumination, we had to offset the beams by an amount much larger than the estimated fluctuations in beam pointing, so we expect this source of error to be small.

To provide equal coupling to each sideband, we set the EOM power so that the intensities of the EOM sidebands were equal to the intensity of the (depleted) R2 carrier. In this setup, only the EOM carrier and one EOM sideband were useful for driving the entangling gate. The rest of the R2 power, which amounted to about half the R2 power before the EOM, contributed to the spontaneous emission rate (see Sec. 7.2.2) but was wasted for purposes of quantum logic. Flopping at $\omega_{\mathrm{B1}} - \omega_{\mathrm{R2}} = \omega_{\downarrow\uparrow} + \omega_{\mathrm{logic}}$ with the EOM on gave the π-pulse time of the blue sideband as driven by the EOM carrier, while flopping at $\omega_{\mathrm{B1}} - \omega_{\mathrm{R2}} = \omega_{\downarrow\uparrow} + \omega_{\mathrm{logic}} + 2\Delta_M$ gave the π-pulse time of the red sideband as driven by the red EOM sideband. Adjusting the EOM power so that these times were equal ensured the desired condition. For cold ions, the red sideband signal was small, so we sometimes flipped the ion spins with a carrier π-pulse before taking the second flopping curve. To observe loss of fidelity from unequal sideband coupling, we had to change the EOM power by about a factor of 3 from the optimum, so we expect this source of error to be small as well.

Since we operated the gate in the nonperturbative regime, the behavior of the ions under the entangling drive depended strongly on Δ_M. Typically we set $\omega_{\rm dp}$ to detune the Raman drives symmetrically from their sidebands and tuned Δ_M by changing the trap endcap voltage, preserving the symmetric detuning. We obtained flopping curves for various values of Δ_M. Fig. 5.2 shows experimental (dots) and theoretical (solid) curves for two ions. Here Δ_M satisfies Eq. (6.3) for $p = 1$, and the theoretical fluorescence is $A(2\rho_{\downarrow\downarrow,\downarrow\downarrow} + \rho_{\downarrow\uparrow,\downarrow\uparrow} + \rho_{\uparrow\downarrow,\uparrow\downarrow})$ from Eq. (5.6) with A a scaling factor. We multiply the theory curve by an exponential decay with time constant $\sim 30\,\mu$s to account for decoherence during the gate.

Fig. 5.3 shows theoretical flopping curves at $p > 1$ for the conditions of Fig. 5.2. Here we parametrize Δ_M in terms of Eq. (6.3) by allowing noninteger p. The curves exhibit a slow oscillation, corresponding to the spin evolution under the first term of Eq. (5.6), with superimposed faster oscillations arising from the last two terms of Eq. (5.6). In Fig. 5.3(a) Δ_M satisfies Eq. (6.3) with $p = 2$, so the frequency of the fast oscillation is 4 times that of the slow oscillation. In contrast, Fig. 5.2(b) shows a flopping curve for which $p = 1.6$, so Δ_M does not satisfy Eq. (6.3). The shape of this curve is significantly deformed from those of Figs. 5.2 and 5.3(a). The flopping curves for four ions at a given value of p were similar to those for two ions.

To operate the entangling gate at $p = 1$, we tuned Δ_M so that the frequency of the fast oscillation was twice that of the slow oscillation, giving a reasonable approximation to Fig. 5.2. We then took a flopping curve, fixed the pulse duration at the point of minimum fluorescence, corresponding to $k(t) \approx \pi$, and varied the endcap voltage (tuning Δ_M) to reduce the fluorescence further. Repeating this last step once or twice was usually sufficient to optimize Δ_M. Reducing the pulse duration by half, we had $k(t) \approx \pi/2$, producing the evolution (5.1).

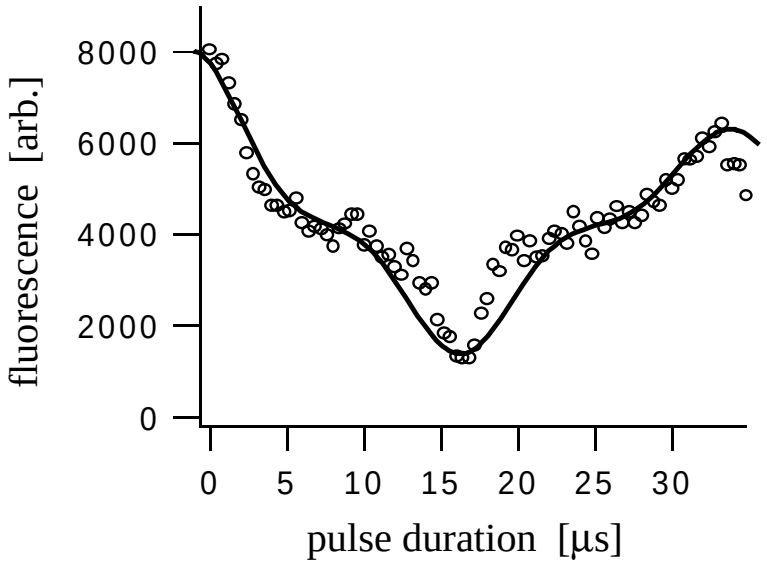

Figure 5.2: Experimental flopping curve for $p = 1$ (dots) with theoretical prediction (line) with exponential decay of time constant $\sim 30\mu$s and with ions in the motional ground state.

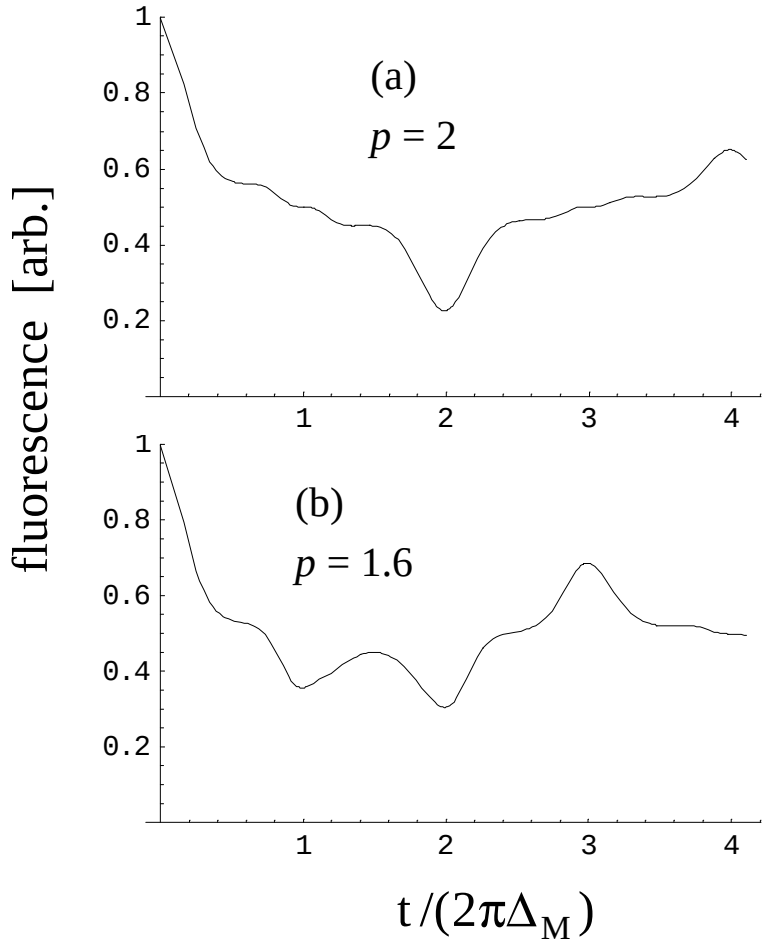

Figure 5.3: Theoretical flopping curves for (a) $p = 2$ and (b) $p = 1.6$, calculated for the same conditions as in Fig. 5.2. The value of p dramatically affects the shape of the flopping curve.

We obtained lineshapes at fixed values of Δ_M by sweeping $\omega_{\rm dp}$. The linewidth of the entangling transition was a few tens of kHz and decreased with increasing Δ_M. Because the R2 power was divided among the sidebands by the EOM, the usable R2 power in either of the Raman drives was about 1/4 the total R2 power, decreasing the Rabi frequency. The small linewidth made the entangling gate especially sensitive to perturbations of $\omega_{\downarrow\uparrow}$, as detailed in Sec. 7.3.

The spin population of the states produced by the evolution (5.1) is nominally equally divided between $|\downarrow^{\rm N}\rangle$ and $|\uparrow^{\rm N}\rangle$ for N ions. Fig. 5.4 shows a histogram of count rates obtained after application of the entangling gate. As expected, the histogram shows a bimodal distribution of count rate. Fitting the populations for this histogram gave probabilities $P_0 = 0.43$, $P_1 = 0.11$, $P_2 = 0.46$, where P_n is the probability to find n ions in $|\downarrow\rangle$. The error in each value is ± 0.01. The populations are quite close to the ideal case $P_0 = 0.50$, $P_1 = 0.00$, $P_2 = 0.50$. For four ions we typically found $P_0 \approx 0.35$, $P_1 \approx P_2 \approx P_3 \approx 0.10$, $P_4 \approx 0.35$. This distribution implies that quite a bit of the population resides outside the desired state. However, there are 14 orthogonal states that give one, two, or three ions in $|\downarrow\rangle$, and only two orthogonal states in the desired entangled state, so the distribution of population over the 16 orthogonal states is far from random.

Ideally, the evolution (5.1) produces full coherence between the $|\downarrow^{\rm N}\rangle$ and $|\uparrow^{\rm N}\rangle$ states, so that $|\rho_{\downarrow^{\rm N},\uparrow^{\rm N}}| = 0.5$. To measure the coherence produced in the experiment, we "interfered" the $|\downarrow^{\rm N}\rangle$ and $|\uparrow^{\rm N}\rangle$ states using a variant of the method proposed in [67]. After the entangling gate, we applied a carrier $\pi/2$ pulse (Eq. 3.26) with Raman phases $\phi_j = \phi$ for all j. Here we have taken the phases $\phi_j = 0$ for the entangling pulse. We then detected the number $N_\downarrow$ of ions in

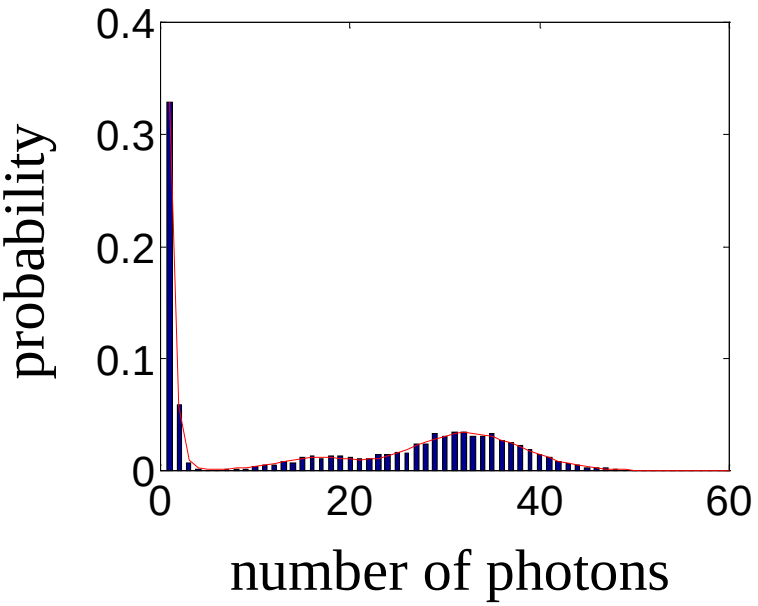

Figure 5.4: Histogram of photon counts obtained after application of the entangling gate.

$|\downarrow\rangle$ and compute the parity $\Pi(\phi) \equiv (-1)^{N_\downarrow}$. Assuming an ideal carrier pulse, we have

$$\Pi(\phi) = 2|\rho_{\downarrow^N,\uparrow^N}| \cos N\phi \tag{5.15}$$

so we could extract the desired coherence by measuring the parity as a function of phase. To observe the parity fringes of Eq. (5.15), we had to set the synthesizer frequency for the $\pi/2$ pulse to $\omega_{\rm ent} - \omega_{\rm EOM}/2$ (in Hz) with accuracy better than ± 1 Hz. This condition ensured that the beat frequency for the $\pi/2$ pulse was exactly midway between the two beat frequencies used for the entangling transition, so that the entangling pulse and the $\pi/2$ pulse were mutually coherent. Any error in setting the frequency of the $\pi/2$ pulse caused phase slippage of ϕ, reducing the contrast of the parity fringes.

To obtain the interference data, we took histograms of the photon counts at each value of the phase ϕ over several oscillations of the sinusoid Eq. (5.15). Averaging all the histograms together and fitting the result determined the mean count number per ion and the mean number of background counts. From this information and our knowledge of the repumping parameter α_p (Eq. 3.1) we constructed reference histograms for $N_\downarrow = 0, 1, \ldots N$. Fitting the individual histograms to the references gave the probabilities $P_n(\phi)$ to find $N_\downarrow = n$ at phase ϕ, from which we could trivially infer $\Pi(\phi)$. Fig. 5.5 shows results of interference experiments for two and four ions. Each curve is fit with a single sinusoid with frequency fixed by Eq. (5.15) to obtain the amplitude. The presence of other oscillation frequencies in the interference data would imply coherences involving less than N ions. Since the fits to the data are good, we infer that $\rho_{\downarrow^N,\uparrow^N}$ is by far the largest off-diagonal element of the density matrix in each case.[1] The data of Fig 5.5 show $|\rho_{\downarrow^N,\uparrow^N}| = 0.39 \pm 0.01$ for two ions and 0.22 ± 0.02 for four ions. Though these values are significantly less than the ideal value of 0.50, we will see that the experimental states are still

[1] In principle, other coherences could be present, but the interference data would constrain these coherences to have particular phase relationships that seem physically unlikely.

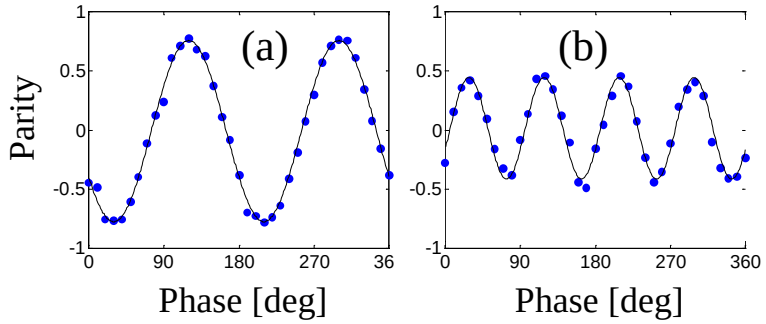

Figure 5.5: Interference data for (a) two and (b) four ions. Dots are data points, solid lines are sinusoidal fits with frequencies fixed by Eq. (5.15). The fit amplitudes show $|\rho_{\downarrow^{\mathrm{N}},\uparrow^{\mathrm{N}}}| = 0.39 \pm 0.01$ for two ions and 0.22 ± 0.02 for four ions.

entangled.

We can easily establish the separability or entanglement of the experimental density matrix $\boldsymbol{\rho}$ by computing its fidelity $F = \langle\psi_{\mathrm{ent}}|\boldsymbol{\rho}|\psi_{\mathrm{ent}}\rangle$ against the ideal state $\psi_{\mathrm{ent}} = (|\downarrow^{\mathrm{N}}\rangle + |\uparrow^{\mathrm{N}}\rangle)/\sqrt{2}$. To show this, consider a general register state $|\psi_F\rangle$ that is factorizable by dividing the register into two subsets X and Y. We can then write [64]

$$|\psi_F\rangle = (a|\uparrow\ldots\uparrow\rangle + b|\downarrow\ldots\downarrow\rangle + \ldots)_X \otimes (c|\uparrow\ldots\uparrow\rangle + d|\downarrow\ldots\downarrow\rangle + \ldots)_Y \tag{5.16}$$

where $|\uparrow\ldots\uparrow\rangle_X$ has all spins in X in the state $|\uparrow\rangle$. Normalization of the states over X and Y requires $|a|^2 + |b|^2 \leq 1$, $|c|^2 + |d|^2 \leq 1$, so we have

$$2(|ac| + |bd|) \leq (|a| - |c|)^2 + (|b| - |d|)^2 + 2(|ac| + |bd|) \tag{5.17}$$

$$= |a|^2 + |b|^2 + |c|^2 + |d|^2 \leq 2 \tag{5.18}$$

Writing $\rho^F = |\psi_F\rangle\langle\psi_F|$ and making identifications $\rho^F_{\uparrow^{\mathrm{N}},\uparrow^{\mathrm{N}}} = |ac|^2$, etc., we find

$$(|ac| + |bd|)^2 = \rho^F_{\downarrow^{\mathrm{N}},\downarrow^{\mathrm{N}}} + \rho^F_{\uparrow^{\mathrm{N}},\uparrow^{\mathrm{N}}} + 2|\rho^F_{\downarrow^{\mathrm{N}},\uparrow^{\mathrm{N}}}| = 2\langle\psi_{\mathrm{ent}}|\rho^F|\psi_{\mathrm{ent}}\rangle \leq 1 \tag{5.19}$$

which holds for any factorizable, i.e., non-entangled state. If the density matrix ρ is factorizable over X,Y, we can write it as a sum of pure states factorizable over X,Y. Hence any factorizable density matrix satisfies $F = \langle\psi_{\rm ent}|\boldsymbol{\rho}|\psi_{\rm ent}\rangle \leq 1/2$. This condition is sufficient but not necessary to show entanglement [68]. By measuring the populations $\rho_{\downarrow^N,\downarrow^N}$, $\rho_{\uparrow^N,\uparrow^N}$ and the coherence $|\rho_{\downarrow^N,\uparrow^N}|$, we established [64]

$$F = 0.83 \pm 0.01 \qquad N = 2 \tag{5.20}$$

$$F = 0.57 \pm 0.02 \qquad N = 4 \tag{5.21}$$

showing that the entangling gate can indeed produce entangled states of two and four ions.

For the two-qubit state, we can approximate the entanglement of formation from the measured density matrix elements as $E \approx 0.5$ [69]. This quantity measures the increase in the entropy of one qubit produced by tracing over the other qubit. Ideally, tracing over one qubit leaves the other in a mixture of half $|\downarrow\rangle$ and half $|\uparrow\rangle$, with no coherence remaining between $|\downarrow\rangle$ and $|\uparrow\rangle$. In this case $E = 1$. The entanglement of formation also gives an upper bound on the entanglement of distillation E_D [70, 71]. Leaving out the technical details, any procedure designed to distill a perfect EPR state $|\downarrow\uparrow\rangle - |\uparrow\downarrow\rangle$ from several copies of a partially entangled two-qubit state requires an average of $1/E_D$ copies [72]. The complexity of quantum communications tasks is often quantified in terms of the number of EPR states required, so E_D measures the usefulness of the experimental state ρ. We see that order of two copies of our two-qubit state ρ are required to distill one EPR state.

There is so far no simple way to characterize the amount of entanglement of a general four-qubit state. However, the absence of coherences other than $\rho_{\downarrow^4,\uparrow^4}$ in the interference data

suggests that we can write the experimental four-ion density matrix as [64]

$$\boldsymbol{\rho} \approx 0.43|\psi_{\rm ent}\rangle\langle\psi_{\rm ent}| + 0.57\rho_{\rm diag} \tag{5.22}$$

where $\rho_{\rm diag}$ has no off-diagonal elements. Thus, not only is the total density matrix entangled, but any one shot of the experiment has a significant chance of producing the desired state.

The high fidelity of the two-ion entangled state encouraged us to use the evolution (5.6) with $p = 1$ and $k(t) = \pi/2$ as our basic two-qubit gate. The experiments of chapters 7 and 8 used precisely this gate for simple quantum logic. Reinstating the phases ϕ_j, we can write the normalized gate operator as

$$\mathbf{U}_{\rm ent}(\phi_1, \phi_2) = \exp[i\pi \mathbf{J}_y^2/2] \tag{5.23}$$

$$\rightarrow \frac{1+i}{2}\left[\mathbf{1} - i\left(e^{i(\phi_1+\phi_2)}|\uparrow\uparrow\rangle\langle\downarrow\downarrow| + e^{-i(\phi_1+\phi_2)}|\downarrow\downarrow\rangle\langle\uparrow\uparrow| \right.\right. \tag{5.24}$$

$$\left.\left. -e^{i(\phi_1-\phi_2)}|\uparrow\downarrow\rangle\langle\downarrow\uparrow| - e^{-i(\phi_1-\phi_2)}|\downarrow\uparrow\rangle\langle\uparrow\downarrow|\right)\right] \tag{5.25}$$

In the following, we describe our two-ion logic circuits as products involving $\mathbf{U}_{\rm ent}(\phi_1, \phi_2)$ and the normalized carrier evolution

$$\mathbf{U}_{\rm car}(\theta, \phi_1, \phi_2) = \bigotimes_{j=1,2}\left[\mathbf{1}\cdot\cos\frac{\theta}{2} - i\sin\frac{\theta}{2}\,(e^{i\phi_j}|\uparrow\rangle\langle\downarrow| + e^{-i\phi_j}|\downarrow\rangle\langle\uparrow|)\right] \tag{5.26}$$

produced by driving the carrier (Eq. 3.26) on resonance for a time $t = \theta/\Omega_R$.

Chapter 6

Applications of Entanglement

6.1 Violation of a Bell Inequality

Perhaps the most striking feature of quantum mechanics is its denial of local realism. The uncertainty principle requires us to believe that measuring the position of an object can change its momentum, but is still consistent with the basic notion of realism: that the object had some position or other before the measurement, which is then perturbed by the act of measurement. At the same time, special relativity insists on locality: the measured position does not depend on events outside the light-cone of the object. As shown by Einstein, Podolsky, and Rosen [73], quantum mechanics is incomplete if we assume local realism. Bell [74] proved that quantum mechanics is actually inconsistent with local realism, deriving an inequality on observables that is satisfied by all local realistic theories but is violated by quantum mechanics. Many experiments [75, 76, 77, 78, 79, 80] have observed violation of a Bell inequality, so that local realistic theories are now discounted by the vast majority of physicists. The result of this reasoning is epistemologically remarkable. One must either accept that "objective reality" is created only at the moment of measurement, or give up special relativity! Mainstream physics has opted to retain special relativity, probably a good choice in view of the massive experimental evidence in favor of quantum field theory. Moreover, the philosophical tradition of Mach and, later, Heisenberg and Bohr, restricts the domain of physics to properties susceptible to measurement, so one can dispense with realism in a Machian theory. The alternative view of Bohm [81, 82] retains

realism at the expense of locality, introducing a "pilot-wave" field that coordinates the behavior of particles at widely separated points.

Clauser, Horne, Shimony, and Holt (CHSH) [83] proposed an experimental arrangement to test a form of Bell's inequality quantitatively. Here a "black box" prepares a pair of particles. The ith particle ($i = 1, 2$) enters a measurement apparatus whose properties are parametrized by an independent classical variable Φ_i. Each (classical) measurement yields a value $M_i(\Phi_i) = \pm 1$ depending on the parameter Φ_i and the state of the correlated particles. Averaging over many measurements, one extracts the correlation function $q(\Phi_1, \Phi_2) = \langle M_1(\Phi_1) M_2(\Phi_2) \rangle$. Then the CHSH form of the Bell inequality

$$\begin{aligned} B(\alpha_1, \delta_1, \beta_2, \gamma_2) &\equiv |q(\delta_1, \gamma_2) - q(\alpha_1, \gamma_2)| + |q(\delta_1, \beta_2) + q(\alpha_1, \beta_2)| \\ &\leq 2 \end{aligned} \tag{6.1}$$

holds for any values α_1, δ_1 (resp. β_2, γ_2) of Φ_1 (resp. Φ_2) under the assumption of local realism [83]. The derivation of Eq. (6.1) involves the quantity $\langle M_1(\alpha_1) M_1(\delta_1) M_2(\beta_2) M_2(\gamma_2) \rangle$. Since the terms $M_1(\alpha_1)$, $M_1(\delta_1)$ refer to different arrangements of the experiment for $\alpha_1 \neq \delta_1$, quantum mechanics forbids us to speak of both terms at once. Hence the product $M_1(\alpha_1) M_1(\delta_1)$ is not well-defined in quantum mechanics, allowing violation of Eq. (6.1).

In our experiment, the entangling gate played the role of the CHSH "black box", preparing two ions in the state $|\downarrow\downarrow\rangle + |\uparrow\uparrow\rangle$. To measure the correlation function $q(\Phi_1, \Phi_2)$, we applied a carrier rotation $\mathbf{U}_{\text{car}}(\theta = \pi/2, \Phi_1, \Phi_2)$ and built up a histogram of photon counts. Counting the number of events N_0 (N_1, N_2) with zero (one, two) ions bright, we find

$$q(\Phi_1, \Phi_2) = \frac{(N_0 + N_2) - N_1}{N_{\rm tot}} \tag{6.2}$$

To measure $B(\alpha_1, \delta_1, \beta_2, \gamma_2)$, we obtained a value of q for each term in Eq. (6.1). We chose α_1, etc., so as to give the maximum violation of Eq. (6.1) by the quantum-mechanical prediction for B, which occurs for

$$\begin{aligned} \alpha_1 &= -\pi/8 \qquad \delta_1 = 3\pi/8 \\ \beta_2 &= -\pi/8 \qquad \gamma_2 = 3\pi/8 \end{aligned} \tag{6.3}$$

For these angles we have the prediction $B = 2\sqrt{2}$, contradicting the bound (6.1) set by local realism.

Independently setting Φ_1 and Φ_2 for the carrier rotation required positioning each of the two ions at a specific point in the interference pattern of the Raman beams (modulo the wavelength of the interference pattern). Changing the phase of the RF driving the RR double-pass AOM shifted the interference pattern by a constant amount, allowing us to control the quantity $\phi_{\rm tot} = \phi_1 + \phi_2$. However, the phase difference $\Delta\phi = \phi_1 - \phi_2$ is set by the separation of the ions Δz along $\hat{z}$ as $\Delta\phi = \sqrt{2}k\Delta z$. To control $\Delta\phi$ without changing $\phi_{\rm tot}$, we varied the endcap voltage, and therefore the trap strength, so that the ions moved symmetrically about the center of the trap. Hence the endcap voltage and the RF phase jointly determined the phases Φ_1, Φ_2.

We repeated the experiment $N_{\rm tot} = 20\ 000$ times for each of the four sets of phases given by Eq. (6.3). These data are presented as histograms in Fig. 6.1. Shelving the $|\uparrow\rangle$ state (see below) allowed us to extend the duration of the detection pulse to 1 ms, increasing the number of photons detected from each bright ion and reducing the error due to photon shot noise. To

Table 6.1: The correlation values and resulting Bell's signals for five runs of the experiment. The phase angles $\alpha_1, \delta_1, \beta_2, \gamma_2$ are given by Eq. (6.3). The statistical errors are 0.006 and 0.012 for the values of q and B respectively.

$q(\alpha_1, \beta_2)$	$q(\alpha_1, \gamma_2)$	$q(\delta_1, \beta_2)$	$q(\delta_1, \gamma_2)$	$B(\alpha_1, \delta_1, \beta_2, \gamma_2)$
0.541	0.539	0.569	-0.573	2.222
0.575	0.570	0.530	-0.600	2.275
0.551	0.634	0.590	-0.487	2.262
0.575	0.561	0.559	-0.551	2.246
0.541	0.596	0.537	-0.571	2.245

determine the values N_0, N_1, N_2 entering Eq. (6.2), we divided the histograms into cases of zero, one, or two ions bright by setting discriminators at the positions of the arrows in Fig. 6.1. This procedure gives the same value of q that we would obtain by measuring M_1, M_2 individually for each shot of the experiment.

We measured the Bell signal five times to estimate the variation between runs. The five sets of correlation functions and the resulting Bell signals are shown in Table 6.1. The statistical error of each Bell signal was ± 0.01. Averaging the Bell signals together, we find

$$B(-\frac{\pi}{8}, \frac{3\pi}{8}, -\frac{\pi}{8}, \frac{3\pi}{8}) = 2.25 \pm 0.03 \tag{6.4}$$

an 8σ violation of the Bell inequality (6.1).

The error in the average Bell signal significantly exceeds the statistical error predicted from Table 6.1. We attribute this discrepancy to drifts of the RF phase between the HP 8660 synthesizer used to drive the entangling gate and the HP 3335 used for the carrier rotation. Such drifts induce errors in setting the angles α_1, etc., for the four measurements of q, but these errors cannot be estimated from the statistical errors in q. The phase drift was usually constant

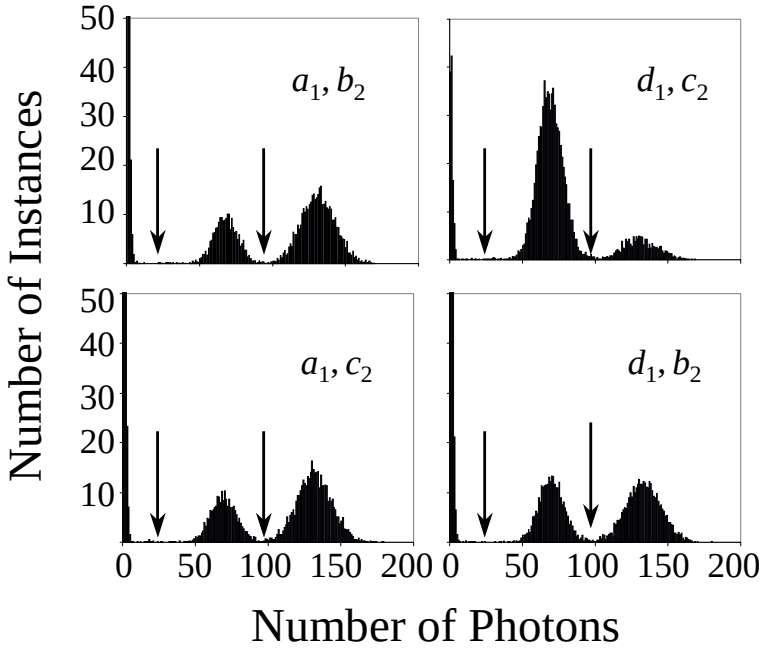

Figure 6.1: Histograms of fluorescence signals for the four sets of phases given in Eq. (6.3). The vertical arrows break up the data into cases of zero, one, or two ions bright with 98% accuracy.

for a few minutes at a time, but could change magnitude and direction rapidly and randomly. The drift sometimes amounted to several tens of mrad per minute, while about 15 minutes were required to make the four measurements of q needed for one measurement of B. Including the drift in the error analysis for each measurement of B approximately accounts for the statistical error in the average value of B.

In this experiment, we attempted to falsify local realism by assuming local realism and arriving at a contradiction, namely $B = 2\sqrt{2} \leq 2$. But Φ_1, Φ_2 were hard to measure directly, since they varied rapidly if an ion moves even a few nm. To ensure the logical consistency of our procedure, we calibrated ϕ_{tot} and $\Delta\phi$ in terms of macroscopic quantities by using purely classical reasoning. The RF phase, a macroscopic quantity, directly set ϕ_{tot} by controlling the (classical) interference pattern of the Raman beams. The endcap voltage, another macroscopic quantity, set $\Delta\phi$ indirectly by changing the ion separation. To calibrate $\Delta\phi$, we first observed that applying a pair of pulses with fixed duration and relative phase ϕ to a single ion caused the ion fluorescence to vary as $C + A\cos\phi$. Here we set ϕ using the (classical) RF phase, and the pulse duration and frequency were set to maximize A. (In quantum-mechanical terms, the pulse duration gave a $\pi/2$ rotation of the ion, but our procedure does not rely on this fact.) We deduced that applying similar pulses to two ions would produce fluorescence

$$C + A\cos\phi_1 + C + A\cos\phi_2 = 2C + 2A\cos\frac{\phi_{\text{tot}}}{2}\cos\frac{\Delta\phi}{2} \tag{6.5}$$

since the detector is linear. Applying the pulses and using the RF phase to sweep ϕ_{tot} at a fixed endcap voltage produced a sinusoidal signal of amplitude $2A\cos(\Delta\phi/2)$. Repeating the experiment for a range of endcap voltages and fitting the amplitudes allowed us to extract $\Delta\phi$ as a function of endcap voltage. Since the phase of the sinusoidal signal did not change as a function of endcap voltage, we could be sure that ϕ_{tot} depended only on the RF phase. Hence the phases Φ_1, Φ_2 were completely determined by the classical parameters of RF phase and

endcap voltage.

Up to now, all experiments showing violation of Bell's inequality have had quite low detector efficiencies, so that the number of particle pairs produced by the "black box" far exceeded the number of events used for calculating the correlation function. To interpret these experiments as ruling out local realism, one assumes that the correlated pairs that are not detected exhibit the same behavior as those that are detected, the fair sampling hypothesis. However, by violating this assumption it is possible to construct local realistic theories that reproduce the experimental data for detector efficiencies below a critical value, the so-called detection loophole [84, 85]. In these theories, the full set of particle pairs satisfies Bell's inequality, but the subset of pairs that is actually detected appears to violate it. While such a conspiracy of detectors seems quite unlikely, no previous experiment has been able to rule it out.

The experiment described here was the first to demonstrate a violation of Bell's inequality without use of the fair sampling hypothesis. Because we could prepare the entangled state on demand, we could make a measurement on every correlated pair. Thus there was no sampling involved in our experiment at all. In this situation, quantum mechanics predicts that uncorrelated errors in measuring the two particles simply lower the value of B. We estimate that we would have observed $B = 2.37$ in the absence of detection errors.

The overlap of the histograms in Fig. 6.1 produced a detection error rate of 2% in discriminating between the cases of zero, one, and two ions bright. Detection error in our experiments frequently arises from off-resonant repumping of the $|\uparrow\rangle$ state to $|\downarrow\rangle$ (see Sec. 3.2). This repumping can occur even if the $|\uparrow\rangle$ ion scatters only one BD photon. However, atomic selection rules

ensure that an ion initially in the $^2S_{1/2}\,|F=1,m_F=1\rangle$ state must scatter at least three BD photons to arrive at $|\downarrow\rangle$. The repumping rate from $^2S_{1/2}\,|F=1,m_F=1\rangle$ to $|\downarrow\rangle$ is therefore lower than that from $|\uparrow\rangle$ to $|\downarrow\rangle$. We took advantage of this fact to reduce our detection error. After the carrier rotation, but before detection, we used two Raman $\pi-$pulses to transfer the population in $|\uparrow\rangle$ to $^2S_{1/2}\,|F=2,m_F=0\rangle$ and thence to $^2S_{1/2}\,|F=1,m_F=1\rangle$. We implemented this "shelving" sequence with the copropagating beams B1, R1. The Zeeman splitting between the shelving transitions exceeded the bandwidth of the RR double-pass AOM, so we used the shelving EOM (see Sec. 4.3.2) to access the shelving transition frequencies.

To falsify local realism using Bell's inequality, one must ensure that the only correlations between $M_1(\Phi_1)$ and $M_2(\Phi_2)$ arise from the correlations of the entangled pair. However, if the measuring devices can communicate during the measurement, i.e., if the measurement processes lie within each others' lightcones, we can attribute any violation of Bell's inequality to a conspiracy between the measuring devices rather than to any violation of local realism by the entangled particles. Tests of Bell's inequality using photons have gone to great lengths to close this "locality loophole" [78, 79, 80]. In our experiment we could not ensure nonlocality because of the small separation between the ions. However, there is no physical reason to believe that the measurement outcomes influence each other in this way. We estimated the size of correlations arising from a wide variety of effects, including dipole-dipole interactions between the ions, interference between the radiation patterns of the ions, etc. [86, 87] In all cases the spurious correlations are negligible, but strictly speaking we have not closed the locality loophole. Similarly, the photon experiments [78, 79, 80] do not close the detection loophole, though there is no physical reason to believe in a conspiracy between detectors. In this sense our experiment is complementary to the photon experiments.

This experiment gives the first violation of the Bell inequality for massive particles obtained using a complete set of correlation measurements. A previous experiment using protons [76] deduced a violation from an incomplete set of measurements using quantum-mechanical assumptions. Furthermore, our data uses the outcome of every shot of the experiment, so the violation is obtained without the use of the fair-sampling hypothesis, closing the detector loophole for the first time. However, the "locality loophole" remains open for our data. Since the detection events on the two ions occur within each other's lightcones, in principle the detections could influence each other, leading to spurious correlations.

6.2 Interferometry below the Standard Quantum Limit

6.2.1 N Views of Ramsey Spectroscopy

Frequency measurements using atomic clocks are currently the most accurate measurements of any physical quantity [88, 89, 90]. These clocks measure the transition frequency between two electronic levels $|\downarrow\rangle$, $|\uparrow\rangle$ of an atomic sample to derive a stable reference for a local oscillator (LO). The LO usually interrogates the transition by Ramsey spectroscopy [91]. The simplest variant of this method consists of three steps: (1) the LO applies a $\pi/2$ rotation to the atoms, (2) the atoms undergo free evolution for a time T_R, and (3) the LO again applies a $\pi/2$ rotation. In the frame rotating at the LO frequency, the free evolution (step 2) causes the part of the atomic state in $|\uparrow\rangle$ to acquire a phase $T_R\omega_R$ relative to the part of the state in $|\downarrow\rangle$. Here ω_R is the difference between the LO and the atomic frequencies. After step 3, the average value of the collective spin operator $\mathbf{J}_z$ on N atoms is

$$\langle \mathbf{J}_z \rangle = N(1 - \cos T_R\omega_R)/2 \tag{6.6}$$

so that we can measure the frequency difference ω_R by measuring the electronic state of the

atoms.

While Ramsey spectroscopy is traditionally described as a measurement of the frequency ω_R, this frequency can fluctuate during the interval T_R. In this case we find the Ramsey signal

$$\langle \mathbf{J}_z \rangle = N(1 - \cos\phi_R)/2 \tag{6.7}$$

$$\phi_R \equiv \int_0^{T_R} \omega_R(t')\, dt' \tag{6.8}$$

so we see that the signal really measures the accumulated relative phase ϕ_R between the $|\downarrow\rangle$ and $|\uparrow\rangle$ states, in the same way that an optical interferometer measures the relative phase between two optical paths. Now representing the atomic spin state on the Bloch sphere, we see that the relative phase is just the azimuthal angle of the spin vector [92, 36], so that Ramsey spectroscopy measures the rotation angle of the spin vector around the $\hat{z}$ axis. Using the Schwinger spin representation for the two modes of an optical interferometer [93], we see that optical path lengths correspond to rotations about the $\hat{z}$ axis, while 50/50 beamsplitters are equivalent to $\pi/2$ pulses [94]. Performing Ramsey spectroscopy is equivalent to operating a Mach-Zehnder interferometer [95] with Fock-state input to one port, as shown graphically in Fig. 6.2.

While Ramsey spectroscopy measures only the rotation angle ϕ_R about the $\hat{z}$ axis, we can use atomic spin operators more generally to characterize an arbitrary rotation of our coordinate system by an angle ζ about an axis $\hat{u}$, as depicted in Fig. 6.3. Such a rotation implements the operator

$$\mathbf{R}(\hat{u}, \zeta) = \exp\Big[-i\zeta\vec{\mathbf{J}} \cdot \hat{u} \Big] \tag{6.9}$$

on the atomic spin system. Since the state of the atomic system $|\Psi(\zeta)\rangle$ after the rotation depends

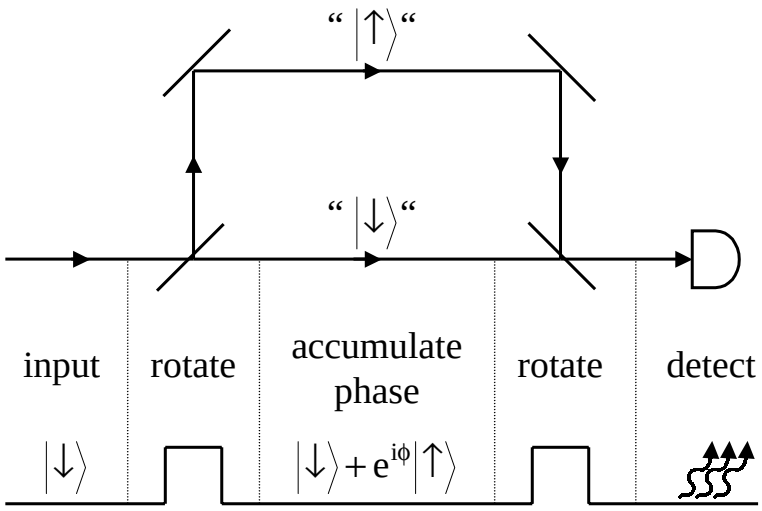

Figure 6.2: Equivalence of Ramsey spectroscopy and Mach-Zehnder interferometry. In the Schwinger representation of the optical modes, 50/50 beamsplitters are $\pi/2$ rotations, while free propagation produces rotations about $\hat{z}$.

on the classical parameter ζ, we can try to estimate ζ by measuring an atomic observable $\boldsymbol{\mathcal{O}}$. We define the expectation value of $\boldsymbol{\mathcal{O}}$ over the state $|\Psi(\zeta)\rangle$ as

$$\langle \boldsymbol{\mathcal{O}} \rangle_\zeta = \langle \Psi(\zeta) | \boldsymbol{\mathcal{O}} | \Psi(\zeta) \rangle \tag{6.10}$$

Then if a measurement of the operator $\boldsymbol{\mathcal{O}}$ yields the result $\mathcal{O}$, we find the estimated value $\overline{\zeta}$ by inverting the equation $\langle \boldsymbol{\mathcal{O}} \rangle_{\overline{\zeta}} = \mathcal{O}$. The uncertainty of the estimate $\delta\zeta$ (measured in radians) is

$$\delta\zeta = \frac{\Delta \boldsymbol{\mathcal{O}}}{|\partial \langle \boldsymbol{\mathcal{O}} \rangle_\zeta / \partial \zeta|} \tag{6.11}$$

where $(\Delta \boldsymbol{\mathcal{O}})^2$ gives the variance in repeated measurements of $\boldsymbol{\mathcal{O}}$. We assume that the measurement has negligible technical noise, so

$$(\Delta \boldsymbol{\mathcal{O}})^2 \equiv \langle \boldsymbol{\mathcal{O}}^2 \rangle_{\overline{\zeta}} - \langle \boldsymbol{\mathcal{O}} \rangle_{\overline{\zeta}}^2 \tag{6.12}$$

Substituting Eq. (6.12) into Eq. (6.11) gives the quantum-limited uncertainty for an estimate of ζ by a single measurement.

Ramsey spectroscopy and Mach-Zehnder interferometry both detect a relative phase ϕ_R by measuring the observable $\mathbf{J}_z$ on the family of states

$$|\Psi(\phi_R)\rangle = \bigotimes_{i=1}^{N} (\cos\phi_R \, |\downarrow\rangle + \sin\phi_R \, |\uparrow\rangle) \tag{6.13}$$

produced by the final $\pi/2$ pulse (or beamsplitter). In both cases, the finite number N of particles (atoms or photons) involved in the measurement leads to the shot-noise limit for measurements of ϕ [96]

$$\delta\phi_{\mathrm{SQL}} = \frac{\Delta \mathbf{J}_z}{|\partial \langle \mathbf{J}_z \rangle / \partial \phi|} = \frac{1}{\sqrt{N}} \tag{6.14}$$

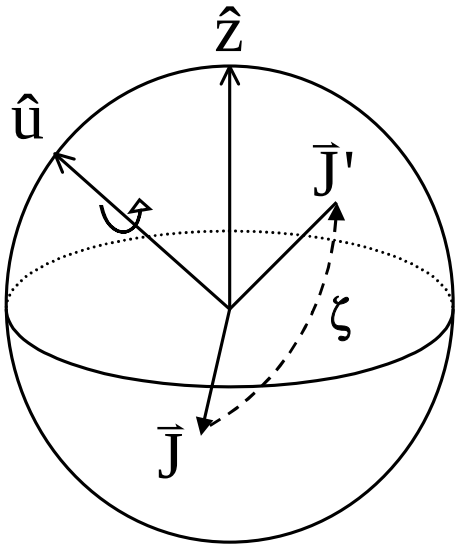

Figure 6.3: Estimating rotation angles on the Bloch sphere. Rotation of the coordinate system is equivalent to rotation of the atomic spin vector.

The limit (6.14) readily generalizes to estimation of an arbitrary rotation angle ζ by any family of states $|\Psi(\zeta)\rangle$ that satisfy

$$|\Psi(\zeta)\rangle = \bigotimes_{i=1}^{N}(a_i(\zeta)|\downarrow\rangle + b_i(\zeta)|\uparrow\rangle) \tag{6.15}$$

in the spin representation. The separability condition (6.15) forbids nonclassical correlations between individual atoms in a spectroscopic sample or between individual photons passing through an interferometer. Since only classical correlations are present in standard spectroscopy or standard interferometry, Eq. (6.14) is usually called the "standard quantum limit" (SQL). This fundamental noise source limits the stability of some atomic clocks [96, 97].

The separable states that achieve $\delta\zeta = 1/\sqrt{N}$ for a given axis $\hat{u}$ are the coherent spin states (CSS) [98], which are obtained from $|\downarrow\rangle^N$ by applying a rotation such that $\langle\vec{\mathbf{J}}\rangle_{\rm CSS}$ lies in the plane perpendicular to $\hat{u}$. After the rotation by ζ, we measure the observable $\mathbf{J}_\perp \equiv \vec{\mathbf{J}}\cdot\hat{n}_\perp$, where $\hat{n}_\perp$ is perpendicular to both $\hat{u}$ and the final CSS spin vector $\langle\vec{\mathbf{J}}\rangle$. Then Eq. (6.11) gives the SQL for general rotation angle estimation

$$\delta\zeta_{\rm SQL} = \frac{\Delta\mathbf{J}_\perp}{|\langle\vec{\mathbf{J}}\rangle|} = \frac{1}{\sqrt{N}} \tag{6.16}$$

6.2.2 Interferometry with Entangled States

States that exhibit quantum correlations allow estimates of ζ with smaller uncertainty than the SQL [94, 99, 100, 101, 102, 103, 104, 67, 9, 105, 106, 107, 108, 109]. Such sub-shot-noise (SSN) interferometry was first demonstrated using squeezed light [100, 101] and later, using pairs of entangled photons [105]. Recently Orzel et al. [108] have claimed reduction of the atom number variance in a collection of Bose-Einstein condensates, a step toward realizing SSN interferometry with matter waves. The analog of SSN interferometry in atomic spin sys-

tems uses entangled spin states to improve rotation angle estimation [109]. In particular, using SSN interferometry to measure ϕ can lead to improved frequency standards [103, 104, 67, 109]. Though two experiments using atomic spins [106, 107] have reduced the spin noise $\Delta J_\perp$ below the value expected for a CSS, these experiments did not apply the squeezing to interferometry.

Here we use entangled states of two ions to investigate two different schemes for rotation-angle estimation with precision better than that allowed by the SQL [109]. In each case we can estimate ζ better than allowed by the SQL, showing that SSN interferometry is indeed possible. We quantify the improvement beyond the SQL using the figure of merit [103, 104]

$$\xi_R = \frac{\delta\zeta}{\delta\zeta_{\mathrm{SQL}}} = \delta\zeta\sqrt{N} \tag{6.17}$$

A number of other measures of spin correlations are extant in the literature [110, 111, 102] and have led to a great deal of confusion in interpreting experimental results [106, 107]. In particular, the definition of [110, 111] gives different correlation values for different CSSs, even though the SQL is the same for all CSSs! The definition (6.17), on the other hand, provides a natural figure of merit for SSN interferometry schemes.

6.2.3 Squeezing Scheme

The "squeezing" scheme for SSN interferometry measures the same observable $\mathbf{J}_\perp$ as for CSS interferometry, but uses a spin-squeezed state (SSS) [102] as input to the interferometer. Fig. 6.4 compares the use of a CSS and an SSS in estimating θ. Both states satisfy the spin uncertainty relation [94, 102, 7]

$$\Delta\mathbf{J}_x\ \Delta\mathbf{J}_z \geq |\langle\mathbf{J}_y\rangle|/2 \tag{6.18}$$

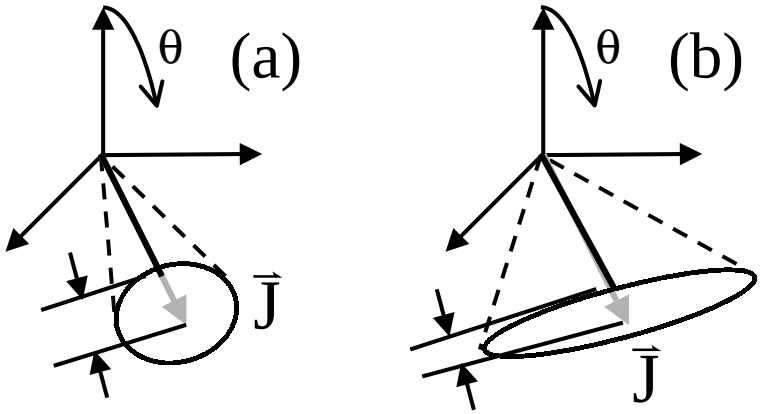

Figure 6.4: Using a CSS (a) and an SSS (b) to estimate the rotation angle θ. The squeezing of the uncertainty ellipse in (b) permits improved determination of θ.

but while the CSS has $\Delta \mathbf{J}_z = \Delta \mathbf{J}_y$, the SSS has $\Delta \mathbf{J}_z < \Delta \mathbf{J}_y$, allowing improved determination of the rotation angle θ about $\hat{y}$. The SSS takes its name from the squeezing of the "uncertainty ellipse" defined by the variances of the spin components, which is reminiscent of the squeezing of an optical field [9].

Our experiment used a two-ion SSS of form

$$\cos\alpha|\downarrow\downarrow\rangle - i\sin\alpha|\uparrow\uparrow\rangle \tag{6.19}$$

where α is the "squeezing angle." We generated the SSS from the initial state $|\downarrow\downarrow\rangle$ by applying the entangling evolution Eq. (5.6) with $k(t) = 2\pi/r$, where we write $r = \pi/\alpha$. To avoid entangling the spin with the motion, we required $h(t) = 0$, leading to the conditions

$$\Delta_M = \eta_k \Omega_{\rm sb} \sqrt{rj} \qquad t = \frac{2\pi}{\eta_k \Omega_{\rm sb}} \sqrt{\frac{j}{r}} \tag{6.20}$$

with j an integer. These conditions generalize Eq. (6.3) to arbitrary values of r. The usual entangling gate just has $r = 4$, $j = 1$, corresponding to $p = 1$ in Eq. (6.3). We realized SSS according to Eq. (6.19) with $r = 10$, 6, and 5. In each case we found the appropriate detuning

Δ_M by taking flopping curves while varying the endcap voltage. For $r = 10$ we used a detuning that yielded a flopping curve with five fast oscillations per slow oscillation and set the pulse duration equal to the period of the fast oscillations ($j = 1$). For $r = 5$ we used the same detuning, but doubled the pulse duration to give $j = 2$. For $r = 6$ we used a detuning with three fast oscillations per slow oscillation and set $j = 1$. In each case, the detunings correspond to noninteger p in Eq. (6.3), so these detunings do not allow operation of the usual entangling gate (Eq. 5.1). However, they are perfectly adequate for generating SSS of form (6.19).

After generating an SSS with the desired value of r, we applied a rotation $\mathbf{U}_{\rm car}(\theta \approx \pi/2, \phi, \phi)$. We then shelved the $|\uparrow\rangle$ state to the $^2\mathrm{S}_{1/2}\,|F = 1, m_F = 1\rangle$ state as described in Section 6.1 and counted the number of photons detected over 1 ms of illumination with BD. We performed 10 000 shots of this experiment at each value of ϕ, recording the number of photons detected for each shot individually. Building up a histogram from these 10 000 shots allowed us to set discriminators for that value of ϕ corresponding to the minimum detection error, as shown in Fig. 6.1. The detection errors are then the same as discussed in Section 6.1. Comparing the number of photons counted in a given shot to the discriminators determined the value of $\mathbf{J}_z$ for that shot.

The orientation of the uncertainty ellipse after the final rotation depends on ϕ, as shown in Fig. 6.5. Measuring the variance $\Delta\mathbf{J}_z(\phi)$ as a function of ϕ therefore maps out the uncertainty ellipse, where the minimum value of $\Delta\mathbf{J}_z(\phi)$ corresponds to the variance $\Delta\mathbf{J}_{\rm sqz}$ along the squeezed direction. We can also regard $\mathbf{J}_z$ as measuring the rotation angle θ of the final rotation, as shown in Fig. 6.4. In the absence of technical noise, our procedure determines θ to a precision

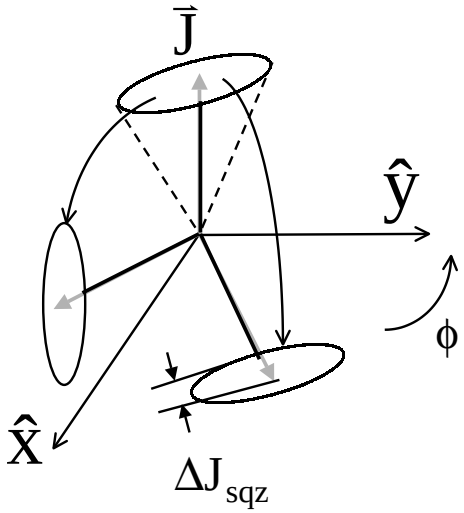

Figure 6.5: Mapping out the uncertainty ellipse of an SSS. The minimum value of $\Delta\mathbf{J}_z(\phi)$ corresponds to the variance $\Delta\mathbf{J}_{\rm sqz}$ along the squeezed direction.

$$\delta\theta(\phi) = \frac{\Delta\mathbf{J}_z(\phi)}{|\langle\vec{\mathbf{J}}\rangle|} \tag{6.21}$$

$$\xi_R(\phi) = \frac{\sqrt{1-\sin 2\alpha \sin 2\phi}}{\sqrt{2}\,|\cos 2\alpha|} \tag{6.22}$$

While $\delta\theta$ attains its theoretical minimum value of 1/2 for $\alpha = \pi/4$, we also find $|\langle\vec{\mathbf{J}}\rangle| = 0$. Any technical noise in the measurement of $\mathbf{J}_z$ then induces large errors in estimating θ, so that we cannot achieve the optimum $\delta\theta$ in practice. We demonstrated SSN interferometry with the $\alpha = \pi/4$ state $|\downarrow\downarrow\rangle + |\uparrow\uparrow\rangle$ using the "parity" scheme described below.

Fig. 6.6 shows measurements of $\delta\theta(\phi)$ for the squeezing scheme with $r = 10$. The data follow the theoretical prediction of Eq. (6.22) fairly well. Though the measured minimum uncertainty $\delta\theta_{\rm min} = 0.65 \pm 0.01$ is considerably larger than the ideal minimum uncertainty $\delta\theta_{\rm ideal} = 0.56$ for this value of r, it is still considerably smaller than the SQL uncertainty $\delta\theta_{\rm SQL} = 1/\sqrt{2}$. We have $\xi_R = 0.92 \pm 0.01$, clearly demonstrating SSN measurement of θ.

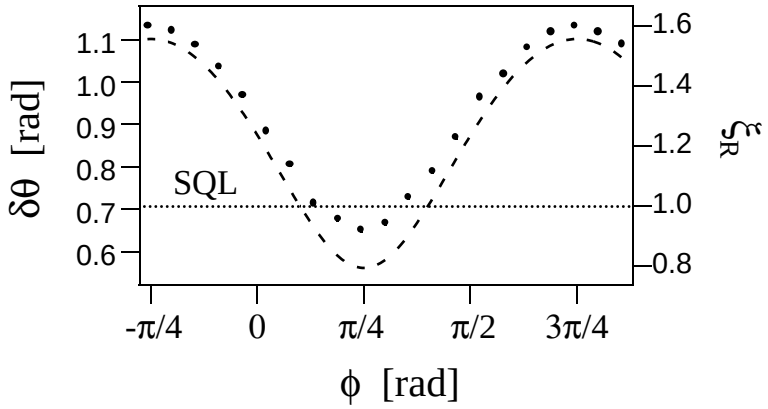

Figure 6.6: Measurements of $\delta\theta(\phi)$ as a function of the rotation phase ϕ for the squeezing scheme with $r = 10$. The data (dots) follow the ideal error (dashed curve) fairly well. Error bars for the data are smaller than the marker size.

We measured $\delta\theta(\phi)$ as a function of ϕ for all three cases ($r = 10$, 6, and 5). Table 6.2 compares the measured minimum values of $\delta\theta$ to the prediction of Eq. (6.22). The figure of merit ξ_R decreases with increasing squeezing angle α (Eq. 6.19). We believe that the loss of precision arises from imperfect preparation of the SSS.

6.2.4 Parity Scheme

The "parity" scheme uses the maximally entangled state $|\downarrow\rangle^N + |\uparrow\rangle^N$ encountered in Section (5) to estimate the angle ϕ. In this case $|\langle\vec{\mathbf{J}}\rangle| = 0$, so we cannot define $\mathbf{J}_\perp$ and the CSS method breaks down. Instead we perform a $\pi/2$ rotation at phase ϕ and measure the expectation value of the parity operator $\mathbf{\Pi} = \mathbf{S}_{1,z}\mathbf{S}_{2,z}$, just as in Section 5.2. Ideally this scheme attains the Heisenberg limit $\delta\phi = 1/N$ set by the uncertainty relation (6.18). For large N this uncertainty is a vast improvement over the SQL $\delta\phi = 1/\sqrt{N}$, allowing corresponding improvements in atomic clocks [103, 104, 67]. Our implementation of this scheme with two ions shows $\delta\phi_R < 1/\sqrt{2}$, a clear proof of principle for this method. A variant of this scheme using pairs of entangled

Table 6.2: Figure of merit ξ_R for SSN estimation of θ as a function of squeezing angle α. The loss of precision probably arises from imperfect preparation of the SSS.

α	Measured ξ_R	Ideal ξ_R
$\pi/10 = 18°$	0.92	0.79
$\pi/6 = 30°$	0.96	0.73
$\pi/5 = 36°$	1.40	0.72

photons previously demonstrated SSN estimation of θ [105].

The parity scheme is closely related to the dual Fock-state scheme considered in optical and matter-wave interferometry [112, 113, 114, 115, 105, 116]. In the spin representation, the state propagating through the interferometer is again the state $|\downarrow\rangle^N + |\uparrow\rangle^N$, but the observable is the variance $\mathbf{V} = \mathbf{J}_z^2 - \langle \mathbf{J}_z \rangle^2$ rather than $\mathbf{J}_z$. For two particles, $\mathbf{V} = (1 + \mathbf{\Pi})/2 - \langle \mathbf{J}_z \rangle^2$, so the dual Fock-state scheme and the parity scheme are equivalent. Our data, like that of [105], can thus be seen as testing both schemes.

We measured the number of photon counts at each value of ϕ over 10 000 shots and extracted $\mathbf{J}_z$ for each shot, just as described for the squeezing method. Fig. 6.7(a) shows the observed mean $\langle \mathbf{\Pi} \rangle$ and variance $(\Delta \mathbf{\Pi})^2$ of the parity as a function of ϕ. For comparison, Fig. 6.7(b) shows the expected mean and variance for a perfect input state $|\downarrow\downarrow\rangle + |\uparrow\uparrow\rangle$ and ideal rotation and detection. The imperfect preparation of the entangled state significantly increases the variance for $|\langle \mathbf{\Pi} \rangle| \sim 1$, but is clearly dominated by the quantum noise (Eq. 6.12) for $|\langle \mathbf{\Pi} \rangle| \sim 0$. We can directly derive the uncertainty $\delta\phi$ from the data using Eq. (6.11). Fig. 6.8 shows these derived values of $\delta\phi$ as a function of ϕ. While the technical noise increases $\delta\phi$ well above the SQL for $|\langle \mathbf{\Pi} \rangle| \sim 1$, $\delta\phi$ drops significantly below the SQL for $|\langle \mathbf{\Pi} \rangle| \sim 0$. The minimum value of $\delta\phi$ is $0.59 \pm 0.01 < 1/\sqrt{2}$, giving a squeezing factor $\xi_R = 0.83 \pm 0.01$.

6.2.5 Sub-Shot-Noise Ramsey Spectroscopy

The parity method clearly improves our estimate of ϕ, so it should also allow improved determination of ω_R in atomic clocks [103, 104, 67]. To demonstrate this result directly, we performed Ramsey spectroscopy with a nonclassical input state. Table 6.9 gives the sequence of operations used for this experiment. Here the state after operation 4 is

$$|\Psi\rangle_{\rm out} = \sin(2T_R\Delta\omega)\left[e^{-i(\alpha+\phi_{\rm fluct})}|\downarrow\downarrow\rangle - e^{i(\alpha+\phi_{\rm fluct})}|\uparrow\uparrow\rangle\right] - \cos(2T_R\Delta\omega)\left[|\downarrow\uparrow\rangle + |\uparrow\downarrow\rangle\right] \quad (6.23)$$

so that $\langle\mathbf{\Pi}\rangle = \sin^2(2T_R\Delta\omega_R)$. Operations 0 through 2 prepare the desired input state $|\downarrow\uparrow\rangle+|\uparrow\downarrow\rangle$, while operations 3 through 5 perform Ramsey spectroscopy on the input state. We scanned the accumulated phase $T_R\omega_R$ by detuning operations 3 and 5 from the carrier frequency by about 10 kHz and scanning the free evolution time T_R. Our experiment implements the Heisenberg-limited Ramsey scheme of [67], for which the state between the Ramsey $\pi/2$ pulses must be the state $|\downarrow\rangle^N + e^{i\beta}|\uparrow\rangle^N$ for some phase β.

The sensitivity of Ramsey spectroscopy scales as the time T_R between the Ramsey $\pi/2$ pulses, so atomic clocks usually use the longest feasible T_R [88, 89]. In our case, heating affects carrier pulses performed with the B1, R2 beams after a few tens of μs (Sec. 7.4), effectively limiting T_R. We therefore used the copropagating B1, R1 beams for operations 3 and 4. However, we could only perform the entangling gate using the B1, R2 beams (Sec. 5.2). The phase difference $\phi_1-\phi_2$ for any operation using B1, R1 is zero, since $\vec{\Delta}k = 0$ for these beams. The method of [67] requires the state after operation 3 to be $|\downarrow\downarrow\rangle + e^{i\beta}|\uparrow\uparrow\rangle$, so the state before operation 3 must be $|\downarrow\uparrow\rangle+|\uparrow\downarrow\rangle$, forcing $\phi_1-\phi_2 = 0$ for operation 2 as well. The ions therefore had to be separated by

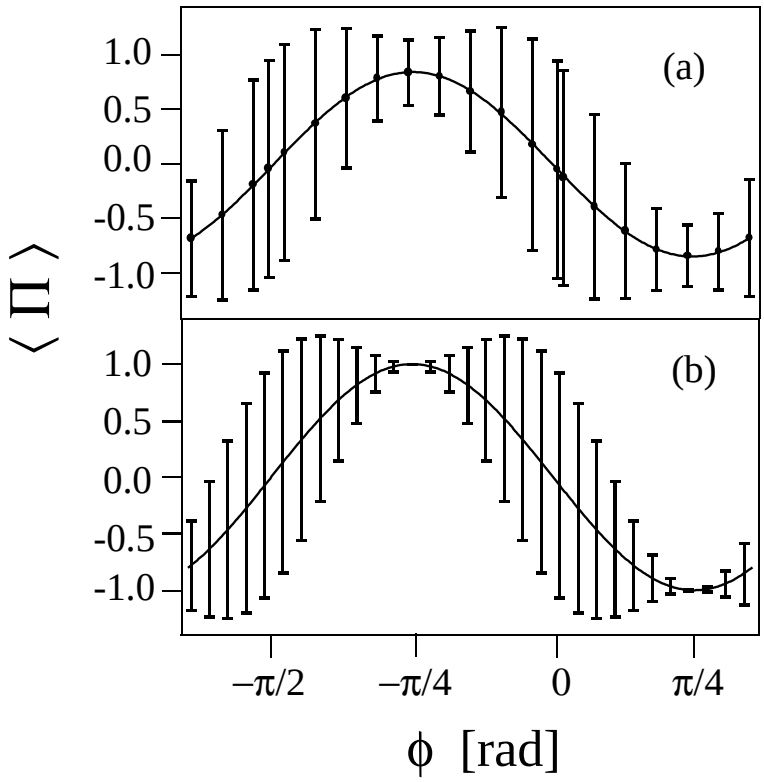

Figure 6.7: Mean and variance of the parity operator $\mathbf{\Pi}$ in the parity scheme for SSN interferometry. (a) Experimental data, 10 000 shots per point. Points give the mean value of $\mathbf{\Pi}$ as a function of ϕ, error bars give the variance. The curve is the best fit to the mean of $\mathbf{\Pi}$. (b) Theoretical values for perfect state preparation and measurement. The curve is the ideal value of the mean as a function of ϕ, and error bars give the ideal variance.

Table 6.3: The sequence of operations implementing SSN Ramsey spectroscopy. Operations 0 through 2 prepare the nonclassical input state, while operations 3 through 5 perform Ramsey spectroscopy on the input state. We define the zero of RF phase such that $\phi_1 + \phi_2 = 0$ for pulse 1.

Number	Operation	Beams Used	$\phi_1 + \phi_2$	$\phi_1 - \phi_2$	State After Operation
0	initialize	–	–	–	$\|\downarrow\downarrow\rangle$
1	$\mathbf{U}_{\rm ent}$	B1, R2	0	ϕ_λ	$\|\downarrow\downarrow\rangle - i\|\uparrow\uparrow\rangle$
2	$\mathbf{U}_{\rm car}(\theta = \pi/2)$	B1, R2	$-\pi/4$	0	$\|\downarrow\uparrow\rangle + \|\uparrow\downarrow\rangle$
3	$\mathbf{U}_{\rm car}(\theta = \pi/2)$	B1, R1	$\phi_{\rm fluct}$	0	$\|\downarrow\downarrow\rangle + e^{2i\phi_{\rm fluct}}\|\uparrow\uparrow\rangle$
4	wait	–	–	–	$\|\downarrow\downarrow\rangle + e^{2i(\phi_{\rm fluct} - T_R\Delta\omega)}\|\uparrow\uparrow\rangle$
5	$\mathbf{U}_{\rm car}(\theta = \pi/2)$	B1, R1	$\phi_{\rm fluct}$	0	$\|\Psi_{\rm out}\rangle$
6	detect	–	–	–	–

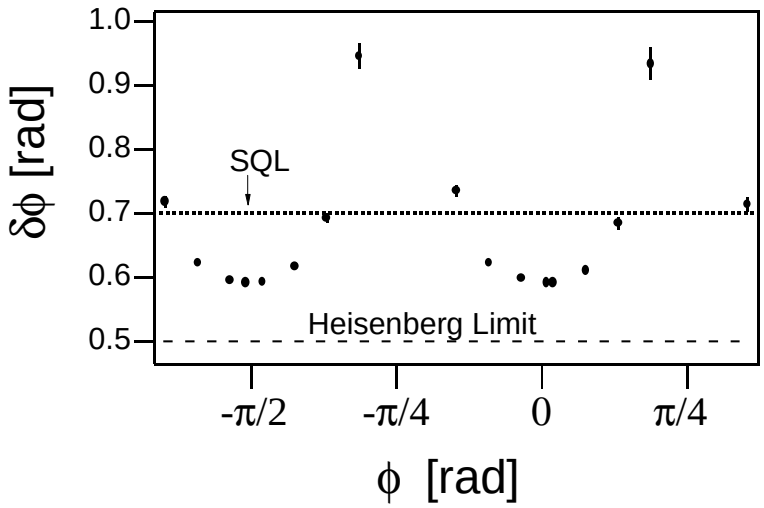

Figure 6.8: Measurement uncertainty $\delta\phi$ derived from the data of Fig. 6.7(a). For certain values of ϕ the uncertainty drops below the SQL, demonstrating SSN interferometry.

a distance $s_0 = 2\pi n/(\sqrt{2}k)$ for operation 2, where n is an integer. Because of the fixed resonant frequency of the entangling EOM (Sec. 4.4), we could not satisfy this condition for operation 1. We therefore changed the endcap voltage between operations 1 and 2 to produce $\phi_1 - \phi_2 = 0$ for operation 2. Minimizing P_1 for the state after operation 3 ensured this condition.

The relative optical phase between R1 and R2 was not stabilized for this experiment, so that even if the Ramsey pulses were not detuned from the logic pulses, random changes in the relative path length produced a fluctuating phase ϕ_{fluct}, as shown in Table 6.9. We had previously characterized this phase using simple Ramsey spectroscopy on a single ion. When we applied one $\pi/2$ pulse with the B1, R1 beams and the other with the B1, R2 beams, we observed the usual Ramsey fringes (Eq. 6.6) for measurement times of a few tenths of a second. At longer measurement times the phase of the fringes shifted randomly and suddenly, indicating an abrupt change of the relative path length. The cause of the fluctuations remains unknown. Since we usually needed 1 s or more to achieve the high signal-to-noise ratio characteristic of our experiment, we could not perform experiments that required phase coherence between B1, R2

operations and B1, R1 operations. Surprisingly, the experiment described in Table 6.9 does not require coherence between the operations using R2 and those using R1. While the final state $|\Psi_{\text{out}}\rangle$ does indeed vary with ϕ_{fluct}, the populations depend only on the accumulated phase $T_R\omega_R$ because of the particular form of the input state $|{\downarrow}{\uparrow}\rangle + |{\uparrow}{\downarrow}\rangle$. Other input states generally give rise to a signal dependent on ϕ_{fluct}, limiting measurement time to less than 1 s.

We collected parity data at several values of T_R in the way described previously. Using Eq. (6.11), we obtained the measurement uncertainty $T_R\delta\omega_R$ as a function of T_R. The data are shown in Fig. 6.9. Since scanning T_R is equivalent to scanning the phase ϕ in the previous parity experiment, the data of Fig. 6.9 are similar to that of Fig. 6.8. Again, the technical noise increases the uncertainty far above the SQL for values of T_R corresponding to $|\langle\mathbf{\Pi}\rangle| \sim 1$, but the uncertainty drops well below the SQL for T_R such that $|\langle\mathbf{\Pi}\rangle| \sim 0$. The maximum gain in precision is a factor of 1.14 ± 0.01, corresponding to $\xi_R = 0.88 \pm 0.01$. Here we are comparing the precision obtained with our imperfect state preparation and measurement to the precision obtained for an experiment on a CSS of two ions with ideal preparation and measurement. The SSN Ramsey scheme [67] for two ions is thus more precise than any concievable frequency measurement on two unentangled ions. The value of ξ_R measured here is consistent with that measured for the previous parity experiment, since the Ramsey $\pi/2$ pulses add some extra noise to the SSN Ramsey experiment.

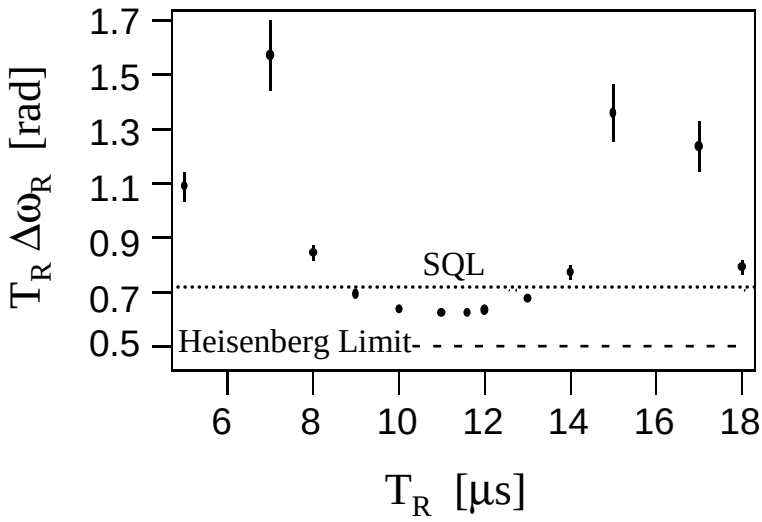

Figure 6.9: Frequency uncertainty $T_R\delta\omega$ as a function of T_R. The uncertainty drops below the SQL for T_R such that $|\langle\mathbf{\Pi}\rangle| \sim 0$, demonstrating SSN Ramsey interferometry.

Chapter 7

Decoherence of the Quantum Register

7.1 Dephasing of Internal States

A qubit in one of the basis states $|\downarrow\rangle$, $|\uparrow\rangle$ is practically unaffected by its environment in our experiments. The radiative lifetime of our qubit states is long ($\gg 10^{12}$ s), so the qubit levels $|\downarrow\rangle$, $|\uparrow\rangle$ do not decay. Stray radiation coupling the basis states must have a frequency near the hyperfine splitting of 1.25 GHz. Typical ambient noise power at this frequency is so small as to be negligible. Quasistatic rotation of the quantization field is also negligible, since ambient fluctuating field strengths are much less than the quantization field strength.

Notwithstanding these facts, a qubit in a superposition state $|\psi(\phi)\rangle = |\downarrow\rangle + e^{i\phi}|\uparrow\rangle$ is readily susceptible to changes in its phase ϕ. In Section 6.2.1, we showed how to exploit this effect to stabilize the frequency of an LO to an atomic transition, realizing an atomic clock. Ideally, the LO and atomic phases are synchronized at all times, so that in a frame rotating at the LO frequency the state $|\psi(\phi)\rangle$ remains the same as time passes. If the relative phase drifts by an unknown amount ϕ_d, though, we might presume that we have the state $|\psi(\phi)\rangle$ when in fact we have $|\psi(\phi+\phi_d)\rangle$. Now suppose that the state $|\psi(\phi)\rangle$ is the state after the first $\pi/2$ pulse of a Ramsey experiment and ϕ_d is characterized by a Gaussian distribution of width σ_ϕ over the free evolution time T_R. The second $\pi/2$ pulse rotates the density matrix $\boldsymbol{\rho}$ associated with the

state after the first $\pi/2$ pulse and the subsequent measurement of $\mathbf{S}_z$ gives the coherence $\boldsymbol{\rho}_{\downarrow,\uparrow}$ as

$$\langle \mathbf{S}_z \rangle_\phi = |\boldsymbol{\rho}_{\downarrow,\uparrow}| \sin\phi \tag{7.1}$$

$$= \frac{1}{2} \int \sin(\phi + \phi_d) \left(\frac{d\phi_d}{\sqrt{2\pi}\sigma_\phi} \exp\left[-\frac{\phi_d^2}{2\sigma_\phi^2} \right] \right) \tag{7.2}$$

$$= \frac{1}{2} \exp[-2\sigma_\phi^2] \sin\phi \tag{7.3}$$

so that the coherence is reduced by a factor $\exp[-2\sigma_\phi^2]$ from its ideal value. This type of decoherence, known as dephasing, occurs whenever an unknown phase is added to a superposition state.

To evaluate σ_ϕ, we must consider the physical process inducing dephasing. If the process acts for a time τ and has a spectral density $S_\phi(\omega)$ for the phase fluctuation ϕ_d, the Wiener-Khintchine theorem yields [117]

$$\sigma_\phi^2 = 2 \int_0^\infty S_\phi(\omega) \frac{\sin\omega\tau}{\omega\tau} \, d\omega \tag{7.4}$$

Frequently we can approximate $S(\omega)$ by white noise with a high-frequency cutoff ω_{lp}, so that

	$S(\omega = 1/\tau)$	σ_ϕ	$\lvert\boldsymbol{\rho}_{\downarrow,\uparrow}\rvert$
$\tau \lesssim 1/\omega_{\mathrm{lp}}$	S_0	$\propto \tau$	$\propto \exp^{-(\tau/T_{\mathrm{lp}})^2}$
$\tau \gtrsim 1/\omega_{\mathrm{lp}}$	0	$\propto \sqrt{\tau}$	$\propto \exp^{-\tau/T_2}$

(7.5)

In the white-noise case, $\omega_{\mathrm{lp}} \to \infty$ and we have an exponential decay for all times, with decay rate set by the dephasing time T_2. In the other limit we have Gaussian decay with dephasing time T_{lp}.

We can describe dephasing as implementing transformations $|\downarrow\rangle_j \to |\downarrow\rangle_j$, $|\uparrow\rangle_j \to e^{i\phi_{d,j}}|\uparrow\rangle_j$, where j indexes the qubits and the $\phi_{d,j}$ are (possibly correlated) random variables. From this standpoint it is easy to characterize dephasing of a general density matrix of N qubits. Using the product basis $\{|k\rangle\}$ over the single-qubit states $\{|\downarrow\rangle, |\uparrow\rangle\}$, we can write the dephased density matrix $\boldsymbol{\rho}'$ in terms of the original density matrix $\boldsymbol{\rho}$ as

$$\rho'_{k,k'} = \langle k'|\boldsymbol{\rho}|k\rangle \tag{7.6}$$

$$\to \exp\left[i\sum_{j=1}^{N}\phi_{d,j}\left(\langle \mathbf{S}_{z,j}\rangle_k - \langle \mathbf{S}_{z,j}\rangle'_k\right)\right]\rho_{k,k'} \tag{7.7}$$

$$\sim \exp[i\phi_d(\langle \mathbf{J}_z\rangle_k - \langle \mathbf{J}_z\rangle_{k'}]\rho_{k,k'} \qquad \text{if } \phi_{d,j} \approx \phi_d \text{ for all } j \tag{7.8}$$

For white noise, we find that the dephasing time for a general state of N ions is no faster than T_2/N (and can be much slower: see Chap. 8). This result contrasts strongly with similar results on dephasing of harmonic oscillators. In the latter case, the dephasing time between Fock states $|n\rangle$ and $|n'\rangle$ scales as $|n-n'|^2$ [118, 119, 120]. Apparently, large superposition states made of qubits are much less susceptible to decoherence than large superpositions made with a harmonic oscillator.

In our experiment, dephasing during free evolution of the register mostly arose from fluctuating magnetic fields. To first order, these fields did not change the direction of the quantization field, but they did change its magnitude: the Zeeman effect shifted $\omega_{\downarrow\uparrow}$ by about 21 GHz/T. The Raman beatnote was derived from a high-stability RF source and has negligible phase noise.[1] We actively stabilized the magnetic field using a pair of coils perpendicular to, and centered on, the path of BD. The coils were placed 10 cm on each side of the trap. Fluctuating magnetic fields induced currents on one coil, which were picked up, amplified, and driven through the other coil. This feed-forward arrangement reduced the magnetic field fluctuation

[1] In contrast to the atomic-clock situation, here the LO was stable and the atomic transition fluctuated.

by about a factor of two. The $1/e$ time for decay of the coherence was about 150 μs with this arrangement.

Almost all the magnetic field noise comes from AC power line noise, so its spectrum is concentrated at 60 Hz and its harmonics. The analysis leading to Eq. 7.1 is therefore invalid, since ϕ_d is correlated from shot to shot. If we assume that the fluctuations are sinusoidal with a period much longer than the duration of a single shot, we find $\phi_d = \beta T_R \sin\phi_n$ over one shot, where β measures the amplitude of the frequency fluctuations and ϕ_n is the fluctuation phase for that shot. The analog of Eq. (7.1) is then

$$\langle \mathbf{S}_z \rangle_\phi = \int_0^{2\pi} \sin\left(\phi + \beta \sin\phi_n\right) \left(\frac{d\phi_n}{\sqrt{2\pi}}\right) \tag{7.9}$$

$$= \frac{1}{2} J_0(2\beta T_R) \sin\phi \tag{7.10}$$

where J_0 is a Bessel function. The coherence (Eq. 7.9) exhibits collapses and revivals as βT_R increases. For fixed β, the Bessel function asymptotically decays as $T_R^{-1/2}$, rather than decaying exponentially. However, for short times the coherence decays as a Gaussian, as in Eq. (7.5). In real life, the magnetic field noise is neither monochromatic nor Gaussian, but the coherence does in fact exhibit collapses and revivals.

We performed a Ramsey experiment with a single ion on the transition between the ${}^2\mathrm{S}_{1/2}$ $|F = 2, m_F = 0\rangle$ and $|F = 1, m_F = 0\rangle$ hyperfine states. Here the transition frequency has only a quadratic Zeeman shift at zero field. At our field strength of 165 μT we estimate a Zeeman shift of 1.2 kHz/μT, as compared to the 21 kHz/μT Zeeman shift of the $|\downarrow\rangle \leftrightarrow |\uparrow\rangle$ transition. After initializing the ion in $|\downarrow\rangle$, shelving pulses using B1 and R1 transferred the ion to $|\uparrow\rangle$, then to $|F = 2, m_F = 0\rangle$. From Eq. (3.37), driving the $|F = 2, m_F = 0\rangle \leftrightarrow |F = 1, m_F = 0\rangle$

transition requires circular polarization of both Raman beams in the atomic basis, so we used the B2, R2 beams to perform the Ramsey $\pi/2$ pulses. After the $\pi/2$ pulses, we transferred the population in $|F = 2, m_F = 0\rangle$ back to $|\downarrow\rangle$ and measured the fluorescence. These measurements showed that the coherence lasted for a $1/e$ time of about 1 ms, rather than the 150 μs found for the $|\downarrow\rangle \leftrightarrow |\downarrow\rangle$ transition.

7.2 Single-Qubit Gate Errors

The results on Raman transitions presented in Chapter 3 assume that the ion state evolves coherently under the Raman Hamiltonian (3.42). In reality, many mechanisms create decoherence during Raman transitions, causing errors in our quantum logic gates. The fundamental source of error is spontaneous emission from the small state amplitude in the P manifold, which has an inevitable lower bound depending on the atomic structure. Since the logic Hamiltonian depends on the ions' motional state, any thermal motion of the ions can lead to gate errors (see Sec. 7.4 below.) In addition, technical noise in the Raman beams can create gate errors, though in principle such errors can be very small.

7.2.1 Characterization of Gate Errors

In Section 7.1, we saw that dephasing is the only decoherence mechanism affecting one of our qubits under ambient conditions. However, during a logic gate, processes like spontaneous Raman scattering can change the populations of internal states as well as their coherences, causing decay of the populations toward some equilibrium distribution. To quantify the relative importance of dephasing and population decay, we consider the decoherence of a single qubit arising from a rotation applied to that qubit. From Eq. (7.1), a phase error ϕ_d transforms

$$\rho_{k,k'} \to \exp[-2\sigma_\phi^2(\langle \mathbf{S}_z\rangle_k - \langle \mathbf{S}_z\rangle_{k'})]\rho_{k,k'} \tag{7.11}$$

where $\mathbf{S}_z$ acts on the rotated ion. To model exponential decay of the populations by a factor γ_r toward an equilibrium distribution $P_k^{\rm eq}$ over the product basis states, we make the transformation

$$\rho_{k,k} \to e^{-\gamma_r}\rho_{k,k} + (1 - e^{-\gamma_r})\rho_{k,k}^{\rm eq} \tag{7.12}$$

We can measure the error induced by a decoherence process using the fidelity $F = \mathrm{Tr}[\boldsymbol{\rho}\boldsymbol{\rho}']$ as

$$\epsilon = 1 - F = 1 - \mathrm{Tr}[\boldsymbol{\rho}\boldsymbol{\rho}'] \tag{7.13}$$

where $\boldsymbol{\rho} \to \boldsymbol{\rho}'$ under the decoherence. We take $\boldsymbol{\rho}$ to represent an intermediate state in a large quantum computation. In such a state, the populations are about equally distributed over the possible measurement basis states, so we take $\rho_{k,k} \sim 1/2^N$ for any product basis state $|k\rangle$. Assuming maximum coherence of the register state, we find $\rho_{k,k'} \sim 1/2^N$ for any $|k\rangle$, $|k'\rangle$ as well. Then the error due to dephasing is

$$\epsilon = \sum_{k,k'} \rho_{k,k'}(1 - \exp[-2\sigma_\phi(\langle \mathbf{S}_z\rangle_k - \langle \mathbf{S}_z\rangle'_k)])\rho_{k',k} \tag{7.14}$$

$$\sim 1 - \frac{1}{2}e^{-\sigma_\phi^2}\mathrm{Tr}\left[\boldsymbol{\rho}^2\right] \sim 1 - \frac{1}{2}\, e^{-\sigma_\phi^2} \tag{7.15}$$

since $\langle \mathbf{S}_z\rangle_k - \langle \mathbf{S}_z\rangle'_k = 1$ for about half the possible choices of $|k\rangle$, $|k'\rangle$. On the other hand, the error due to population decay is

$$\epsilon = \sum_k \rho_{k,k}(1 - e^{-\gamma_r})(\rho_{k,k} + P_k^{\rm eq}) \tag{7.16}$$

$$\sim \frac{1 - e^{-\gamma_r}}{2^N} \sum_k \left(\frac{1}{2^N} + P_k^{\rm eq}\right) \tag{7.17}$$

$$\lesssim \frac{1 - e^{-\gamma_r}}{2^N} \tag{7.18}$$

Any process that causes population decay also causes dephasing, so we see that as the quantum register becomes large ($N \to \infty$) we can ignore relaxation errors.

Noise processes in a single-qubit gate introduce fluctuations in the phase or the polar angle of the rotation operator $\mathbf{U}_{\text{car}}$ (Eq. 5.26). Solving the optical Bloch equations with dephasing [36] shows that the presence of noise causes decay of the inversion $\langle \mathbf{S}_z \rangle(t)$ and coherence $\langle \mathbf{S}_+ \rangle$. To observe the effects of noise in the experiment, we typically performed Rabi flopping on the carrier resonance of a single ion and observed the decay envelope of the Rabi oscillations. We could then characterize the noise by fitting the observed decay to the model based on the Bloch equations.

For perfect rotations, the inversion and coherence oscillate at the Rabi frequency Ω_R, so the duration $t = \theta/\Omega_R$ of the Raman pulse sets the timescale of interest for the noise. Assuming a flat noise spectrum with a high-frequency cutoff ω_{lp}, we find two limiting cases, as in Section 7.1: the white noise regime $\omega_{\text{lp}} \gtrsim \Omega_R$ and the slow noise regime $\omega_{\text{lp}} \lesssim \Omega_R$. White noise in θ and ϕ have roughly the same effect, so we model both by including white-noise dephasing in the optical Bloch equations. Starting from $|\downarrow\rangle$ and applying a carrier pulse of duration t, we find in this model

$$\langle \mathbf{S}_+ \rangle = e^{-t/T_2} \sin \Omega_R t \tag{7.19}$$

$$\langle \mathbf{S}_z \rangle = -\frac{1}{2}\, e^{-t/T_2} \cos \Omega_R t \tag{7.20}$$

so that dephasing **during** a logic gate causes decay of the ion populations ($\propto \langle \mathbf{S}_z \rangle$) as well as decay of the coherence ($\propto \langle \mathbf{S}_+ \rangle$).

In the experiment, the effects of slow noise in θ dominate the slow noise in ϕ. To model this noise, we average the noiseless solution to the Bloch equations over a Gaussian distribution in θ centered about the desired value $\overline{\theta}$. We find

$$\langle \mathbf{S}_+ \rangle = e^{-(t/T_{\mathrm{lp}})^2} \sin \Omega_R t \tag{7.21}$$

$$\langle \mathbf{S}_z \rangle = -\frac{1}{2}\, e^{-(t/T_{\mathrm{lp}})^2} \cos \Omega_R t \tag{7.22}$$

where we have exploited the similarity to Eq. (7.5) to define an effective dephasing time T_{lp}.

In both models, the inversion and the coherence decay in the same way, so we can use flopping curves on one ion to extract the effective dephasing behavior due to any source of gate error. Hence we can predict the effect of gate errors on a large register from the behavior of a single ion. Since the decay of coherence under gate errors is similar to that under ambient noise (Sec. 7.1), we can describe both gate errors and ambient noise in terms of the associated white-noise dephasing time T_2 and slow-noise dephasing time T_{lp}. Adding the contributions from several (small) sources of noise gives the overall dephasing times as

$$\frac{1}{T_2} = \sum_j \frac{1}{T_{2,j}} \qquad \frac{1}{T_{\mathrm{lp}}^2} = \sum_j \frac{1}{T_{\mathrm{lp,j}}^2} \tag{7.23}$$

where j labels the individual noise sources.

7.2.2 Spontaneous Emission

Although the Raman laser detuning is always much larger than the linewidth $\Gamma = 2\pi \times 19.4$ MHz of the S $\leftrightarrow$ P transition, a small part of the atomic population remains in the P state

throughout a Raman transition. This population can spontaneously decay, emitting a photon with a random phase and adding a correlated random phase to the hyperfine coherence $\boldsymbol{\rho}_{12}$ in the process. Since we cannot recover the emitted photon phase, a spontaneous scattering event essentially destroys the hyperfine coherence. Assuming that the Raman beam intensities are constant across the ion crystal, the probability that a spontaneous scattering event will occur at a particular ion is [9]

$$P_{\rm se} = \gamma_{\rm se} T \tag{7.24}$$

$$\gamma_{\rm se} \equiv \sum_{j=1,2} \sum_{k=\{1/2,3/2\}} \Omega_j^2 \Gamma \frac{R^{(k)}_{{\rm Stark},j}}{\Delta_k^2} \tag{7.25}$$

for a Raman pulse of length T. If no emission event occurs, the density matrix after the logic gate is the ideal density matrix $\boldsymbol{\rho}_I$. However, if an event occurs at ion i, all coherences involving ion i vanish. A little algebra shows that spontaneous scattering from the Raman beams effectively induces white-noise dephasing with $T_2 = 1/\gamma_{\rm se}$.

The probability of dephasing during a 2π carrier pulse is $P_{{\rm se},2\pi}(\Delta) = 2\pi\gamma_{\rm se}/|\Omega_{12}|$, where Ω_{12} is given by Eq. (3.40.) This quantity is a convenient measure of the spontaneous emission error per gate. We have

$$P_{{\rm se},2\pi} = \frac{2\pi\Gamma}{R_{\rm Raman}\Omega_1\Omega_2} \left|\Delta\left(1 - \frac{\Delta}{\omega_{\rm FS}}\right)\right| \sum_{j=1,2} \sum_{k=\{1/2,3/2\}} \Omega_j^2 \frac{R^{(k)}_{{\rm Stark},j}}{\Delta_k^2} \tag{7.26}$$

For the beams B1, R2 used to drive logic gates on the $|{\downarrow}\rangle \leftrightarrow |{\uparrow}\rangle$ transition, we have $\hat{\epsilon}_{\rm B1} = \pi$, $\hat{\epsilon}_{\rm R2} = \sigma^+ + \sigma^-$. Then writing $|\Omega_{\rm B1}| = r|\Omega_{\rm R2}|$, we find

$$P_{{\rm se},2\pi}(\Delta, r) \propto \left|\Delta\left(1 - \frac{\Delta}{\omega_{\rm FS}}\right)\right| \left(\frac{2r^2+5}{3r}\frac{1}{\Delta^2} + \frac{4r^2+8}{3r}\frac{1}{(\omega_{\rm FS}-\Delta)^2}\right) \tag{7.27}$$

which exhibits a broad minimum near 313.160 nm and $r = 1.5$ with $\mathcal{P}_{\rm se} \approx 6 \times 10^{-3}$. For the experimental Raman wavelength 313.341 nm, and allowing for day-to-day variations of r from

0.5 to 2, the value of $P_{\mathrm{se},2\pi}$ is larger than the minimum by no more than a factor of 2.

The relatively large gate error $P_{\mathrm{se},2\pi}$ limits us to a few tens of quantum logic operations. We cannot reduce this source of error through technical improvements. However, from Eq. (7.27), we see that $P_{\mathrm{se},2\pi}$ scales as $1/\omega_{\mathrm{FS}}$. While the $^9\mathrm{Be}^+$ ion has a relatively small $\omega_{\mathrm{FS}} \approx 2\pi \times 197$ GHz, heavier ions can have much larger values of ω_{FS}, e.g., tens of THz for Cd^+. For this reason, such ions may be more promising qubits than $^9\mathrm{Be}^+$ for large-scale quantum computation.

Finally, we note that an ion can change hyperfine state on spontaneously scattering a photon from the Raman beams. Both Rayleigh and Raman scattering can occur. The transition rate from the initial state $|i\rangle$ to the final state $|f\rangle$, with $i \neq f$, is just

$$T(i,f) = \sum_{j=1,2} \sum_{k=\{1/2,3/2\}} \sum_{\mathcal{F}_k} \sum_{\hat{\epsilon}_a} \Omega_j^2 \Gamma \frac{S(i,\mathcal{F}_k;\hat{\epsilon}_a) S(f,\mathcal{F}_k;\hat{\epsilon}'_a)(\hat{\epsilon}^*_a \cdot \hat{\epsilon}_j)}{\Delta_k^2} \tag{7.28}$$

from which we can deduce the population decay under spontaneous emission. This process can remove an ion from the computational basis $\{|\downarrow\rangle, |\uparrow\rangle\}$ entirely. The relaxation is a useful diagnostic, as we could deduce the single-photon Rabi frequency of a Raman beam by applying that beam alone and observing the decay of the ion populations. During quantum logic operations, however, the population decay from this effect was much smaller than the population decay from dephasing.

7.2.3 Ion Motion

The Rabi frequency of logic transitions (3.22) is a function of the Fock state of the ion motion. Assuming that the motional state does not change much over the course of a Raman pulse, the evolution under the logic Hamiltonian is no longer sinusoidal but becomes a sum of Rabi flopping curves of form (3.21) weighted by the populations of the motional Fock states. This indirect effect of the ion motion on the carrier transition is analogous to the Debye-Waller (DW) effect encountered in condensed-matter physics [121].

Here we will treat only the decoherence of the carrier transition. We will discuss decoherence of the two-ion gate in Sec. 5. For one ion, the Rabi frequency (3.22) reduces to $\Omega_n \equiv \Omega_{n,n} = \Omega_R e^{-\eta^2/2}(1 - n\eta^2)$. If the ions are not perfectly cold, n fluctuates about its average value $\overline{n}$, so that $\theta = \Omega_n t$ effectively fluctuates from shot to shot, as in the slow-noise model. Expanding about the average value $\overline{\Omega} = \Omega_R e^{-\eta^2/2}(1 - \overline{n}\eta^2)$ gives

$$T_{\mathrm{lp,DW}} = \left[\sum_n P_n(\Omega_n - \overline{\Omega})^2\right]^{-1/2} \tag{7.29}$$

For multiple ions, the gate error from the DW effect depends on the fluctuations in all N axial modes. Writing $T_{\mathrm{lp,j}}$ the error due to the jth mode, we find the total decay time $T_{\mathrm{lp,DW}}$ from Eq. (7.23). If the ions are in the Lamb-Dicke limit and each of the N axial modes is in a thermal state of average excitation $\overline{n}_p$, we find [2]

$$\Omega_R T_{\mathrm{lp,DW}} = \left[\sum_{p=1}^{N} \left(v_j^{(p)}\eta_p\right)^4 \overline{n}_p(\overline{n}_p + 1)\right]^{-1/2} \tag{7.30}$$

$$\eta_p^2 \equiv \frac{\sqrt{2}k}{(2Nm_{\mathrm{Be}}\xi_p\omega_z)^{1/2}} \tag{7.31}$$

where we define η_p the Lamb-Dicke parameter of the pth mode of N ions and the quantities $v_j^{(p)}$, ξ_p are defined by Eq. (2.26). For a given set of motional-state parameters, we see that

$\Omega_R T_{\mathrm{lp,DW}}$ is constant, so the total gate error is proportional to the rotation angle θ.

7.2.4 Technical Noise

Intensity fluctuations of the Raman light during a logic gate also lead to uncontrolled fluctuations of the Rabi frequency with time. If the bandwidth of the intensity noise is much less than the inverse of the Raman pulse time, as is the case in our experiments, we can use the slow-noise model of the gate error. Since $\Omega_R \propto \sqrt{I_1 I_2}$, where I_j is the intensity of the jth Raman beam, we find

$$\Omega_R T_{\mathrm{lp}} = \frac{2}{(\sigma_1 + \sigma_2)} \tag{7.32}$$

where σ_j is the relative intensity noise (RIN) of the jth beam. Again we see that the total gate error is proportional to θ. Contributions to σ_j over times longer than the averaging time are neglected here, so the "decoherence" here depends on the length of the quantum computation being attempted. In other words, if you want to run a computation ten seconds long, the Raman beam intensity only needs to be stable for ten seconds. Eq. (7.32) is only an approximation to the gate error if the noise bandwidth is smaller than the average time between gates, as the gate errors can be correlated in this case.

Though the intensity noise cannot be reduced below the shot-noise limit, the resulting lower limit on gate error can be very small [2]. Typically we achieved about 10 Rabi flops for a gate error $< 50\%$ over an averaging time of ~ 30 s using intensity-stabilized Raman beams (Secs. 4.3.1 and 4.3.2). Assuming $\sigma_1 \approx \sigma_2$, Eq. (7.32) gives $\sigma_1 \approx 10^{-2}$ over the frequency range between 1/30 Hz and $\Omega_R \sim 100$ kHz. Each Raman beam has a power ~ 1 mW, so the shot-noise

RIN over this frequency band is $\sim 10^{-5}$. It is technically feasible to approach the shot-noise RIN, so this source of gate error can be greatly reduced.

Fluctuations in the relative optical phase of the Raman beams can induce fluctuations in the ion phases. The difference frequency between the Raman beams is generated by high-stability RF synthesizers, so phase noise from this source is negligible. The motion of the ion relative to the trap effectively causes fluctuations in the phase, as described in the last section. Phase errors can also arise from motion of the trap relative to the laser beams, which produces the same effect as phase noise of the RF synthesizer. However, we do not need to know the relative phases between gates performed in different shots of the experiment, so fluctuations slower than ~ 1 ms do not affect our results. We damped out vibrations of the trap relative to the resonator using springs inside the vacuum chamber. Mechanical vibrations of the resonator should be slower than 1 kHz. In any event, we see little evidence of phase fluctuations unless we require coherence between logic gates performed with different beam geometries (see Sec. 6.2.5). However, mechanical vibrations may have an effect on long quantum computations.

7.3 Errors in the Entangling Gate

All the errors described in the previous section for single-qubit rotations also affect the entangling gate, although to different extents. The T_2 from spontaneous emission remains the same. Since the entangling gate is slower than a $\pi/2$ rotation by a factor of $2/\eta_{\mathrm{logic}}$, the total gate error due to spontaneous emission increases by a factor of $2/\eta_{\mathrm{logic}}$. On the other hand, the error due to laser intensity noise is just proportional to the rotation angle $\theta \equiv \Omega_M t = \pi/2$ of the entangling gate, so the error in the entangling gate from this source is the same as the error in a $\pi/2$ carrier rotation.

An evaluation of the effects of ion motion on the entangling gate can be found in [66]. Since the entangling gate acts directly on the logic mode, the motion in this mode affects the gate differently from the motion in the spectator modes. In thermal equilibrium, we can characterize the motion by the average excitation $\overline{n}_{\mathrm{COM}}$ of the center-of-mass mode. The Debye-Waller effect of the spectator modes gives an upper limit to the error contribution

$$\epsilon_{\mathrm{DW,ent}} \leq \frac{\pi^2 N(N+1)}{8}\eta_{\mathrm{COM}}^4 \overline{n}_{\mathrm{COM}}(1.2\overline{n}_{\mathrm{COM}} + 1.4) \tag{7.33}$$

Heating of the logic mode during gate operation can cause errors in the nonperturbative regime by destroying the spin/motion entanglement essential to the gate. Assuming a constant heating rate on the logic mode, a master-equation treatment [66] predicts a contribution to the gate error

$$\epsilon_{\mathrm{heat,ent}} = \frac{\pi N}{4\eta_{\mathrm{logic}}\Omega_R}\frac{d\overline{n}_{\mathrm{COM}}}{dt} \tag{7.34}$$

which is just proportional to the number of quanta gained during a sideband π-pulse time. Our experiments used a logic mode with essentially zero heating rate (see Sec. 7.4), so this source of error was negligible.

An additional source of technical noise comes into play for the entangling gate. The Stark shift of $\omega_{\downarrow\uparrow}$ (Eq. 3.36) depends on the Raman beam power, so intensity noise of the beams causes a fluctuating Stark shift. These fluctuations are no greater than a few tens of kHz RMS, so they are small compared to the carrier Rabi frequency Ω_R and have no observable effect on single-qubit rotations. However, the linewidth of the entangling transition is only ~ 10 kHz, so these fluctuations have a large effect on the entangling gate.

The Stark shift varies with the wavelength of the Raman beams in much the same way as the spontaneous emission rate (Sec. 7.2.2). The ratio κ_{Stark} of Stark shift to carrier Rabi frequency conveniently quantifies the sensitivity of a single-qubit rotation to the Stark shift. The Stark shift was given in Eq. (3.39). Taking the usual Raman beam polarizations $\hat{\epsilon}_{\mathrm{B1}} = \pi$, $\hat{\epsilon}_{\mathrm{R2}} = \sigma^+ + \sigma^-$ on the $|\downarrow\rangle \leftrightarrow |\uparrow\rangle$ transition, we find from Eq. (3.39) that the Stark shift is exactly zero. However, Eq. (3.39) fails to account for the small corrections to the detunings Δ_k arising from the hyperfine splitting ω_{HF}. To lowest order in ω_H/Δ_k, we find the Stark shift

$$\delta_{\mathrm{Stark}} = \omega_{\mathrm{HF}} \frac{\Omega_{\mathrm{B1}}^2 + \Omega_{\mathrm{R2}}^2}{3} \left[\frac{1}{\Delta^2} + \frac{2}{(\omega_{\mathrm{FS}} - \Delta)^2} \right] \tag{7.35}$$

and writing $|\Omega_{\mathrm{B1}}| = r|\Omega_{\mathrm{R2}}|$ gives

$$\kappa_{\mathrm{Stark}} = \frac{1 + r^2}{r} \Delta \left(1 - \frac{\Delta}{\omega_{\mathrm{FS}}} \right) \left[\frac{1}{\Delta^2} + \frac{2}{(\omega_{\mathrm{FS}} - \Delta)^2} \right] \tag{7.36}$$

The sensitivity to Stark shift is minimized for $r = 1$ with the Raman wavelength of 313.341 nm used in the experiment. In practice, we needed to carefully adjust the polarization of R2 using a $\lambda/4$ plate to obtain the minimum κ_{Stark}. The response of the entangling gate to a detuning is difficult to calculate, so we did not quantify the noise contribution from this mechanism. However, we did not observe broadening of the entangling transition beyond the 10 kHz Rabi linewidth for κ_{Stark} near its minimum, suggesting that the remaining noise did not induce much gate error.

We also implemented the entangling gate on the field-independent $|F = 2, m_F = 0\rangle \leftrightarrow |F = 1, m_F = 0\rangle$ transition. Here we used the B2, R1 beams as described in Section 4.3.2. The fidelity was about the same as that obtained on the $|\downarrow\rangle \leftrightarrow |\uparrow\rangle$ transition. The $|\downarrow\rangle \leftrightarrow |\uparrow\rangle$ transition is about a factor of 20 more sensitive to magnetic field fluctuations than the field-independent transition, as described in Section 7.1. The Stark shift of the field-independent transition is also

independent of polarization. Hence the experiments on the field-independent transition ruled out polarization and magnetic field fluctuations as sources of error in the entangling gate.

We were never able to reduce the error in the two-ion gate below ~ 0.08. The fundamental error limit due to spontaneous emission is 0.02. The initial temperature of the COM mode was at least $\overline{n} = 0.50$, because of the limit to Raman cooling imposed by the ion heating (Secs. 3.3.4 and 7.4). Eq. (7.33) then predicts an error of ~ 0.06 from the Debye-Waller effect. The error from these two effects accounts for most of the observed error, so we believe that other technical noise did not contribute much error. The four-ion gate error of 0.43 probably arises almost completely from the Debye-Waller effect. From Eq. (7.33) we see that the Debye-Waller error scales as N^2 for fixed $\overline{n}_{\mathrm{COM}}$. It was difficult to measure the temperature of the four-ion crystal, but $\overline{n}_{\mathrm{COM}}$ was certainly higher for four ions than for two. Reducing the heating rate and thus the initial temperature should enable entanglement of more than four ions.

7.4 Heating of the Ion Motion

In all ion traps described in this thesis, we observed a heating of the COM motional mode. This heating caused the COM motional state to relax toward a thermal distribution with average occupation number $\overline{n}_{\mathrm{COM}}$ over motional Fock states. Since $\overline{n}_{\mathrm{COM}}$ increased linearly under the heating, we quantify the heating rate as $\Gamma_{\mathrm{heat}} = \dot{\overline{n}}_{\mathrm{COM}}$. To measure $\overline{n}_{\mathrm{COM}}$ at a given time, we typically took sideband spectra for a single ion. Defining P_{rsb} (P_{bsb}) the maximum population in $|\uparrow\rangle$ when driving the red (blue) sideband, we have [2, 122]

$$\overline{n}_{\mathrm{COM}} = \frac{P_{\mathrm{rsb}}}{P_{\mathrm{bsb}} - P_{\mathrm{rsb}}} \tag{7.37}$$

which is valid for any drive duration, even if the ion is not in the Lamb-Dicke limit. To obtain high signal-to-noise, we typically set the drive duration to maximize P_{bsb}. We extracted Γ_{heat} by Raman cooling the ion near the ground state and measuring $\overline{n}_{\mathrm{COM}}$ after a variable delay.

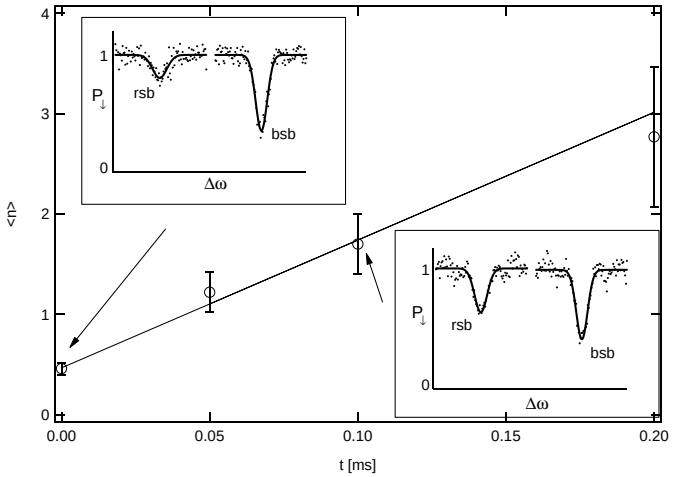

Figure 7.1: A typical heating measurement. The main graph shows $\overline{n}_{\mathrm{COM}}$ vs. the delay time t. Insets show the population $P_{\downarrow}$ remaining in $|{\downarrow}\rangle$ after the Raman drive. The data are for linear trap #2 with secular frequency 5 MHz. The data show $\Gamma_{\mathrm{heat}} = 12 \pm 2$ quanta/ms.

Figure 7.1 shows a typical example of a heating measurement.

Since ions are electrically charged, the obvious candidate for a source of heating is a fluctuating electric field. If this field originates at the trap electrodes, we expect the field to be spatially uniform over the ion crystal, so that the field couples only to the COM mode of the crystal. Heating measurements with a two-ion crystal [28] confirm that the COM heating rate is a factor of several hundred larger than the heating rate of the axial stretch mode. We measure the fluctuating field in terms of a spectral density $S_E(\omega)$ (in SI units) normalized so that the RMS field strength is $(2\pi)^{-1} \int_0^\infty S_E(\omega)\, d\omega$. For a single ion of mass m, the heating rate can be found from S_E as [123]

$$\Gamma_{\mathrm{heat}} = \frac{10^4 e^2}{4m\hbar\omega_{\mathrm{COM}}} S_E(\omega_{\mathrm{COM}}) \tag{7.38}$$

The ion only responds to driving fields near ω_{COM}. Assuming the electric field originates at the electrodes and that the fluctuating potential is spatially uniform over an electrode, a typ-

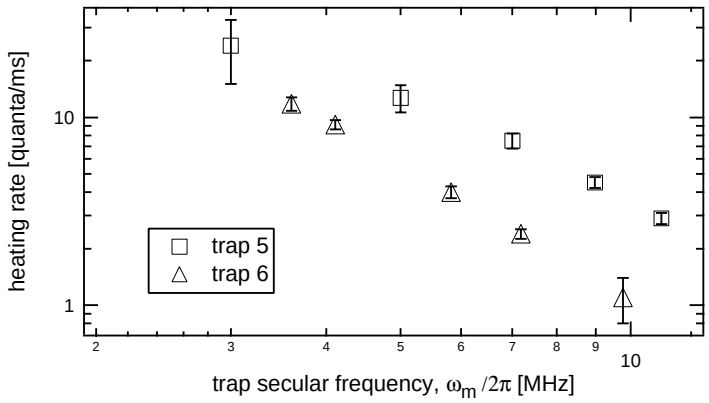

Figure 7.2: Heating measurements for trap #2 (squares) and trap #3 (triangles) at several values of ω_{COM}. Γ_{heat} approximately scales as $\omega_{\mathrm{COM}}^{-2}$.

ical heating rate $\Gamma_{\mathrm{heat}} \sim 1\mathrm{ms}^{-1}$ corresponds to a fluctuating potential noise power density $\sim 1(\mathrm{nV})^2/\mathrm{Hz}$ near ω_{COM}. Even a very small fluctuation is enough to give rise to the observed heating.

7.4.1 Heating Measurements and Interpretations

We measured Γ_{heat} for a wide variety of traps, as described in [122]. The heating rate was typically $1 - 30\mathrm{ms}^{-1}$ for all traps. These included Paul traps constructed from both Be and molybdenum, and the three linear traps, which had gold electrodes, so the heating appears to be largely independent of trap design. Figure 7.2 shows heating data for linear traps #2 and #3 at several values of ω_{COM}. From Eq. (7.38) and the approximate $\omega_{\mathrm{COM}}^{-2}$ scaling of the data, we find $S_E \sim 1/\omega_{\mathrm{COM}}$. The difference in scale between the two data sets is probably due to the increase in wafer spacing from trap #2 to trap #3 (see Sec. 2.2.1).

Figure 7.2 suggests that the heating rate depends on the size of the trap. However, we

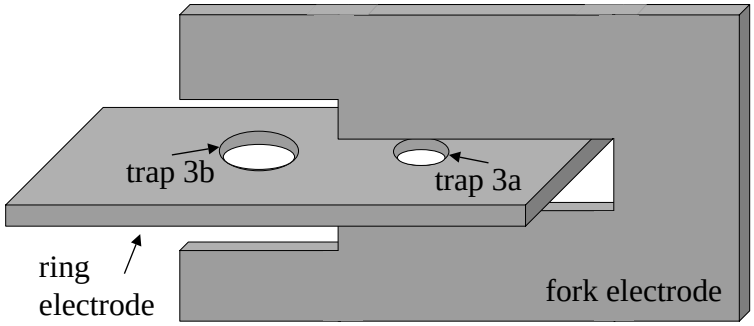

Figure 7.3: Schematic of the double Paul trap. The distance between the two rings is 1.7 mm.

could not confidently compare data from different traps because of the many factors that could not be controlled from trap to trap. To give only one example, it is extremely difficult to investigate the surface chemistry at the electrodes *in situ*. To investigate the size dependence in a controlled way, we constructed a "double" ring-and-fork Paul trap with two rings, as shown in Figure 7.3. By this means we hoped to compare the two traps formed by the two rings under similar conditions. We refer to the larger (smaller) trap as trap PL (PS). The distance d from the ion to the nearest electrode surface was 395 μm for PL, 175 μm for PS. Figure 7.4 shows Γ_{heat} as a function of ω_{COM} for two datasets taken with these traps. Between the two datasets, the trap was removed from the vacuum apparatus, cleaned as described in [122], and replaced. The first dataset yields a scaling $\Gamma_{\mathrm{heat}} \propto d^{(3.8\pm0.6)}$, while the second yields the remarkably strong scaling $\Gamma_{\mathrm{heat}} \propto d^{(12\pm2)}$.

The heating rate also tended to increase as a trap aged. The first trap used for quantum logic experiments in our group was a molybdenum Paul trap (trap P1) with $d = 170\mu$m. Figure 7.5 shows heating rate measurements for trap P1 over a period of almost two years. The trap was under vacuum continuously over this time, and the only known change inside the vacuum apparatus was the plating of Be onto the electrodes from loading. Here the solid line is meant

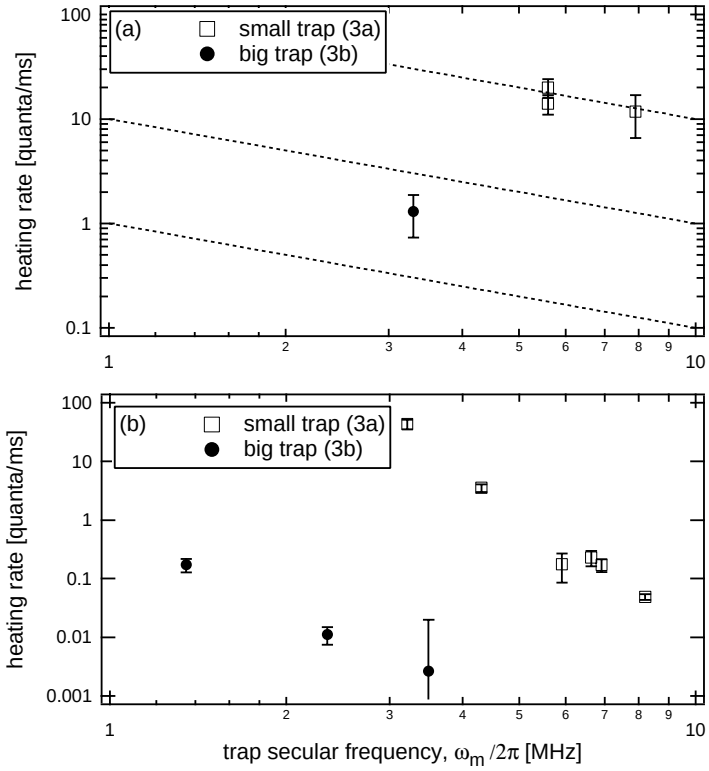

Figure 7.4: Heating measurements for trap PL (circles) and trap PS (squares). (a) First dataset, showing a scaling $\Gamma_{\rm heat} \propto d^{(3.8\pm0.6)}$. (b) Second dataset, showing a scaling $\Gamma_{\rm heat} \propto d^{(12\pm2)}$.

solely as a guide to the eye, but it certainly appears as though the heating rate increased by about a factor of four over this time.

The heating data obtained so far do not clearly indicate the source of heating. However, we have ruled out a great many possible sources of heating, including injection of noise from the RF and DC sources used to operate the trap, background gas collisions, and RF heating [2]. One theoretical explanation, which is absolutely not borne out by experiment, is thermal (Johnson) noise [124, 125]. Modeling the thermal noise as a potential on the electrodes originating from a lumped resistor gives the expression [122]

$$\Gamma_{\text{heat}} = \frac{e^2 k_B T R}{m\hbar\omega_{\text{COM}} d^2} \tag{7.39}$$

where we take $T = 300$ K. Apart from the fact that a realistic value of R gives $\Gamma_{\text{heat}} \sim 1\text{s}^{-1}$ rather than 1ms^{-1}, this model predicts a scaling $\Gamma_{\text{heat}} \propto d^{-2}$. The data presented in Figures 7.2 and 7.4 are both inconsistent with this scaling.

Among people who have made experimental studies of heating, a popular model of heating assumes a random distribution of fluctuating charges at the electrode surface. The potentials due to the fluctuations at different points add incoherently, leading to a scaling $\Gamma_{\text{heat}} \propto d^{-4}$, which is consistent with the data in Figures 7.2 and 7.4(a). Unfortunately, we have made little progress in identifying the source of these fluctuations. One possible mechanism involves the adsorption of gas onto patches of the electrode. The gas charges up, and movement of the patches gives rise to charge fluctuations. However, it is hard to imagine the motion giving rise to significant noise power at $\omega_{\text{COM}} \sim 5$ MHz. Another intriguing possibility is the formation of charge traps by impurities and crystal defects at the electrode surface [126]. Electrons tunnel in and out of these traps over a large range of timescales, giving rise to a $1/f$ noise spectrum. Noise from this source has been detected in other systems for frequencies up to 100 GHz [127]. The $1/f$ spectral dependence is also consistent with the observed scaling $S_E \propto 1/\omega_{\text{COM}}$.

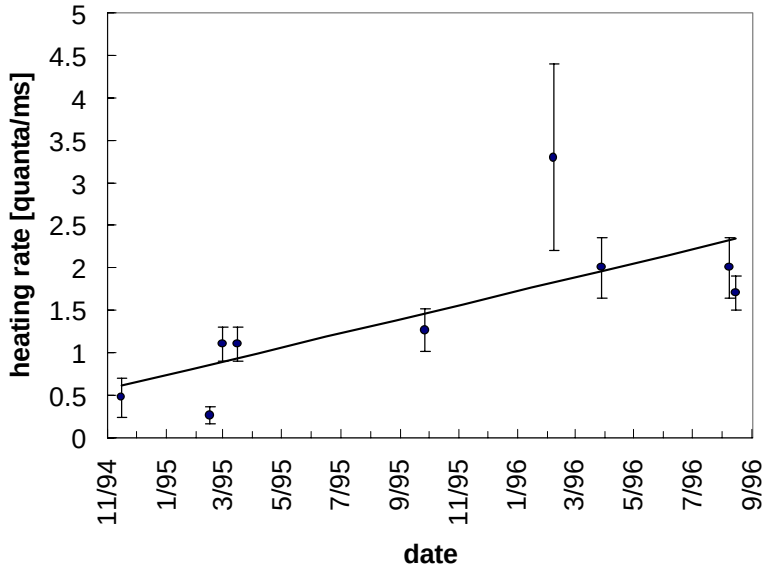

Figure 7.5: Heating measurements for trap P1 over a period of two years. The solid line is a guide to the eye, but indicates a distinct increase in heating rate with trap age. The trap remained under vacuum for the entire period shown.

7.4.2 Sympathetic Cooling for Quantum Logic

Heating is currently the largest source of error in our entangling gate through the Debye-Waller effect. Moreover, the temperature of the ion crystal increases as a computation proceeds, so that the error contribution increases over the value of 0.06 quoted above. Section 8.2 furnishes a striking example of this effect. Apparently we must actively cool the ions to perform a long computation. However, the cooling mechanism will cause decoherence if it couples to the register.

We have proposed a scheme for sympathetic cooling [128] of the quantum register by laser-cooling only the center ion in a string with an odd number of ions [17]. Here the COM motion of the whole crystal is cooled through coupling to the center ion. If the ions are sufficiently spatially separated, one can simply focus the cooling beams so that they affect only the center ion. By using a different species for the cooling ion, the cooling transition can be separated from any transition of the logic ions by many THz, relaxing the focusing requirement. In either case, the cooling affects only the internal states of the center ion, leaving all other internal coherences intact. If the logic operations use a mode in which the center ion remains at rest, the motional coherences in that mode are also unaffected by the cooling. In this case the logic mode will not directly couple to the uniform electric fields causing the heating and the decoherence will arise from the Debye-Waller effect (see Secs. 7.2.3 and 7.3).

If we use different species for logic and cooling ions, the dynamics of the crystal are no longer governed by the theory of Section 2.1.3, but change according to the mass ratio

$\mu = m_{\text{cool}}/m_{\text{logic}}$ of the two species. The potential energy (Eq. 2.21) remains the same, since $m\omega_z^2$ depends only on the electric field strength. The equilibrium positions u_i (Eq. 2.22) are then independent of μ. To solve for the normal modes, we define a normalized time $T = \omega_z t$ and normalized motional amplitudes $Q_i(t)$ as $Q_i = q_i$, $i \neq n_c$, $Q_{n_c} = q_{n_c}\sqrt{\mu}$. Here n_c is the index of the center ion. The motion is then governed by the Lagrangian [17]

$$L = \frac{1}{2}\sum_{i=1}^{N}\left(\frac{dQ_i}{dT}\right)^2 - \frac{1}{2}\sum_{i,j=1}^{N} A'_{ij}Q_iQ_j \tag{7.40}$$

$$A'_{ij} = \begin{cases} A_{ij} & i,j \neq n_c \\ A_{ij}/\sqrt{\mu} & i \text{ or } j = n_c,\ i \neq j \\ A_{ij}/\mu & i = j = n_c \end{cases} \tag{7.41}$$

$$A_{ij} = \begin{cases} 1 + 2\sum_{k=1,\neq i}^{N} \frac{1}{|u_i - u_k|^3} & i = j \\ -2\frac{1}{|u_i - u_k|^3} & i \neq j \end{cases} \tag{7.42}$$

where i and j index the ions and n_c is the index of the center ion.

Figure 7.6 shows the axial mode frequencies calculated from the Lagrangian Eq. (7.40) for 3, 5, 7, and 9 ions. The modes are numbered in order of increasing frequency (at $\mu = 1$), and are normalized to the trap frequency ω_z for a single logic ion. In each case, the lowest-lying mode has all ions moving in the same direction and is just the COM mode for $\mu = 1$. For $\mu \neq 1$, however, all the odd-numbered ("hot") modes participate in the center-of-mass motion of the crystal. Hence all these modes couple to the spatially uniform heating field. The even-numbered ("cold") modes correspond to the $(N-1)/2$ modes for which the center ion does not move. Their frequencies are independent of μ, and they do not participate in the COM motion, so they do not heat.

Cold modes are suitable for quantum logic, since they do not heat and they are not directly affected by the sympathetic cooling. Figure 7.6 shows that each cold mode is nearly degenerate with a hot mode for $\mu \gg 1$. To perform our entangling gate, we need to resolve the logic mode from other normal modes, so small frequency splittings limit the speed of our logic gates. The regime $\mu \lesssim 1$ is more convenient for quantum logic, since mode #2 is well-resolved from all other modes in this case.

We can predict the mode heating rates Γ_k for the kth hot mode of the two-species crystal by modifying Eq. (7.38). Normalizing to the COM heating rate for a one-species crystal with the same number of ions and the same trap frequency, we find [17]

$$\gamma_k \equiv \frac{\Gamma_k}{\Gamma_{\text{heat}}} = \frac{1}{N\xi_k}\left(\frac{v_{n_c}^{(k)}}{\sqrt{\mu}} + \sum_{j=1,\neq n_c}^{N} v_j^{(k)}\right) \tag{7.43}$$

assuming that the spectral density $S_E(\omega)$ is constant over the frequency range of the normal modes, i.e., $S_E(\omega_z) = S_E(\zeta_k \omega_z)$. Figure 7.7 shows the calculated heating rates for the hot modes of 3, 5, 7, and 9 ions. Since the heating rate is inversely proportional to the mode frequency, the variation of heating rate in Figure 7.7 is partly due to the variation of mode frequency with μ.

We now consider the effect of species substitution on the transverse dynamics. The transverse potential (Eq. 2.11) depends on the mass, so the trap potential is different for the center ion than for the others. If we include the effects of the static field, the transverse potential becomes

$$\omega_x = \omega_{\text{RF}}\sqrt{1 - \frac{{\omega_z}^2}{\omega_{\text{RF}}}} \tag{7.44}$$

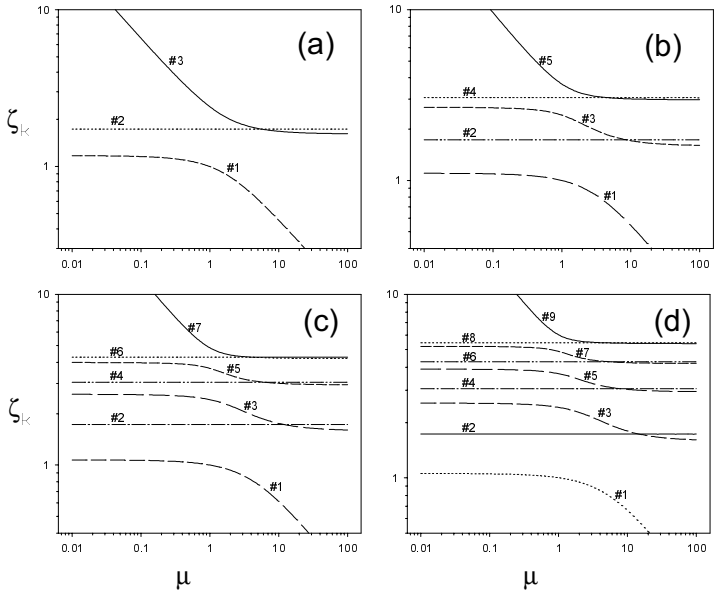

Figure 7.6: Normalized axial mode frequencies as a function of μ for (a) 3, (b) 5, (c) 7, and (d) 9 ions.

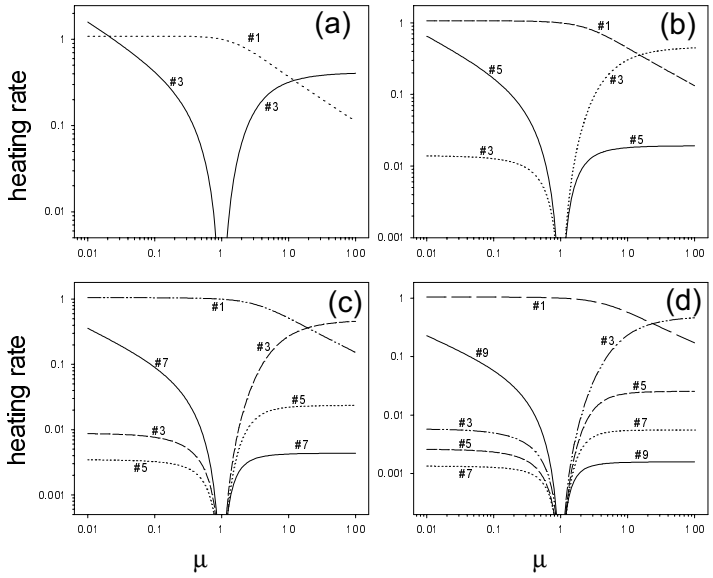

Figure 7.7: Normalized heating rates for the axial modes as a function of μ for (a) 3, (b) 5, (c) 7, and (d) 9 ions.

under the condition $\omega_x = \omega_y$. Using the same normalizations of time and amplitude as for Eq. (7.40), we have the Lagrangian

$$L = \frac{1}{2}\sum_{i=1}^{N}\left(\frac{dx_i}{dT}\right)^2 - \frac{1}{2}\sum_{i,j=1}^{N} B'_{ij}x_i x_j \tag{7.45}$$

$$B'_{ij} = \begin{cases} B_{ij} & i,j \neq n_c \\ B_{ij}/\sqrt{\mu} & i \text{ or } j = n_c,\ i \neq j \\ B_{ij}/\mu & i = j = n_c \end{cases} \tag{7.46}$$

$$B_{ij} = \begin{cases} \varepsilon^2 - \frac{1}{2} - \sum_{k=1,\neq i}^{N} \frac{1}{|u_i - u_k|^3} & i = j,\ j \neq n_c \\ \frac{\varepsilon^2}{\mu} - \frac{1}{2} - \sum_{k=1,\neq i}^{N} \frac{1}{|u_i - u_k|^3} & i = j = n_c \\ \frac{1}{|u_i - u_j|^3} & i \neq j \end{cases} \tag{7.47}$$

where ε was defined after Eq. (2.28).

For sufficiently small ε, the ion string breaks into a zigzag pattern as described in Section 2.1.3. We can find the critical value $\varepsilon_s(\mu)$ for this transition by solving $\det B'(\varepsilon, \mu) = 0$. Figure 7.8 shows the critical anisotropy as a function of μ for 3, 5, 7, and 9 ions. As discussed in [17], either of two different modes becomes unstable, depending on the value of μ. The arrows in Fig. 7.8 show the position of the crossover between the two modes.

Figure 7.9 shows the frequencies of the transverse modes, normalized to ω_z, for 3, 5, 7, and 9 ions. We choose $\varepsilon = 1.1\varepsilon_s(\mu)$; at higher values of ε the mode spacings decrease rapidly. Again we find cold (even-numbered) and hot (odd-numbered) modes. The large frequency splitting required to use a cold transverse mode for quantum logic only occurs near the zigzag instability and for $\mu \sim 1$, as shown by Figure 7.9. The effect of perturbations under these conditions is

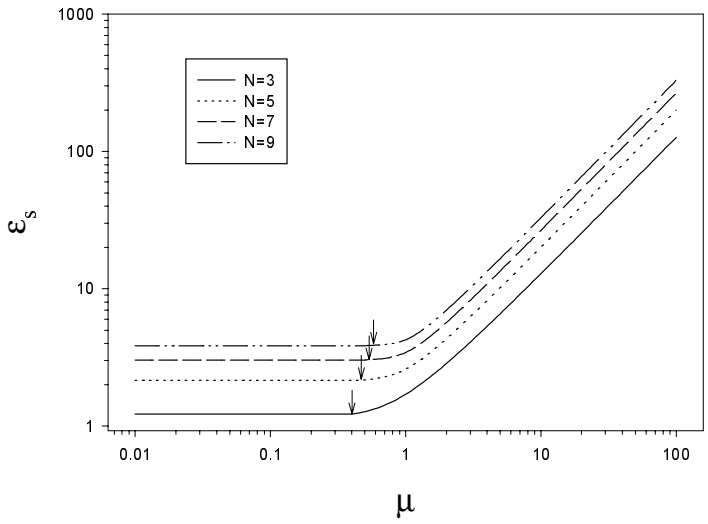

Figure 7.8: Trap anisotropy at the zigzag instability as a function of μ for 3, 5, 7, and 9 ions. Arrows indicate the crossover point between two distinct zigzag instabilities.

probably large, so the axial modes are better candidates for logic than the transverse modes in this scheme.

We calculated the heating rates for the transverse modes in the same way as for the axial modes. Again, all hot modes couple to the COM motion. Figure 7.10 shows the results for 3, 5, 7, and 9 ions.

The analysis above indicates that, all other things being equal, it is best to use a cooling ion that is not much heavier than the logic ions, and that the lowest-lying cold axial mode is most suitable for quantum logic. For technical reasons, however, we plan to implement sympathetic cooling of $^{9}Be^{+}$ with $^{24}Mg^{+}$. For three ions, an axial frequency of 10 MHz then yields a spacing of 1.6 MHz between the cold axial breathing mode and its nearest neighbor. This splitting is large compared with our sideband Rabi frequencies ($\sim$ 50 kHz), so sympathetic cooling is compatible with quantum logic even in this nonideal case.

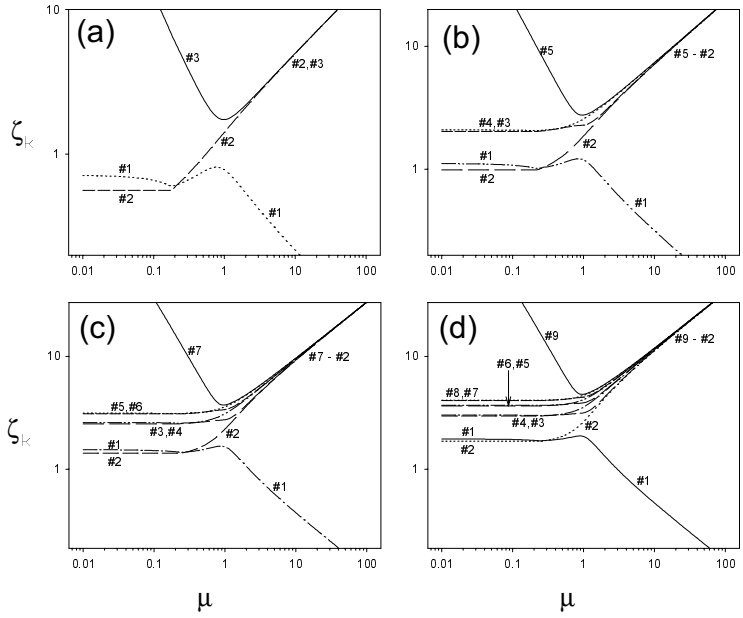

Figure 7.9: Normalized frequencies of the transverse modes as a function of μ with $\epsilon = 1.1\epsilon_0(\mu)$ for (a) 3, (b) 5, (c) 7, and (d) 9 ions.

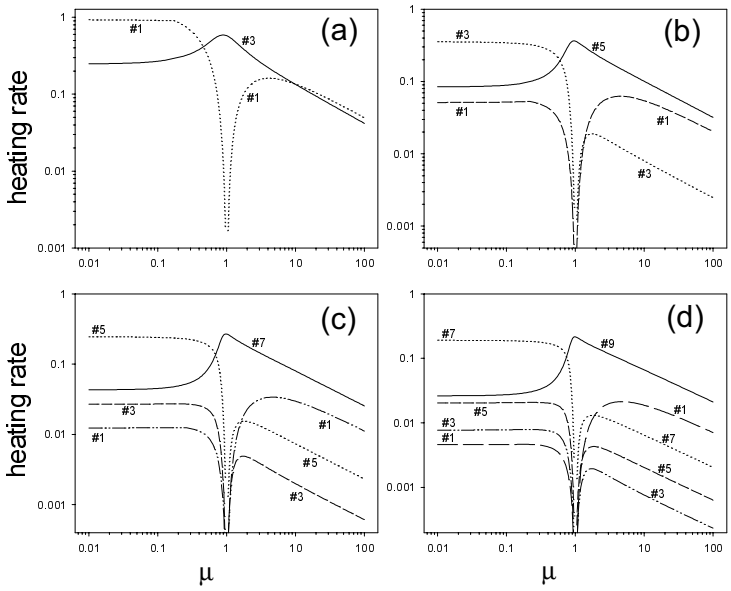

Figure 7.10: Normalized heating rates of the transverse modes as a function of μ with $\epsilon = 1.1\epsilon_0(\mu)$ for (a) 3, (b) 5, (c) 7, and (d) 9 ions.

Chapter 8

A Decoherence-Free Quantum Memory

8.1 Decoherence-Free Subspaces

Large-scale quantum computers will require robust long-term storage of quantum information [129]. As we saw in Chapter 6, a multitude of decoherence mechanisms stand in the way of a reliable quantum memory. In a classical computer, one usually evades memory errors by storing backup copies of information. However, the destructive nature of quantum measurement makes it impossible to reliably copy quantum information [130], so we must resort to other methods. One approach to improving quantum memory is to try to reduce the sources of noise on physical grounds, using magnetic shielding or "field-independent" transitions to avoid magnetic dephasing (Sec. 7.1) or reducing the technical noise of a laser to improve gate fidelity (Sec. 7.2.4). However, one can also use techniques based on the properties of quantum information to improve a quantum memory. These fall into two broad categories: decoherence-free subspace (DFS) encoding [131, 132, 133, 134, 135] and quantum error correcting codes (QECC) [136, 137, 138, 15, 139].

QECC's are the quantum analog of the error-correcting codes developed in classical information theory. They usually encode one qubit's worth of information (a "logical qubit") into two basis states of a small quantum register (the "physical qubits"). The decoherence mecha-

nism is assumed to cause an error on one of the physical qubits, altering the logical qubit as well. A properly selected partial measurement of the state of the physical qubits specifies the type of error that has occurred, without revealing any information on the state of the logical qubit. Applying suitable quantum logic then reverses the effect of the error. One can construct a wide variety of QECCs [140, 141, 142, 139] and many of these permit fault-tolerant QC, allowing perfect error correction even if the correction process is itself imperfect [143, 144, 139]. QECC-based fault tolerance comes at a high cost: for a large-scale quantum computation, we need $\gtrsim 10$ physical qubits per logical qubit [145].

Collective decoherence processes, which have the same effect on each qubit, are expected to cause decay of many proposed quantum memories [146, 147, 148, 149, 131, 132, 133]. In fact, the most prominent decoherence mechanism in our experiment is the collective dephasing caused by fluctuating magnetic fields, discussed in Section 7.1. Since the fields are spatially uniform across the ion string, the Hamiltonian for this process is

$$\mathbf{H}_{\mathrm{B}} \propto B_z(t) \sum_{i=1}^{N} \mathbf{S}_{i,z} = g\mathbf{J}_z \tag{8.1}$$

where B_z is the magnetic field component along the quantization axis (not along the trap axis $\hat{z}$!) Since we do not know $B_z(t)$, we cannot predict the evolution of an arbitrary superposition of register states.

One can exploit the equal coupling of Eq. (8.1) to find subspaces of the full register Hilbert space that are unaffected by collective decoherence. Since the noise Hamiltonian $\mathbf{H}_B$ depends only on $\mathbf{J}_z$, a superposition of two eigenstates of $\mathbf{J}_z$ with the same eigenvalue does not evolve under $\mathbf{H}_B$. Modeling the evolution under $\mathbf{H}_B$ by the transformation $|\uparrow\rangle \rightarrow e^{i\phi_B}|\uparrow\rangle$, we see that an arbitrary superposition of the two-ion states $|\downarrow\uparrow\rangle$, $|\uparrow\downarrow\rangle$ evolves as

$$a|\downarrow\uparrow\rangle + b|\uparrow\downarrow\rangle \rightarrow e^{i\phi_B}(a|\downarrow\uparrow\rangle + b|\uparrow\downarrow\rangle) = a|\downarrow\uparrow\rangle + b|\uparrow\downarrow\rangle \qquad |a|^2 + |b|^2 = 1 \tag{8.2}$$

Since the overall phase has no physical relevance, the superposition does not evolve under $\mathbf{H}_B$. On the other hand, if the coupling were not the same for the two qubits, an unknown relative phase would develop between $|\downarrow\uparrow\rangle$ and $|\uparrow\downarrow\rangle$ and a superposition of $|\downarrow\uparrow\rangle$ and $|\uparrow\downarrow\rangle$ would decohere.

The space spanned by $|\downarrow\uparrow\rangle$ and $|\uparrow\downarrow\rangle$ is the simplest example of a decoherence-free subspace [131, 132, 133]. Since this space contains two states, and the amplitudes a, b of the states are invariant under $\mathbf{H}_B$, we can encode one qubit's worth of information into this DFS. Below we experimentally demonstrate encoding of a qubit into this DFS and show that the encoded qubit resists collective dephasing. Although we have discussed only the coupling to magnetic field so far, encoding into the DFS protects against all forms of collective dephasing, i.e. any noise Hamiltonian of form (8.1). In particular, our data show the resistance of the DFS to collective dephasing originating from either a fluctuating magnetic field or a fluctuating uniform Stark shift.

The DFS discussed above only protects information from collective dephasing. A general collective process has the Hamiltonian

$$\mathbf{H}_{\text{coll}} = g(t)\sum_{i=1}^{N}\hat{n}(t)\cdot\vec{\mathbf{S}}_i = g(t)\hat{n}(t)\cdot\vec{\mathbf{J}} \tag{8.3}$$

where both $g(t)$ and $\hat{n}(t)$ fluctuate. In this case the evolution under $\mathbf{H}_{\text{coll}}$ depends only on the value of $\vec{\mathbf{J}}$. In particular, a state $|\Psi_S\rangle$ with $\vec{\mathbf{J}}|\Psi_S\rangle = 0$ is invariant under $\mathbf{H}_{\text{coll}}$. Such states are called singlet states, and the space of singlet states is the most general DFS for quantum registers made of qubits. For two qubits, there is only one such state, namely $|\downarrow\uparrow\rangle - |\uparrow\downarrow\rangle$. How-

ever, the number of singlet states grows rapidly with the number of qubits and approaches the number of register basis states in the limit of large N [131]. We therefore anticipate little or no overhead associated with the singlet DFS encoding for large registers. Of course, the singlet DFS encoding protects against collective dephasing as a special case.

Generic DFSs have been shown to support fault-tolerant QC [134, 135]. Moreover, a generic DFS is robust to small perturbations that break the collective symmetry; transitions between the DFS and the rest of the Hilbert space are suppressed to first order [134]. As a robust, low-overhead, QECC-compatible way to remove the ubiquitous collective decoherence, DFSs will most likely be intrinsic to future quantum computing architectures. Logic gates on DFS-encoded qubits have been proposed in the context of cavity quantum electrodynamics [150] and solid-state quantum logic schemes [135]. Also, a recent experiment has observed resistance of the singlet state of two photons to collective noise [151], but a DFS of at least two states is required to encode a qubit. Here we encode a qubit into a DFS for the first time.

8.2 Experimental Implementation of Encoding

Our encoding method reversibly maps an arbitrary state of one ion onto the DFS spanned by the states $|\Psi_{\pm}\rangle = |{\downarrow\uparrow}\rangle \pm |{\uparrow\downarrow}\rangle$, which is the same as the DFS over $|{\downarrow\uparrow}\rangle$, $|{\uparrow\downarrow}\rangle$ discussed above. The sequence of operations used to demonstrate encoding is given in Table 8.1. Here a "block" denotes a group of operations that jointly perform a quantum logic task. The first Ramsey block prepared the bare state $|\Psi_{\rm bare}(\alpha)\rangle = |{\downarrow}\rangle \otimes (|{\downarrow}\rangle - ie^{i\alpha}|{\uparrow}\rangle$ by rotating one ion while leaving the other ion alone. We refer to the ion rotated by the first Ramsey block as ion 2. In the bare state, the quantum information was carried by ion 2 alone. The encoding block mapped $|\Psi_{\rm bare}(\alpha)\rangle$ to the DFS-encoded state $|\Psi_{\rm DFS}(\alpha)\rangle = |\Psi_{-}\rangle + e^{i\alpha}|\Psi_{+}\rangle$, in which the information

was carried jointly in the DFS states of the two ions. We allowed the encoded state to evolve freely for a short time (usually $\sim 20\mu$s), then decoded it by performing the inverse of the unitary evolution applied by the encoding block. Decoding nominally returned the register to the bare state $|\Psi_{\rm bare}(\alpha)\rangle$. Finally, the second Ramsey block rotated ion 2 alone about an axis specified by β.

Ignoring the encoding and decoding blocks for a moment, we see that the two Ramsey blocks just implemented Ramsey spectroscopy on ion 2. Sweeping β and detecting $\langle \mathbf{S}_z \rangle$ gave rise to the usual Ramsey fringes (Eq. 6.6), but with a constant offset in $\langle \mathbf{S}_z \rangle$, since ion 1 always remained in the state $|\downarrow\rangle$. The amplitude of the Ramsey fringes nominally measured the coherence remaining in the state of ion 2 just before the second Ramsey block. Since the encoding and decoding blocks together amounted to just the identity operator, we could measure the coherence of the encoded state from the amplitude of the Ramsey fringes.

To perform a Ramsey block, we individually addressed the ions using the RF phase and trap voltage. In a classical picture of spin, the first rotation (e.g., step 1 in Table 8.1) took $\downarrow\downarrow$ to $\searrow\searrow$. The second rotation (e.g., step 2) reversed the sense of rotation on ion 1, while keeping it the same on ion 2, so the second rotation took $\searrow\searrow$ to $\downarrow\rightarrow$. This procedure rotated ion 2 alone, without changing the state of ion 1. The phase α was just set by the RF phase. More generally, two rotations by θ at these ion phases generated the state $\cos 2\theta|\downarrow\rangle - ie^{i\alpha}\sin 2\theta|\uparrow\rangle$.

In practice, we optimized the Ramsey block by using $\theta = \pi/2$, which nominally performed a π-pulse on ion 2, and maximizing the probability P_1 to have one ion bright. We used endcap voltages V_1, V_2 for the two rotations so as to change ϕ_1 by π. V_1 was the same endcap voltage

Table 8.1: The sequence of operations used to demonstrate DFS encoding. Rotations by an angle θ are written $\mathbf{U}_{\mathrm{car}}(\theta)$. "Block" refers to a group of operations that jointly perform a quantum logic task. A Ramsey block performs a $\pi/2$ rotation on ion 2 while leaving ion 1 alone. The encoding and decoding blocks map the information in ion 2 into and out of the DFS spanned by $|\Psi_-\rangle$, $|\Psi_+\rangle$. We specify some intermediate register states for clarity.

Number	Block	Operation	ϕ_1	ϕ_2	State After Operation
0	Initialize	–	–	–	$\|\downarrow\downarrow\rangle$
1	Ramsey	$\mathbf{U}_{\mathrm{car}}(\pi/4)$	α	α	–
2		$\mathbf{U}_{\mathrm{car}}(\pi/4)$	$\alpha+\pi$	α	$\|\downarrow\rangle \otimes (\|\downarrow\rangle - ie^{i\alpha}\|\uparrow\rangle)$
3	Encode	$\mathbf{U}_{\mathrm{ent}}^{-1}$	0	0	$(\|\downarrow\downarrow\rangle + i\|\uparrow\uparrow\rangle) - e^{i\alpha}\|\Psi_+\rangle$
4		$\mathbf{U}_{\mathrm{car}}(\pi/2)$	$\pi/2$	0	$\|\Psi_-\rangle + e^{i\alpha}\|\Psi_+\rangle$
5	Wait	–	–	–	–
6	Decode	$\mathbf{U}_{\mathrm{car}}(\pi/2)$	$3\pi/2$	π	$(\|\downarrow\downarrow\rangle + i\|\uparrow\uparrow\rangle) - e^{i\alpha}\|\Psi_+\rangle$
7		$\mathbf{U}_{\mathrm{ent}}$	0	0	$\|\downarrow\rangle \otimes (\|\downarrow\rangle - ie^{i\alpha}\|\uparrow\rangle)$
8	Ramsey	$\mathbf{U}_{\mathrm{car}}(\pi/4)$	$\alpha+\beta$	$\alpha+\beta$	–
9		$\mathbf{U}_{\mathrm{car}}(\pi/4)$	$\alpha+\beta+\pi$	$\alpha+\beta$	$\|\downarrow\rangle \otimes (\sin\frac{\beta}{2}\|\downarrow\rangle - ie^{i\beta}\cos\frac{\beta}{2}\|\uparrow\rangle)$
10	Detect	–	–	–	–

used for the entangling operations. We set V_2 from the calibration curve obtained for the Bell inequality experiment (Sec. 6.1). We then varied the differential voltage $V_{\rm shim}$ between the trap endcaps so as to produce a uniform field along $\hat{z}$ at the ion. For some value of this voltage, ion 2 moved by an integer number of wavelengths of the Raman beam pattern between the first and second rotations, so ϕ_2 remained the same for the two rotations, giving $P_1 \sim 0.98$. After tweaking V_2 and $V_{\rm shim}$ to maximize P_1, we reduced the carrier pulse lengths to half their former values, corresponding to $\theta \approx \pi/4$. We then tweaked the pulse lengths slightly to make $P_1 = P_2$, as expected for the state $|{\downarrow}\rangle \otimes (|{\downarrow}\rangle + e^{i\alpha}|{\uparrow}\rangle$. The resulting populations were approximately $P_0 = P_1 = 0.48$, $P_2 = 0.04$. Although the carrier pulses were less than 1 μs long, we had to allow $\sim 5\mu$s settling time after changing the trap voltage; otherwise the ion phases fluctuated during the second rotation, reducing the fidelity. The total time required to perform the Ramsey block was about 15 μs.

To encode the bare state into the DFS, we first applied the entangling gate three times (step 3 of Table 8.1) by tripling the usual entangling pulse duration, nominally obtaining the evolution $\mathbf{U}_{\rm ent}^{-1}$ (see Eq. (5.6). This operation mapped the part of the bare state in $|{\uparrow}\rangle$ into the DFS state $|\Psi_+\rangle$. The phases of the subsequent $\pi/2$ pulse (step 4) were set so that this pulse had no effect on $|\Psi_+\rangle$, but mapped the state $|{\downarrow\downarrow}\rangle + i|{\uparrow\uparrow}\rangle$ resulting from the entangling operation into the orthogonal DFS state $|\Psi_-\rangle$.

We set the phases for step 4 by changing the endcap voltage from V_1 to a third value V_3 and using the appropriate RF phase. We determined the value of V_3 roughly from the calibration curve. Using a π-pulse on ion 2 to generate $|{\downarrow\uparrow}\rangle$, then applying the encoding block nominally produced the DFS state $|\Psi_+\rangle$, with $P_1 = 1$. An incorrect value of V_3 reduced P_1, so we optimized V_3 by encoding $|{\downarrow\uparrow}\rangle$ and maximizing P_1. Here P_1 was independent of the RF

phase, so we were able to set V_3 and the RF phase separately. To set the RF phase, we applied the encoding block to the initial state $|\downarrow\downarrow\rangle$, nominally mapping it to $|\Psi_-\rangle$, and maximized P_1 with respect to the RF phase. Since the two bare basis states $|\downarrow\downarrow\rangle$, $|\downarrow\uparrow\rangle$ were mapped to the DFS basis states $|\Psi_-\rangle$, $|\Psi_+\rangle$, the superposition principle ensured that an arbitrary bare state would be mapped to a DFS state. Applying $U_{\rm ent}^{-1}$ took about 30 μs. Adding in the time to change the trap voltage and apply the rotation, we found that the encoding block required about 35 μs.

After waiting a minimum of $\sim 25\mu$s, we decoded the DFS state by applying the operator inverse of the encoding block. First we applied another $\pi/2$ pulse with the rotation axes of both ions reversed, corresponding to a change in the RF phase by π. The trap voltage was kept at V_3 throughout steps 4–6 to save settling time. We then changed the trap voltage to V_1 and applied the usual entangling gate. We had to apply the entangling gate three times to obtain its inverse, so the error of the inverse gate was three times that of the usual gate. The gate error from the DW effect increased due to heating, and this error would have tripled if we had used the usual gate in the encoding and the inverse gate in the decoding. The decoding block took 15 μs to complete. After decoding, the second Ramsey block and the detection produced the Ramsey fringes that constituted our signal.

We built up a histogram at each step of β from 1000 shots of the experiment. These data were analyzed as in the experiment of Chapter 5. We constructed reference histograms from the data averaged over β and used these references to deduce the value of P_i at each step of β. Ion 2 typically scattered about 10% more photons in $|\downarrow\rangle$ than ion 1 did, presumably due to unequal illumination by BD. We therefore allowed the mean of the Poissonian for one ion bright to vary independently of the mean for two ions bright. The extra free parameter did not increase the error in determining P_i. We fit the data on $P_i(\beta)$ to sinusoids of amplitude $\tilde{P}_i$. The error in $\tilde{P}_i$

was typically 0.05–0.08.

To determine the fidelity of the encoding/decoding sequence, we compared data taken with the encoding and decoding ("DFS data") to data taken without these operations ("bare data"). Dead time was substituted for the encoding/decoding operations in the latter case, so that the time between Ramsey blocks was the same in both cases. Ideally $\tilde{P}_0 = 0$, but in practice $P_0(\beta)$ oscillated appreciably in the data. For the bare data we found $\tilde{P}_0 \lesssim 0.04$, showing that the presumed individual rotation of ion 2 actually affected ion 1 as well. The two rotations composing a Ramsey block were therefore identical up to a gate error of ~ 0.02. For the DFS data we found $\tilde{P}_0 \lesssim 0.10$. P_1 and P_2 oscillated π out of phase with P_0 in both cases and we found $\tilde{P}_2 = \tilde{P}_0 + \tilde{P}_1$ within error. We characterized each dataset by the coherence $C = \tilde{P}_2$. For the bare data we found $C_{\rm bare} = 0.69 \pm 0.08$, while for the DFS data we found $C_{\rm DFS} = 0.43 \pm 0.05$. The loss of contrast of the bare data mostly comes from the decoherence of the bare state over the $\sim 100\mu$s delay between the two Ramsey blocks, as well as from the gate error, which we estimate as ~ 0.04 for each Ramsey block. We expect the population decay to be smaller than the decay of the coherence, so we can set a lower limit for the encoding/decoding fidelity as $F_{encode} \gtrsim C_{\rm DFS}/C_{\rm bare} = 0.62$. The errors in encoding and decoding mostly come from the DW effect on the entangling operations.

We set the synthesizer frequencies used for the Ramsey blocks to the exact resonance frequency of the carrier transition, which we measured using a normal Ramsey experiment on both ions. Here T_R ($\sim 100\mu$s) was much longer than the total time required to drive the Ramsey pulses ($\sim 1\mu$s), so the measured value of $\omega_{\downarrow\uparrow}$ did not suffer a significant Stark shift from the Raman beams. On the other hand, we measured the RR double-pass frequency $\omega_{\rm ent}$ used for the entangling transition (step 3) by taking a spectrum for a fixed pulse duration, so the

measured frequency experienced a relatively large Stark shift of ~ 7 kHz. We set the synthesizer frequency of the $\pi/2$ pulse (step 4) to $\omega_{\rm ent} - \omega_{\rm EOM}/2$ (in Hz) with accuracy better than ± 1 Hz, just as described in Section 5.2, to ensure mutual coherence of steps 3 and 4. We used the same frequencies for steps 3 and 7, and the same frequencies for steps 4 and 6.

The operations in the Ramsey blocks (steps 1, 2, 8, and 9) were thus all mutually coherent, as were the encoding and decoding sequences (steps 3, 4, 6, and 7). However, the encoding/decoding blocks were not coherent with the Ramsey blocks, since the synthesizer frequencies between the two blocks differed by the Stark shift (~ 7 kHz). In a frame rotating at the beat frequency of step 4, the bare state phase α precesses at ~ 7 kHz, so the data were effectively averaged over the bare state phase. The persistence of the coherence under these conditions shows that the encoding procedure works even if we do not know the bare state phase. It is then no stretch of credulity to suppose that the encoding procedure works for an arbitrary superposition of $|\downarrow\rangle$ and $|\uparrow\rangle$.

8.3 Decoherence of Bare and DFS States

To study the effects of decoherence on the bare and DFS states, we applied an engineered noisy environment for a time $t_{\rm noise}$ during step 5. We left some dead time after $t_{\rm noise}$ so that step 5 always lasted a fixed time of 25μs. To apply the noise, we turned on B2 with a randomly varying intensity for the time $t_{\rm noise}$. As described in Section 4.3.2, we directed B2 into the trap with a pickoff mirror so that we could vary the B2 and R2 polarizations independently. While the R2 polarization was set to minimize the Stark shift from R2, the B2 polarization was set to maximize the B2 Stark shift. We measured the Stark shift of B2 by turning on B2 for a short time between the two pulses of a Ramsey experiment and observing the resulting fringe

shift. Nominally, B2 equally illuminated the ions, so they experienced the same Stark shift. The fluctuating intensity of B2 therefore introduces a pure collective dephasing of the ion string.

We applied the random intensity modulation to B2 by modulating the amplitude of the RF power driving the B2 switch AOM. The modulation signal originated from the white-noise output of a Stanford Instruments DS345 signal generator. The noise was low-pass filtered with cutoff frequency 100 kHz and attenuation of 6 dB/octave using a Stanford Instruments SR560 preamplifier. We used the resulting signal to induce amplitude modulation of the RF signal driving the B2 switch before the RF signal was sent to its amplifier. We characterized the resulting intensity noise of B2 using a photodiode of bandwidth > 500 kHz. Figure 8.1 shows the power spectrum of a typical photodiode signal. We see that the spectrum is fairly flat below 100 kHz and drops off rapidly for higher frequencies. Since the photodiode bandwidth was much larger than the noise bandwidth, we can completely characterize the noise from the photodiode signal.

While the bare state should rapidly decohere under the noisy environment, the DFS state should resist the decoherence. Figure 8.2 shows the coherence remaining in the bare and DFS states as a function of the noise duration t_{noise}. The coherence data are normalized to their values for zero applied noise. We extracted the decay rates for the bare and DFS states from the exponential fit lines in Fig. 8.2, obtaining a rate of $0.18(1)\ \mu\mathrm{s}^{-1}$ for the bare state and $3.5(5.0) \times 10^{-3}\ \mu\mathrm{s}^{-1}$ for the DFS state. This result confirms our expectations; clearly collective dephasing occured, since the test state decayed, but the DFS state resisted the dephasing.

For white-noise intensity fluctuations of the Stark-shifting beam, we expect C to decay

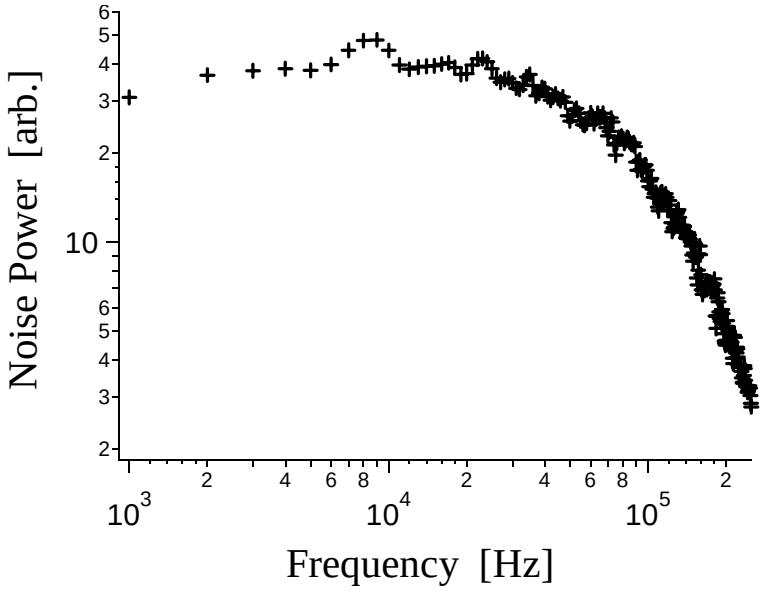

Figure 8.1: Power spectral density of the B2 intensity as determined from the photodiode signal. The spectrum is flat to ~ 100 kHz and drops off rapidly for higher frequencies, as desired. The measurement time of 5 ms limits the spectral resolution.

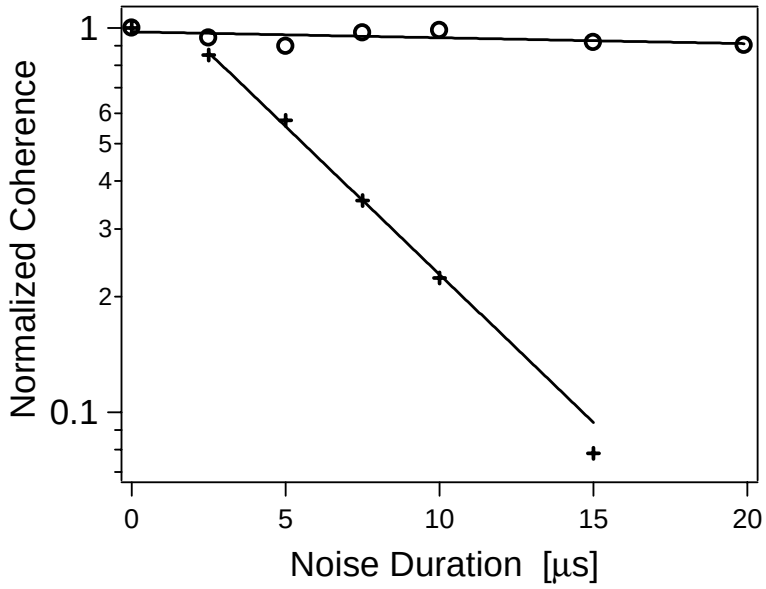

Figure 8.2: Decay of the DFS state (circles) and the bare state (crosses) under engineered collective dephasing. The noise is applied for a fraction of the delay time of about 25 μs between encoding and decoding. Coherence data are normalized to their values for zero applied noise. The fit lines are exponential decay curves, giving decay rates of $0.18(1)\ \mu\mathrm{s}^{-1}$ for the bare state and $3.5(5.0)\times 10^{-3}\,\mu\mathrm{s}^{-1}$ for the DFS state. The bare data point for zero applied noise is excluded from the fit (see text).

exponentially for the bare state, as shown by the fit line. Since the intensity fluctuations of the noise beam had $\sim$ 100 kHz bandwidth, Eq. (7.5) predicts a crossover between Gaussian and exponential decay of the bare state for $t_{\rm noise}$ of a few μs. This causes the anomalously low decay rate between $t_{\rm noise} = 0$ and 2.5μs in Figure 8.2. We were able to fit all the bare data in Figure 8.2 by numerically evaluating Eq. (7.4) using the observed noise spectrum from Figure 8.1. However, we also obtained a good fit to a simple exponential by simply excluding the bare data point with $t_{\rm noise} = 0$. The decay rate from this simpler fit is that quoted above.

To investigate the eventual decay of the DFS state, we increased the delay time to about 200 μs and applied decoherence for up to 100 μs during the delay time. The results are shown in Figure 8.3. The line is the best fit of the data to a Gaussian decay curve. The DFS state coherence dropped by 50% for 100 μs applied noise relative to its value for the same delay time and no applied noise. We believe that this decay was due to small departures from equal illumination by B2. In this case B2 applies a small, random differential phase to the two ions, modeled by the transformation $|\uparrow\rangle \rightarrow e^{i\phi_{\rm diff}}|\uparrow\rangle$ on ion 2 alone. Taking $\phi_{\rm diff}$ constant for a moment and averaging over α, we find $C = e^{-\phi_{\rm diff}^2/2}$, so the contrast drops even if the differential phase shift is not noisy. The phase $\phi_{\rm diff}$ should increase linearly with $t_{\rm noise}$, so this model reproduces the approximate Gaussian decay observed in Figure 8.3.

We also measured the decay of the bare and DFS states under ambient conditions in our laboratory. Here we left a variable delay time (step 5) between encoding and decoding to give the ambient noise a variable time to act. Figure 8.4 shows the coherence as a function of the delay time. The coherence data for this case are normalized in the same way as the data with applied noise. We empirically found a roughly exponential decay, shown by the fit lines, for both bare and DFS states. The fit lines give a decay rate of $7.9(1.5) \times 10^{-3}$ $\mu{\rm s}^{-1}$ for the test state

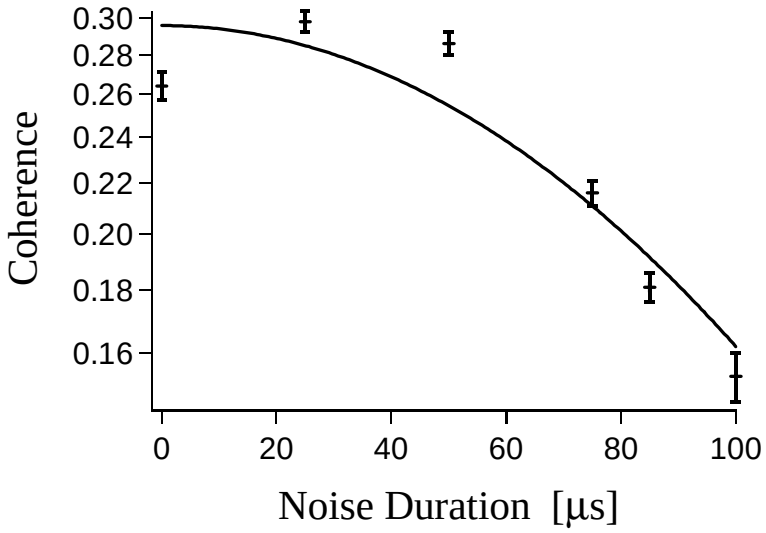

Figure 8.3: Decay of the DFS state (crosses) under application of B2 for up to 100 μs. The noise is applied for a fraction of the delay time of 200 μs between encoding and decoding. Coherence data are not normalized. The line is the best fit to a Gaussian decay curve.

and $2.2(0.3) \times 10^{-3}\ \mu\text{s}^{-1}$ for the DFS state. The decoherence of the bare state was dominated by ambient fluctuating magnetic fields with most of their power spectrum at 60 Hz and its harmonics. We treated this situation in detail in Section 7.1. Since the fields were roughly uniform across the ion string, they induced collective dephasing. The DFS state is resistant to this type of decoherence, as demonstrated by Figure 8.2. Since the DFS state maintained coherence much longer than the test state, we conclude that collective dephasing from magnetic field noise was the major ambient source of decoherence for the bare state. Though Figure 8.4 presents only normalized contrasts, the unnormalized contrast of the DFS state is higher than that of the test state for delay times exceeding 150 μs. Hence, encoding into the DFS materially improves the information storage under real conditions.

The apparent decay of the DFS coherence arises from the heating of the ions. As the delay time increases, so does $\overline{n}_{\text{COM}}$, and thus the DW gate error in the decoding block increases as well. Unfortunately, we do not have good theoretical predictions for the DW gate error when the DW error becomes large. We found a heating rate of $\sim 20\text{ms}^{-1}$ from data taken at roughly the same time as the data for this experiment. The error predicted by Eq. (7.33) for this heating rate is considerably **larger** than that observed in Figure 8.4. In any event, Figure 8.2 conclusively demonstrates that the loss of coherence is not due to any effect of collective dephasing.

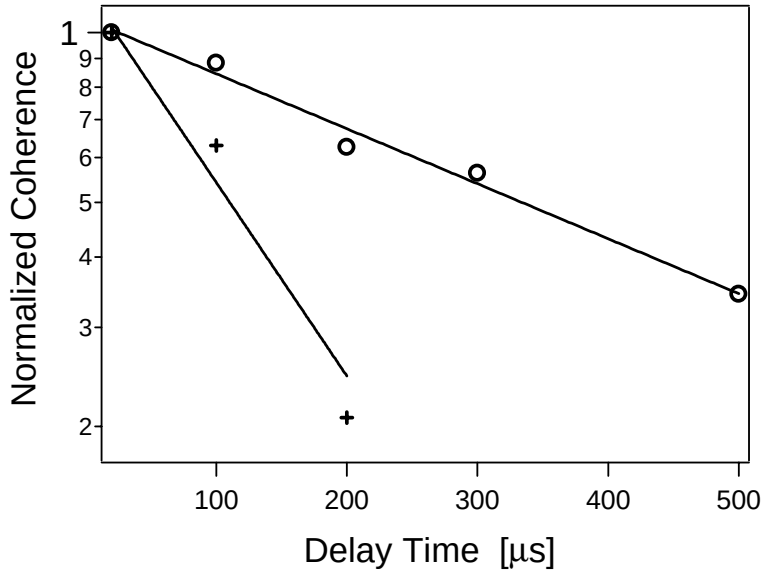

Figure 8.4: Decay of DFS-encoded state (circles) and test state (crosses) under ambient decoherence. We vary the delay time between encoding and decoding to give the ambient noise a variable time to act. Coherence data are normalized to their values for zero applied noise. The fit lines are exponential decay curves for purposes of comparison and are not theoretical predictions. The decay rate from the fit is $7.9(1.5) \times 10^{-3}\ \mu\text{s}^{-1}$, for the test state and $2.2(0.3) \times 10^{-3}\ \mu\text{s}^{-1}$ for the DFS state. Since the coherence time of the DFS-encoded state is much longer than that of the test state, we see that the chief source of ambient decoherence is collective dephasing.

Bibliography

[1] P.W. Shor. Proc. 35th Ann. Symp. Found. Comp. Sci., page 116. IEEE Computer Society, Los Alamitos, CA, 1994.

[2] D.J. Wineland et al. J. Res. NIST, 103:259, 1998.

[3] M.G. Raizen et al. J. Mod. Opt, 39:233, 1992.

[4] E.C. Beaty. J. Appl. Phys., 61:2118.

[5] M.A. Abramowitz and I.A. Stegun, editors. Handbook of Mathematical Functions, volume 55 of NBS Applied Mathematics Series. U.S. Gov't Printing Office, Washington, DC.

[6] P.K. Ghosh. Ion Traps. Clarendon, Oxford, 1995.

[7] J.J. Sakurai. Modern Quantum Mechanics. revised edition.

[8] J.I. Cirac et al. Phys. Rev. A, 49:421, 1994.

[9] D.F. Walls and G.J. Milburn. Quantum Optics. Springer, New York, 1994.

[10] M.G. Raizen et al. Phys. Rev. A, 45:6493, 1992.

[11] H. Walther. Adv. At. Mol. Phys., 31:137, 1993.

[12] D.G. Enzer et al. Phys. Rev. Lett., 85:2466, 2000.

[13] R. Rafac et al. Proc. Natl. Acad. Sci. USA, 88:483, 1991.

[14] J.P. Schiffer. Phys. Rev. Lett., 70:818, 1993.

[15] A. Steane. Appl. Phys. B, 64:623, 1997.

[16] D.F.V. James. Appl. Phys. B, 66:191, 1998.

[17] D. Kielpinski et al. Phys. Rev. A, 61:032310, 2000.

[18] J. Hoffnagle et al. Phys. Rev. Lett., 61:255, 1988.

[19] R. Blümel et al. Phys. Rev. A, 40:808, 1989.

[20] R.G. Brewer et al. Nature, 344:305, 1990.

[21] H.G. Dehmelt. In A De Marci, editor, Proceedings of the Fourth Symposium on Frequency Standards and Metrology, Berlin, 1996. Springer-Verlag.

[22] J.D. Prestage, G.J. Dick, and L. Maleki. J. Appl. Phys., 66:1013, 1989.

[23] H.G. Dehmelt. Adv. At. Mol. Phys., 3:53, 1967.

[24] R.C. Thompson. Adv. At. Mol. Phys., 31:63, 1993.

[25] S.R. Jefferts et al. Phys. Rev. A, 51:3112, 1995.

[26] A. Gerhard et al. IEEE Trans. Electrical Insulation, 24:1033, 1989.

[27] R.A. Kishek et al. Phys. Plasmas, 5:2120, 1998.

[28] B.E. King. Quantum State Engineering and Information Processing with Trapped Ions. PhD thesis, University of Colorado, 1999. Available at http://jilawww.colorado.edu/www/sro/thesis/king/index.html.

[29] J.J. Bollinger, J.S. Wells, D.J. Wineland, and W.M. Itano. Phys. Rev. A, 31:2711, 1985.

[30] O. Poulsen, T. Andersen, and N. Skouboe. J. Phys. B, 8:1393, 1975.

[31] E. Arimondo. Progress in Optics, volume 35, page 259. Elsevier, Amsterdam, 1996.

[32] D.J. Wineland and W.M. Itano. 20:1521, 1979.

[33] H.G. Dehmelt. Bull. Am. Phys. Soc, 20:60, 1975.

[34] D.J. Wineland, J.C. Bergquist, W.M. Itano, and R.E. Drullinger. Opt. Lett, 5:245, 1980.

[35] W. Nagourney, J. Sandberg, and H. Dehmelt. Phys. Rev. Lett., 56:2797, 1986.

[36] L. Allen and J.H. Eberly. Optical Resonance and Two-Level Atoms. Dover, New York, 1975.

[37] A.B. Klimov and L.L. Sanchez-Soto. Phys. Rev. A, 61:063802, 2000.

[38] J.I. Cirac and P. Zoller. Phys. Rev. Lett., 74:4091, 1995.

[39] D.J. Wineland and W.M. Itano. Phys. Rev. A, 20:1521, 1979.

[40] F. Diedrich, J.C. Bergquist, W.M. Itano, and D.J. Wineland. Phys. Rev. Lett., 62:403, 1989.

[41] C. Monroe et al. Phys. Rev. Lett., 75:4011, 1995.

[42] R.H. Dicke. Phys. Rev., 89:472, 1953.

[43] J.C. Bergquist, W.M. Itano, and D.J. Wineland. Phys. Rev. A, 36:428, 1987.

[44] B.E. King et al. Phys. Rev. Lett., 81:1525, 1998.

[45] Q.A. Turchette et al. Phys. Rev. A, 62:053807, 2000.

[46] Coherent Laser Group. Coherent 699 Ring Dye Laser Manual. Coherent, Santa Clara, CA.

[47] L. Hollberg. Dye Laser Principles with Applications, page 185. Academic Press, San Diego CA, 1990.

[48] T.W. Hänsch and B. Couillaud. Opt. Comm., 35:441, 1980.

[49] W. Demtröder. Laser Spectroscopy. Springer, New York, 1981.

[50] S. Gerstenkorn and P. Luc. Atlas du Spectre d'Absorption de la Molecule d'Iode. Laboratoire Aime-Cotton, CNRS II, Orsay, France, 1978.

[51] J.L. Hall and S.A. Lee. Appl. Phys. Lett., 29:367, 1976.

[52] P.J. Fox, R.E. Scholten, M.R. Walkiewicz, and R.E. Drullinger. Am. J. Phys., 67:624, 1999.

[53] J.J. Bollinger, D.J. Wineland, W.M. Itano, and J.S. Wells. Laser Spectroscopy VI, page 168. Springer, New York, 1983.

[54] M.J. Weber, editor. Handbook of Laser Science and Technology, volume III. CRC Press, Boca Raton, FL, 1986.

[55] R.W.P. Drever et al. Appl. Phys. B, 31:97, 1983.

[56] D. Deutsch, A. Barenco, and A. Ekert. Proc. Roy. Soc. London A, 449:669, 1995.

[57] S. Lloyd. Phys. Rev. Lett., 75:346, 1995.

[58] A. Barenco et al. Phys. Rev. A, 52:3457, 1995.

[59] C. Monroe et al. Phys. Rev. Lett., 75:4714, 1995.

[60] Q.A. Turchette et al. Phys. Rev. Lett., 75:4710, 1995.

[61] A. Rauschenbeutel et al. Phys. Rev. Lett., 83:5166, 1999.

[62] A. Sørensen and K. Mølmer. Phys. Rev. Lett., 82:1971, 1999.

[63] K. Mølmer and A. Sørensen. Phys. Rev. Lett., 82:1835, 1999.

[64] C.A. Sackett et al. Nature, 404:256, 2000.

[65] C. Cohen-Tannoudji, J. Dupont-Roc, and G. Grynberg. Atom-Photon Interactions. Wiley-Interscience, New York, 1992.

[66] A. Sørensen and K. Mølmer. Phys. Rev. A, 62:022311, 2000.

[67] J.J. Bollinger, D.J. Wineland, W.M. Itano, and D.J. Heinzen. Phys. Rev. A, 54:4649, 1996.

[68] W. Dür and J.I. Cirac. quant-ph/0011025.

[69] W.K. Wootters. Phys. Rev. Lett., 80:2245, 1998.

[70] C.H. Bennett et al. Phys. Rev. Lett., 76:722, 1996.

[71] M. Lewenstein et al. J. Mod. Opt, 47:2481, 2000.

[72] V. Vedral and M.B. Plenio. Phys. Rev. A, 57:1619, 1998.

[73] A. Einstein, B. Podolsky, and N. Rosen. Phys. Rev., 47:777, 1935.

[74] J.S. Bell. Physics (N.Y.), 1:195, 1965.

[75] S.J. Freedman and J.F. Clauser. Phys. Rev. Lett., 28:938, 1972.

[76] M. Lamehi-Rachti and W. Mittig. Phys. Rev. D, 14:2543, 1976.

[77] A. Aspect, P. Grangier, and G. Roger. Phys. Rev. Lett., 49:91, 1982.

[78] A. Aspect, J. Dalibard, and G. Roger. Phys. Rev. Lett., 49:1804.

[79] G. Weihs et al. Phys. Rev. Lett., 81:5039, 1998.

[80] H. Zbinden, J. Brendel, N. Gisin, and W. Tittel. Phys. Rev. A, 63:022111, 2001.

[81] D. Bohm. Phys. Rev., 85:166, 1952.

[82] D. Bohm. Phys. Rev., 85:180, 1952.

[83] J.F. Clauser, M.A. Horne, A. Shimony, and R.A. Holt. Phys. Rev. Lett., 23:880, 1969.

[84] J.F. Clauser and M.A. Horne. Phys. Rev. D, 10:526, 1974.

[85] P.H. Eberhard. Phys. Rev. A, 47:747, 1993.

[86] T. Richter. Optica Acta, 30:1769, 1983.

[87] U. Eichmann et al. Phys. Rev. Lett., 70:2359, 1993.

[88] J. Bergquist, editor. Proc. 5th Conf. on Frequency Standards and Metrology. World Scientific, Singapore, 1996.

[89] D.M. Sullivan et al. J. Res. NIST, 106:47, 2001.

[90] T. Udem et al. Phys. Rev. Lett., 86:4996, 2001.

[91] N.F. Ramsey. Molecular Beams. Oxford Univ. Press, London, 1963.

[92] R.P. Feynman, F.L. Vernon, and R.W. Hellwarth. J. Appl. Phys., 28:49, 1957.

[93] J. Schwinger. Quantum Theory of Angular Momentum, page 229. Academic Press, New York, 1965.

[94] B. Yurke, S.L. McCall, and J.R. Klauder. Phys. Rev. A, 33:4033, 1986.

[95] M. Born and E. Wolf. Principles of Optics. Cambridge University Press, Cambridge UK, 7th ed. edition.

[96] W.M. Itano et al. Phys. Rev. A, 47:3554, 1993.

[97] G. Santarelli et al. Phys. Rev. Lett., 82:4619, 1999.

[98] F.T. Arecchi, E. Courtens, R. Gilmore, and H. Thomas. Phys. Rev. A, 6:2211, 1972.

[99] C.M. Caves. Phys. Rev. D, 23:1693, 1981.

[100] M. Xiao, L.A. Wu, and H.J. Kimble. Phys. Rev. Lett., 59:278, 1987.

[101] P. Grangier, R.E. Slusher, B. Yurke, and A. LaPorta. Phys. Rev. Lett., 59:2153, 1987.

[102] M. Kitagawa and M. Ueda. Phys. Rev. A, 47:5138, 1993.

[103] D.J. Wineland et al. Phys. Rev. A, 46:6798, 1992.

[104] D.J. Wineland, J.J. Bollinger, W.M. Itano, and D.J. Heinzen. Phys. Rev. A, 50:67, 1994.

[105] A. Kuzmich and L. Mandel. Quantum Semiclass. Opt., 10:493, 1998.

[106] J. Hald, J. L. Sorensen, C. Schori, and E. S. Polzik. Phys. Rev. Lett., 83:1319, 1999.

[107] A. Kuzmich, L. Mandel, and N.P. Bigelow. Phys. Rev. Lett., 85:1594, 2000.

[108] C. Orzel et al. Science, 291:2386, 2001.

[109] V. Meyer et al. Phys. Rev. Lett., To appear, 2001.

[110] D.F. Walls and P. Zoller. Phys. Rev. Lett., 47:709, 1981.

[111] K. Wódkiewicz and J. Eberly. J. Opt. Soc. Am. B, 2:458, 1985.

[112] M.J. Holland and K. Burnett. Phys. Rev. Lett., 71:1355, 1993.

[113] P. Bouyer and M.A. Kasevich. Phys. Rev. A, 56:1083, 1997.

[114] T. Kim et al. Phys. Rev. A, 57:4004, 1998.

[115] B.C. Sanders and G.J. Milburn. Phys. Rev. Lett., 75:2944, 1995.

[116] T. Kim et al. Opt. Comm., 156:37, 1998.

[117] L. Mandel and E. Wolf. Optical Coherence and Quantum Optics. Cambridge Univ. Press, Cambridge, UK, 1995.

[118] R. Alicki. Phys. Lett. A, 103:247, 1984.

[119] A.O. Caldeira and A.J. Leggett. Phys. Rev. A, 31:1059, 1985.

[120] D.F. Walls and G.J. Milburn. Phys. Rev. A, 31:2403, 1985.

[121] H. Frauenfelder. The Mossbauer Effect. Benjamin, New York, 1963.

[122] Q.A. Turchette et al. Phys. Rev. A, 61:063418, 2000.

[123] D.J. Wineland et al. Forts. der Physik, 46:363, 1998.

[124] S.K. Lamoreaux. Phys. Rev. A, 56:4970, 1997.

[125] D.F.V. James. Phys. Rev. Lett., 81:317, 1998.

[126] J.M. Martinis. private communication.

[127] M. Covington, M.W. Keller, R.L. Kautz, and J.M. Martinis. Phys. Rev. Lett., 84:5192, 2000.

[128] D.J. Larson et al. Phys. Rev. Lett., 57:70, 1986.

[129] A. Steane. Proc. 5th Intl. Conf. on Quantum Communication, Measurement, and Computing. Capri, Italy, to appear.

[130] W.K. Wootters and W.H. Zurek. Nature, 299:802, 1982.

[131] D.A. Lidar, I.L. Chuang, and K.B. Whaley. Phys. Rev. Lett., 81:2594, 1998.

[132] P. Zanardi and M. Rasetti. Phys. Rev. Lett., 79:3306, 1997.

[133] L.M. Duan and G.C. Guo. Phys. Rev. A, 57:737, 1998.

[134] D.A. Lidar, D. Bacon, and K.B. Whaley. Phys. Rev. Lett., 82:4556, 1999.

[135] D. Bacon, J. Kempe, D.A. Lidar, and K.B. Whaley. Phys. Rev. Lett., 85:1758, 2000.

[136] P.W. Shor. Phys. Rev. A, 52:2493, 1995.

[137] A.M. Steane. Proc. Roy. Soc. London A, 452:2551, 1996.

[138] E. Knill and R. Laflamme. Phys. Rev. A, 55:900, 1997.

[139] M.A. Nielsen and I.A. Chuang. Quantum Information and Quantum Computation. Cambridge Univ. Press, Cambridge, UK, 2000.

[140] A.R. Calderbank and P.W. Shor. Phys. Rev. A, 54:1098, 1996.

[141] A.M. Steane. Phys. Rev. Lett., 77:793, 1996.

[142] R. Laflamme, C. Miquel, J.P. Paz, and W.H. Zurek. Phys. Rev. Lett., 77:198, 1996.

[143] P.W. Shor. Proc. 37th Symp. Found. Comp. Sci., page 56. IEEE Computer Science Press, Los Alamitos, CA, 1996.

[144] D.P. DiVincenzo and P.W. Shor. Phys. Rev. Lett., 77:3260, 1996.

[145] A.M. Steane. Nature, 399:124, 1999.

[146] G.M. Palma, K.-A. Suominen, and A.K. Ekert. Proc. Roy. Soc. London A, 452:567, 1996.

[147] P. Zanardi and F. Rossi. Phys. Rev. Lett., 81:4752, 1998.

[148] Fortsch. der Physik, 46(No. 4-8).

[149] Fortsch. der Physik, 48(No. 9-11).

[150] A. Beige, D. Braun, B. Tregenna, and P.L. Knight. Phys. Rev. Lett., 85:1762, 2000.

[151] P.G. Kwiat, A.J. Berglund, J.B. Altepeter, and A.G. White. Science, 290:498, 2000.